AREA QUALITÀ, PROGRAMMAZIONE E SUPPORTO STRATEGICO
SETTORE STRATEGIA PER LA RICERCA
U. O. DOTTORATI

Università degli Studi di Palermo

Dottorato di Ricerca in Scienze Fisiche e Chimiche
Dipartimento di Fisica e Chimica - Emilio Segrè
Settore Scientifico Disciplinare PHYS-04/A

EMISSION DYNAMICS OF A QUBIT IN PHOTONIC LATTICES WITH SYNTHETIC POTENTIALS

IL DOTTORE
MARCEL AUGUSTO PINTO
Marcel Augusto Pinto

IL COORDINATORE
MARCO CANNAS
Marco Cannas

IL TUTOR
FRANCESCO CICCARELLO
Francesco Ciccarello

CO TUTOR

CICLO XXXVIII
ANNO CONSEGUIMENTO TITOLO 2025

To Thamyres,
who stood at my side at the
best and worst moments.

“We must be clear that when it comes to atoms,
language can be used only as in poetry.”

— Niels Bohr

Acknowledgements

This thesis would not have been possible without the support, guidance, and encouragement of many people, to whom I am deeply grateful.

First and foremost, I would like to thank Prof. Francesco Ciccarello for his invaluable supervision throughout this project. His guidance, insight, and continuous support have been essential to my development as a researcher. I am also grateful for his support during my stay in Palermo, which made this experience both productive and enjoyable.

A special thanks goes to my wife, Thamyres, for her unwavering encouragement, patience, and support throughout this journey. Her presence has been a constant source of strength and motivation.

I would also like to thank my colleagues Giovanni Luca Sferrazza, Xuejian Sun and Enrico Di Benedetto for the many fruitful discussions that enriched this work and broadened my perspective.

I am particularly grateful to Prof. Francesco Ciccarello, Prof. Mauro Paternostro, Sujan Vijayaraj and Alessandro Romancino for their support during the organization of the group seminars, which provided a stimulating environment for scientific exchange and learning.

My sincere thanks also go to Prof. Salvatore Lorenzo for granting access to the computational resources that made the large-scale numerical simulations presented in this thesis possible.

I would like to express my gratitude to Prof. Alejandro González-Tudela for hosting me during my research stay abroad and for providing a welcoming and inspiring scientific environment.

I am also thankful to my office mates Alessandro Romancino, Marco Vetrano, Diana Chisholm, Simone Artini, and Daniele Morone for their companionship and for making everyday life in the office more enjoyable.

I would furthermore like to acknowledge Prof. Angelo Carollo, Prof. Umberto Di Giovannini, Luca Leonforte, Silvia Casulleras, Andris Erglis and Luca Innocenti for the many interesting conversations shared over lunch, which often extended well beyond physics.

Finally, I would like to thank Bar Vabres for the excellent coffee and food that fueled countless working days, and Bar Atenaeum for the traditional Friday pasta that became a cherished part of life in Palermo.

To everyone who contributed, directly or indirectly, to this work and to my experience during these years, thank you.

Abstract

Engineering the on-site frequencies of a photonic lattice provides a powerful route to endow emitted photons with non-trivial dynamical and topological properties, reshaping the way a coupled qubit decays. This thesis investigates the emission dynamics of a qubit weakly coupled to photonic lattices hosting such synthetic potentials, showing how the resulting band structure dictates qualitatively distinct regimes of light-matter interaction.

In the first part, we study a qubit coupled to a one-dimensional coupled-cavity array with a linear gradient in the cavity frequencies, which acts on photons as a synthetic force F. For strong F, emission becomes reversible and is captured by an effective Jaynes–Cummings model, producing a chiral, time-periodic excitation of an extended region of the array, either to the right or to the left of the qubit depending on its frequency. For weak F, the decay is non-Markovian and exhibits revivals reminiscent of atoms between mirrors, even though no mirrors are present: the finite bandwidth confines the emitted photon, and the dynamics is well described by a delay differential equation in which the amplitude and period of Bloch oscillations play the role of cavity length and round-trip time.

In the second part, we move to two dimensions and couple a giant atom, a qubit with multiple, spatially separated coupling points, non-locally to a honeycomb lattice of resonators with detuned sublattice frequencies. By suitably arranging the coupling points, the giant atom selectively addresses a single valley, a capability unattainable with a local emitter. This valley-selective coupling endows the emitted photons with an effective valley-polarized Berry curvature, giving rise to valley-polarized edge modes at domain walls between regions of opposite sublattice detuning. As a consequence, a giant atom placed near such a domain wall exhibits chiral emission of valley-polarized photons without breaking time-reversal symmetry, suggesting a natural implementation in circuit QED.

Together, these results establish synthetic potentials in photonic lattices as a versatile tool for controlling qubit emission, linking waveguide QED to Bloch-oscillation physics and to valleytronics.

Contents

Publications vii

1 Introduction 1

2 Background Theory and Methods 9
- 2.1 Atom-field Hamiltonian . . . 9
  - 2.1.1 Quantized electromagnetic field . . . 9
  - 2.1.2 Atom . . . 10
  - 2.1.3 General form of the atom-field Hamiltonian . . . 11
  - 2.1.4 Rotating-wave approximation . . . 12
- 2.2 Single-excitation dynamics . . . 13
  - 2.2.1 Conservation of the total number of excitations . . . 13
  - 2.2.2 Single-excitation subspace . . . 14
  - 2.2.3 Equations of motion in the single-excitation sector . . . 14
- 2.3 Spontaneous emission . . . 16
  - 2.3.1 Local density of states . . . 17
- 2.4 Vacuum Rabi oscillations . . . 18
- 2.5 Non-Markovian emission due to photonic time delays . . . 19
- 2.6 QED in coupled-cavity arrays . . . 23
  - 2.6.1 Spontaneous emission into an infinite array . . . 24
  - 2.6.2 Non-Markovian emission into a finite array . . . 25
- 2.7 Coupled-cavity array with a synthetic potential . . . 26
  - 2.7.1 One-dimensional coupled-cavity array with linear synthetic potential . . . 27
- 2.8 Giant atoms . . . 32
  - 2.8.1 Giant-atom-enabled chiral emission . . . 33
- 2.9 Topological photonic lattices . . . 34
  - 2.9.1 Topological edge modes . . . 37
  - 2.9.2 The honeycomb lattice . . . 39
  - 2.9.3 Spectrum and normal modes of H_B . . . 40
  - 2.9.4 Valleys K and K' . . . 41
  - 2.9.5 Topological properties of valleys . . . 42

3 Non-Markovian decay of an atom due to Bloch oscillations 43
- 3.1 Model and Hamiltonian . . . 44
- 3.2 Dynamics of qubit emission via numerical simulations . . . 45
  - 3.2.1 Chiral vacuum Rabi oscillations . . . 46
  - 3.2.2 Non-Markovian decay with revivals . . . 47
- 3.3 Theoretical analysis . . . 50

3.3.1 Regimes of light-matter interaction 51
3.3.2 Strong-force: vacuum Rabi oscillations 51
3.3.3 Weak-force: delay differential equation 52
3.3.4 Differences from an atom in a conventional cavity 54
3.4 Experimental implementations 55
3.5 Conclusions 56

4 Chiral emission of valley-polarized light from a giant atom **58**
4.1 Model and Hamiltonian 59
4.2 Selective coupling to a single valley 60
4.3 Spontaneous emission of valley-polarized photons 63
4.4 Valley-polarized edge modes 64
4.4.1 Edge modes 64
4.5 Single-photon chiral emission 66
4.5.1 Emission from a normal atom 66
4.5.2 Emission from a giant atom 68
4.6 Experimental Implementations 69
4.7 Conclusions 69

5 Conclusions **71**

Appendix A The Laplace Transform **75**

Appendix B Analytical Derivations of Return Times and Delay Differential Equations **76**
B.1 Return times 76
B.2 Derivation of the delay differential equation 77
B.3 Delay differential equation for generalized coupling-mode function . . . 78

Appendix C Derivation of Valley-Polarized Edge Modes **80**
C.1 Derivation of the edge modes 80

Bibliography **82**

Publications

The research carried out in this thesis has resulted in the following papers

- **M. A. Pinto**, G. L. Sferrazza, D. De Bernardis, and F. Ciccarello, *Non-Markovian dynamics of a qubit due to accelerated light in a lattice*, Phys. Scr. 100, 105304 (2025).
- **M. A. Pinto**, G. L. Sferrazza, S. Casulleras, A. González-Tudela, D. De Bernardis, and F. Ciccarello, *Giant-atom-enabled quantum optics with valley-polarized photons*, arXiv:2605.06771 (2026).

Besides these works, I have been involved in other collaborations during this period, which have led to the following works

- E. Di Benedetto, X. Sun, **M. A. Pinto**, L. Leonforte, C. Chang, V. Jouanny, L. Peyruchat, P. Scarlino, and F. Ciccarello, *Emergent cavity-QED dynamics along the edge of a photonic lattice*, arXiv:2507.13444 (2025).
- J. T. Schneider, **M. A. Pinto**, C. Tabares, A. Muñoz de las Heras, F. Ciccarello, and A. González-Tudela, *Scalable spin squeezing in a waveguide-QED platform*, in preparation (2026).

Chapter 1

Introduction

Waveguide quantum electrodynamics [1–3] studies the interaction between localized quantum emitters and confined photonic modes in engineered electromagnetic environments. In its most traditional form, this means emitters coupled to photons propagating in effectively one-dimensional waveguides. In a broader and by now widely useful sense, however, the same framework also includes emitters coupled to structured photonic reservoirs realized by coupled-cavity arrays, photonic crystals, and higher-dimensional photonic lattices, whenever the central problem is how confinement, dispersion, and geometry reshape light–matter interaction. In this setting, the reduction and control of the photonic phase space make the emitter–field coupling much more tunable than in free space. As a result, waveguide QED has become one of the natural meeting points between quantum optics, open quantum systems, and quantum many-body physics [1]. Its relevance is not only conceptual. The rapid development of nanophotonic and superconducting platforms has made it possible to engineer guided and lattice-confined reservoirs with high precision, so that the electromagnetic environment is no longer a fixed background, but rather a design variable.

A key idea in this field is that the properties of spontaneous emission, photon transport, and mediated interactions depend crucially on the spectral and spatial structure of the bath. In ordinary Markovian settings, the reservoir is often treated as broad and featureless around the emitter frequency, which leads to exponential decay and local-in-time dynamics. By contrast, in structured waveguides and photonic lattices the density of states can vary strongly with frequency, and the dispersion relation can exhibit finite bandwidths, band edges, gaps, slow-light regions, and nontrivial topology. In this regime, waveguide QED becomes a setting where light–matter interaction is shaped by geometry and band structure as much as by bare coupling strengths [4–6].

This viewpoint is especially fruitful in photonic lattices. Here the guided field is naturally described in terms of collective lattice modes, often within a tight-binding picture, and the emitter probes a reservoir with an engineered dispersion relation. Photonic lattices therefore provide a clean route to move beyond textbook spontaneous emission and into a regime where the bath retains memory, photons can localize around emitters, and effective interactions become tunable in range, sign, and anisotropy. For this reason, photonic lattices are not merely one possible implementation of waveguide QED, but one of the most transparent physical arenas in which its central ideas can be explored.

Structured reservoirs and the physics of band engineering

The simplest conceptual step beyond standard waveguide QED is to replace a broad continuum by a structured photonic environment. Already in the early work on photonic band-gap materials, it was realized that an emitter tuned near a band edge does not simply radiate away its excitation into a featureless continuum. Instead, the strong spectral dependence of the photonic density of states produces anomalous Lamb shifts, non-exponential relaxation, and the formation of dressed atom–photon states localized around the emitter [4–6]. These bound states are among the clearest signatures that the field can no longer be eliminated as a memoryless bath.

From a modern perspective, this physics can be read as a continuum generalization of cavity QED. In cavity QED, strong coupling leads to dressed light–matter states because the emitter hybridizes with a small number of discrete modes. In structured waveguide QED, a similar hybridization can occur inside or near a continuum whenever the dispersion and bandwidth constrain photon propagation strongly enough. The resulting atom–photon bound states interpolate between localized cavity-like modes and propagating-waveguide excitations [7]. This is one of the reasons why structured waveguides are so appealing: they allow one to explore strong-coupling phenomena without giving up transport, nonlocality, or many-body scalability.

Near a band edge, the group velocity is reduced and the photonic density of states is enhanced. In this slow-light regime, both coherent and dissipative effects are amplified, but not in a trivial way. The emitter may experience inhibited decay, strong dressing by the nearby continuum, and a crossover from predominantly radiative behavior to interaction through localized photonic clouds. This basic mechanism has been discussed theoretically in detail and has also been observed in superconducting and optical implementations [7–10]. What makes these results especially important for quantum optics is that they show that the vacuum itself can be engineered to become colored, dispersive, and spatially structured.

Photonic lattices as a natural setting for waveguide QED

Photonic lattices offer a particularly convenient language for this program. In arrays of coupled cavities or resonators, the photonic bath is described by bands emerging from photon hopping, while localized emitters couple to selected lattice sites or modes. This makes the connection between microscopic design and emergent optical behavior unusually direct. The lattice spacing, hopping amplitudes, onsite frequencies, and dimensionality can all be used to reshape the reservoir seen by the emitters. As a consequence, waveguide QED in photonic lattices provides access to finite-bandwidth transport, controllable localization, and interaction ranges that can differ radically from those of free-space dipolar systems [11–13].

This lattice viewpoint is valuable both physically and conceptually. Physically, it explains why quantities such as group velocity, band curvature, and gap width become decisive for emission and scattering. Conceptually, it links quantum optics to the broader toolkit of condensed-matter and many-body theory. In a photonic lattice, a single emitter can act as an impurity embedded in a band structure, while multiple emitters can generate collective states mediated by the lattice modes. Depending on frequency and geometry, the same platform may interpolate between dissipative transport, coherent exchange, and bound-state-mediated coupling. In this sense, photonic lattices turn waveguide QED into a flexible laboratory for reservoir engineering.

Another important aspect is that lattice baths make it easier to move beyond one-dimensional intuition. Structured reservoirs in two dimensions, topological waveguides, and anisotropic band structures can produce directional emission, unconventional superradiance and subradiance, and bound states with spatial structure set by the underlying lattice rather than by geometric optics alone [1, 14]. This broader perspective is useful for the present thesis, where waveguide QED is understood not only as transport in a strictly one-dimensional channel, but more generally as quantum optics of emitters embedded in structured photonic lattices, including two-dimensional ones, provided that the bath remains sufficiently controlled for its dispersion and mode geometry to govern the emission process. Even when one ultimately focuses on one-dimensional implementations, the broader lesson remains the same: the bath can be designed to carry its own nontrivial kinematics, and the emitter dynamics inherit that structure.

Beyond single-emitter physics, photonic lattices provide a natural platform for studying collective radiative phenomena and photon-mediated interactions. When multiple emitters couple to the same structured bath, interference effects can give rise to superradiant and subradiant states, while propagating bath modes induce both collective dissipation and coherent excitation exchange [1, 15]. Near photonic band edges or within band gaps, however, the electromagnetic dressing becomes spatially localized, leading to the formation of emitter-photon bound states that mediate interactions while strongly suppressing radiative losses [7–9, 13]. The overlap of these bound states between distant emitters can be exploited to engineer effective spin models with tunable interaction strength and range [16–18]. As a result, waveguide QED platforms have emerged as a versatile testbed for quantum simulation, enabling the realization of engineered many-body Hamiltonians and exotic quantum phases [19–22].

Long delays and effective Markovian regimes as an emerging direction

A very active line of current research concerns waveguide QED with significant propagation delays. In conventional quantum-optical models, retardation is often neglected because the travel time of photons between nodes is much shorter than the internal system dynamics. Modern platforms, however, make it possible to engineer situations in which the delay becomes an explicit ingredient of the problem. This has pushed waveguide QED toward a broader regime where propagation, memory, and network structure must be treated on equal footing [23, 24].

Even when the underlying field can still be described as a propagating quantum channel, long delays can qualitatively reshape the dynamics by feeding back previously emitted radiation after a finite time. This gives rise to a modern form of quantum optics in which the system is not merely coupled to a reservoir, but to its own time-delayed output or to distant emitters through a delayed channel. In suitable parameter regimes one can still formulate effective Markovian descriptions for the local nodes while keeping the delay as a physically essential timescale of the interconnection [23]. This perspective has become especially important for quantum networks, cascaded architectures, and engineered feedback protocols.

Experiments with superconducting structured reservoirs have shown that the border between Markovian and non-Markovian behavior is now experimentally accessible rather than merely conceptual. In particular, slow-light waveguides and mirror-like boundaries can generate revivals, non-exponential decay, and tunable crossovers between short-memory and delayed-feedback regimes [24]. For this reason, long-delay waveguide QED should be viewed as one of the emerging frontiers of modern quantum optics: it expands the traditional framework of open systems by making propagation time itself a design parameter.

Chiral quantum optics

Another major contemporary development is chiral quantum optics, where the coupling between emitters and guided modes depends on the propagation direction. In standard waveguides, emission to the left and to the right is usually symmetric. In nanophotonic and structured environments, however, spin–momentum locking and polarization engineering can break this symmetry and lead to directional light–matter interaction [25]. This is conceptually significant because it moves waveguide QED beyond reciprocal transport and toward genuinely directional quantum dynamics. Recent reviews have highlighted how this perspective now connects waveguide QED to a broader range of solid-state and many-body platforms [26].

Chiral coupling enables single emitters to radiate preferentially into one direction and allows arrays of emitters to realize cascaded interactions, nonreciprocal transport, and dissipative generation of entangled states [25, 27]. Experiments in nanophotonic waveguides and photonic-crystal structures have demonstrated strongly directional spontaneous emission and near-deterministic chiral interfaces [28, 29]. From the viewpoint of the present thesis topic, chiral quantum optics is important not as a separate subfield, but as a natural extension of the same central idea: once the photonic environment is engineered in detail, light–matter interaction need not be isotropic, local, or reciprocal. Directionality itself becomes a resource.

Giant atoms and nonlocal light–matter coupling

A further striking departure from standard quantum-optical intuition is provided by giant atoms. In the usual dipole approximation, the emitter is treated as pointlike on the scale of the wavelength and couples locally to the field. Superconducting circuits and related artificial-atom platforms make it possible to violate this assumption by coupling a single emitter to the same waveguide at several spatially separated points. The resulting interference between coupling points changes both decay and interaction mechanisms in a way with no direct analogue for ordinary small atoms [30, 31].

This nonlocal coupling has several consequences. First, relaxation rates become frequency dependent through interference, so that decay can be enhanced, suppressed, or even effectively cancelled at selected frequencies. Second, giant atoms can sustain decoherence-free exchange interactions mediated by the waveguide, a feature that is difficult or impossible to realize with purely local emitters [30]. Third, when combined with structured reservoirs, giant atoms provide an especially rich platform in which band structure and nonlocal coupling geometry interplay. Recent theoretical work has developed a general framework for giant atoms coupled to structured photonic baths, including genuinely two-dimensional lattices such as square lattices, photonic graphene, and extended Lieb lattices [32]. On the experimental side, a recent realization has implemented a transmon giant atom non-locally coupled to a high-impedance coupled-cavity array [see Fig. 1.1(c)], demonstrating that giant-atom physics can now be explored directly in a lattice-structured bath [33]. The phase-dependent coupling points can be engineered experimentally through effective complex couplings. In particular, periodic modulation of the emitter–waveguide coupling can be employed to induce a controllable coupling phase, thereby enabling the realization of complex-valued couplings [34].

For a thesis centered on photonic lattices, giant atoms are therefore relevant for two reasons. They broaden the notion of what an emitter in waveguide QED can be, and they highlight once more that modern quantum optics is increasingly based on engineered coupling geometries rather than on fixed microscopic assumptions. Their experimental realization with superconducting artificial atoms has made this direction especially visible [35, 36].

Experimental motivation and focus on circuit QED lattices

The broad theoretical interest in waveguide QED would be far less compelling without the parallel progress of experimental platforms. Optical nanophotonics has established high-efficiency interfaces between emitters and guided modes, including photonic-crystal waveguides where coupling to the desired mode can approach unity [37, 38]. These systems have demonstrated superradiant effects, strong atom–photon coupling near band edges, and the transition from dissipative to predominantly dispersive interactions [8, 15]. They provide a clear proof that structured photonic environments can reshape quantum optical dynamics in precisely the ways anticipated by theory.

At the same time, superconducting circuits have opened a particularly powerful route to implementing the same ideas in the microwave domain. In circuit QED, artificial atoms and resonators can be fabricated, tuned, and coupled with a level of control that is hard to match in other architectures. This makes coupled-resonator arrays especially attractive as photonic lattices: their band structure can be designed from the layout, their disorder can be kept low, and the qubit–photon coupling can be made strong enough to access bound-state and many-body regimes. More broadly, circuit-QED lattices have long been recognized as a natural platform for lattice quantum optics and for Jaynes–Cummings-type many-body models [39].

Recent experiments have made this connection concrete. Microwave photonic crystals and superconducting metamaterials have shown how band edges and band gaps can be used to engineer Lamb shifts, inhibit spontaneous emission, and generate localized photonic dressing around qubits [9, 10]. Going one step further, arrays of Josephson-junction resonators coupled to tunable qubits [Fig. 1.1(a)] have provided explicit realizations of photonic-lattice waveguide QED in which atom–photon bound states and their mutual interactions can be controlled directly [13]. For this reason, circuit-QED lattices based on coupled resonators and qubits form a particularly compelling endpoint for the present introduction: they combine the conceptual clarity of lattice models with the tunability of superconducting hardware, and they offer a direct route from the physics of structured reservoirs to experimentally accessible many-body quantum optics [13, 41].

In this sense, waveguide QED in photonic lattices is best viewed not simply as a specialization of cavity QED or as a variant of quantum transport. It is a broader framework in which the electromagnetic environment is designed to control emission, interactions, and correlations at the quantum level. The availability of modern photonic and superconducting platforms has turned this framework into a concrete experimental program, while current themes such as delayed quantum optical dynamics, chiral interfaces, and giant atoms continue to expand its scope. Within this landscape, circuit-

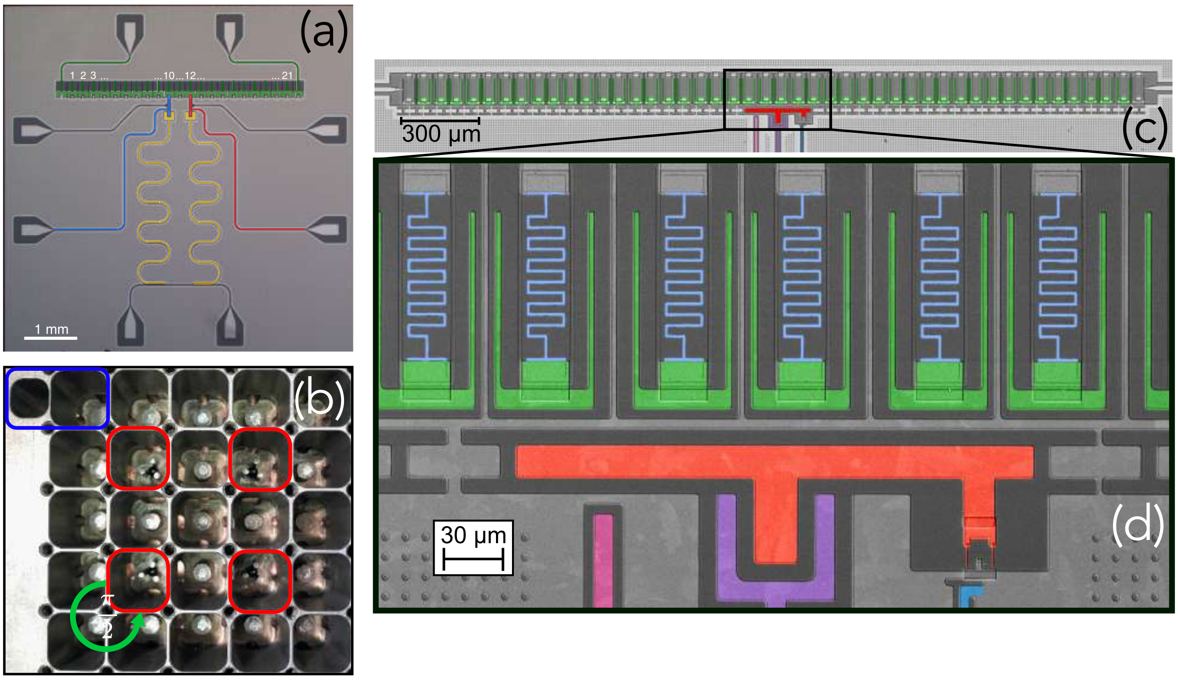

Figure 1.1: Examples of circuit-QED experimental implementations of artificial atoms coupled to a photonic lattice of cavities, where the atoms are realized as a superconducting qubits and the lattice as an array of coupled microwave resonators. In (a) two artificial atoms (blue and red) are locally coupled to an array of 21 resonators (green), taken from [13]. In (b) a 5×5 Hofstadter lattice of resonators is coupled to a single qubit on the edge (blue) taken from [40].In (c) and (d) a giant atom (red) is coupled non-locally to a coupled cavity array (green) both taken from [33]

.

QED coupled-resonator lattices stand out as one of the most flexible and physically transparent architectures for exploring the next generation of engineered light–matter phenomena.

Scope of the thesis

The broader viewpoint developed above is also the one adopted in the original results presented in this thesis. Consistently with the title, the unifying theme of the thesis is the study of the emission dynamics of a qubit coupled to photonic lattices whose properties are controlled by *synthetic potentials*. Here, the term synthetic potential is understood in a broad sense: it refers to engineered spatial variations of the photonic lattice parameters, such as cavity-frequency gradients, sublattice detunings, or domain walls, which act on photons as effective potentials and reshape the reservoir seen by the emitter. The central question is how these synthetic potentials modify the emission properties of a qubit when the photonic environment is not a featureless continuum, but a lattice bath with an engineered band structure and spatial mode profile.

Throughout the thesis, the focus is on the single-excitation regime. This setting is simple enough to allow a microscopic description of the joint qubit–photon dynamics, yet rich enough to reveal non-Markovian emission, reversible atom–photon exchange, directional propagation, and topological effects. In this regime, the emitted photon can be followed explicitly as it evolves through the lattice, while the qubit dynamics retains a direct memory of the spectral and spatial structure of the bath. The synthetic potential therefore does not merely shift the photonic frequencies; it changes the way in which the excitation explores the lattice and can feed back onto the emitter.

The first line of work considers a qubit coupled to a *one-dimensional* coupled-cavity array in the presence of a *linear synthetic frequency gradient*. In this case, the site-dependent cavity frequency acts as a constant effective force on the emitted photon. Therefore, the photon undergoes Bloch-like oscillatory motion across the finite photonic band, and the qubit can display non-Markovian dynamics with revivals even though no physical mirrors are present [42]. This shows that a synthetic force, combined with the finite bandwidth of the lattice, can generate an effective delayed feedback mechanism. Depending on the strength of the force, the emission process ranges from reversible, cavity-like vacuum Rabi oscillations to a delayed-feedback regime in which the emitted photon returns to the qubit after a Bloch period and partially re-excites it.

The second line of work moves to a *two-dimensional* photonic lattice, where the synthetic potential is implemented through a *(generally non-uniform) sublattice detuning* in a honeycomb resonator array. A uniform detuning opens a gap and endows the lattice modes with valley-dependent geometrical properties, while a spatially varying detuning creates a domain wall supporting valley-polarized edge modes. In this structured bath, a giant atom is coupled nonlocally to several lattice sites, so that interference between the different coupling points acts as a momentum-space filter. This makes it possible to select a single photonic valley and, near a domain wall, to achieve chiral emission into valley-polarized edge modes [43]. In this case, the synthetic potential shapes the topology and spatial localization of the available photonic modes, while the nonlocal emitter–field coupling selects which of these modes are addressed.

These two studies can therefore be understood in some sense as complementary realizations of the same general idea: synthetic potentials in photonic lattices provide a flexible way to engineer the reservoir responsible for qubit emission. In the one-dimensional case, the synthetic potential controls the photon dynamics in time and produces effective feedback through Bloch oscillations. In the two-dimensional case, it controls the band geometry and creates topological interfaces supporting directional edge propagation. The thesis thus explores how the combination of lattice band structure, synthetic potentials and engineered light–matter coupling can give rise to emission phenomena that are absent in conventional quantum-optical reservoirs, including non-Markovian revivals, cavity-like dynamics without physical cavities, and chiral single-photon emission.

Thesis outline

The core of the thesis consists of one preliminary chapter, Chapter 2, which introduces the theoretical background used throughout the work, followed by two chapters presenting the *original results*, Chapters 3 and 4.

More specifically, Chapter 2 reviews the basic tools of light–matter interaction in structured photonic reservoirs. It introduces the atom–field Hamiltonian, the rotating-wave approximation, the single-excitation formalism, spontaneous emission, vacuum Rabi oscillations, non-Markovian emission with time delays, coupled-cavity arrays, synthetic potentials, giant atoms, and topological photonic lattices.

Chapter 3 presents the first original contribution of the thesis. It studies the emission dynamics of a qubit coupled to a one-dimensional coupled-cavity array in the presence of a linear synthetic potential. The resulting synthetic force accelerates the emitted photon across the finite photonic band, giving rise to Bloch oscillations and to a non-Markovian qubit dynamics with revivals. Depending on the strength of the force, the system exhibits either chiral vacuum Rabi oscillations or a delayed-feedback dynamics analogous to that of an atom coupled to a multimode cavity.

Chapter 4 presents the second original contribution of the thesis. It investigates a giant atom non-locally coupled to a two-dimensional honeycomb photonic lattice with broken inversion symmetry. The interference between the different coupling points enables selective coupling to a single photonic valley. In the presence of a domain wall supporting valley-polarized edge modes, this mechanism leads to chiral emission of single photons without requiring time-reversal-symmetry breaking in the photonic bath.

Finally, Chapter 5 summarizes the main results of the thesis and discusses possible future directions, including time-dependent synthetic forces, multiband lattices, many-emitter extensions, and arrays of valley-selective giant atoms.

Chapter 2

Background Theory and Methods

This chapter develops the theoretical background on which the rest of the thesis builds. We begin by deriving the atom-field Hamiltonian under the rotating-wave approximation at Section 2.1 and reduce the many-body problem to the single-excitation sector at Section 2.2. We then study spontaneous emission in a variety of photonic environments, from infinite waveguides to finite waveguides where the edge play the role of mirrors, where the finite propagation time of emitted light gives rise to non-Markovian feedback at Section 2.3. The subsequent sections introduce the structured photonic baths central to this thesis: coupled-cavity arrays and their dispersion relation at Section 2.6, the same arrays subject to a synthetic force and the resulting Bloch oscillations at Section 2.7, and lattices with non-trivial band topology at Section 2.9. Finally, we discuss giant atoms, emitters that couple to a photonic bath at multiple spatially separated points, and show how their interference properties lead to directional emission at Section 2.8.

2.1 Atom-field Hamiltonian

2.1.1 Quantized electromagnetic field

To quantize the electromagnetic field, very similarly to the quantization of the vibrational field in solids, one first works out the field's normal modes each labeled by k and the related normal frequencies ω_k[1]. The field's classical Hamiltonian in terms of such normal modes has the form of a sum of independent fictitious harmonic oscillators, one for each normal mode k and with frequency ω_k, each expressed in terms of a pair of fictitious position and related conjugate momentum x_k and p_k. One thus quantize all these operators using the standard commutation rule $[x_k, p_k] = i\hbar$, hence converting the total field Hamiltonian into a sum of independent *quantum* harmonic oscillator Hamiltonians as

$$H_f = \sum_k \hbar\omega_k a_k^\dagger a_k$$

[1] Index k is to be generally intended as a set of indexes. In free space, for instance, the field's normal modes are plane waves labeled by $\mathbf{k} = (k_x, k_y, k_z)$ and a polarization index. Thus k for now must be intended as just set the of indexes (continuous and discrete) that label the field's normal modes. This notation is suitable for our goals since the most relevant systems we will focus on feature 1D fields of fixed polarization such that k is a scalar quasi-momentum.

with ladder operators $\{a_k\}$ fulfilling the commutation rules $[a_k, a^\dagger_{k'}] = \delta_{kk'}$ (operators of different normal modes, $k \neq k'$, commute).

We define number or Fock states the multi-mode generalization of the standard number states of the quantum harmonic oscillator

$$|\{n_k\}\rangle = |n_1\rangle \otimes |n_2\rangle \otimes ... = |n_1,\, n_2,\, ...\rangle \tag{2.1}$$

with $n_k = 0, 1, 2, ..$such that

$$a_q\,|\{n_k\}\rangle = \sqrt{n_q}\,|n_1,\, n_2,\, ..., n_q - 1,\, ...\rangle\,,\;\; a^\dagger_q\,|\{n_k\}\rangle = \sqrt{n_q + 1}\,|n_1,\, n_2,\, ..., n_q + 1,\, ...\rangle$$

and

$$a^\dagger_q a_q\,|\{n_k\}\rangle = n_q\,|\{n_k\}\rangle\;\; .$$

Based on the form of H_f, the Fock states are just the stationary states of the field with the corresponding energy spectrum given by

$$E_{\{n_k\}} = \sum_k n_k \hbar\omega_k\,,$$

where we set to zero the vacuum energy $\sum_k \hbar\omega_k/2$ since this plays no role for the physics under study in the present thesis. From now on, we will set always $\hbar = 1$ in this thesis (so that e.g. the energy of a photon populating the kth mode is now just given by ω_k).

A Fock state contains a *well-defined* number of photons, in particular each Fock state has n_q photons in the qth normal mode each with energy ω_q. The total number of photons in state $|\{n_k\}\rangle$ is thus $\sum_k n_k$. An especially important are *single-photon* Fock states: each of these features only *one* photon populating a certain field's mode q. Accordingly, it can be labeled with just q and is given by

$$|q\rangle = a^\dagger_q\,|0\rangle\;\;(\text{single}-\text{photon Fock state})\,.$$

2.1.2 Atom

An atom for our purposes can be considered as a collection of electrons fully confined within a limited region of space due to an attractive potential. Accordingly, the energy spectrum of an atom is *discrete* and its stationary states are all bound (i.e. normalizable):

$$H_a = \omega_g\,|g\rangle\langle g| + \sum_\nu \omega_{e_\nu}\,|e_\nu\rangle\langle e_\nu|$$

with $|g\rangle$ the ground state and $|e_\nu\rangle$ excited states such that $\omega_{e_\nu} > \omega_g$ with ω_g the ground-state energy. In a vast amount of atom-photon interaction phenomena, only a limited range of electromagnetic frequencies are involved in a way that the physics is dominated only by a single atomic transition, say $|g\rangle \leftrightarrow |e_\nu\rangle$ for a given ν. This typically happens when $\omega_{e_\nu} - \omega_g$ (transition frequency) is close to the electromagnetic frequencies entering the problem under study (all the remaining transitions are not involved being far-detuned).

In such typical cases, we can approximate the atom as a *two-level system* featuring a ground state $|g\rangle$ and an excited state $|e\rangle$

$$H_a \simeq \omega_g |g\rangle\langle g| + \omega_e |e\rangle\langle e| \ .$$

This is an effective spin-1/2 system, hence we can conveniently define standard spin ladder operators

$$\sigma_+ = (\sigma_-)^\dagger = |e\rangle\langle g| \,, \tag{2.2}$$

such that the atomic Hamiltonian can be written as

$$H = \omega_0 \sigma_+ \sigma_- \,, \tag{2.3}$$

where we set $\omega_0 = \omega_e - \omega_g$ and set the energy zero in the ground state (frequency ω_0 from now on will be referred to as *atomic frequency*).

Typically, if $\hat{d}$ is the electric dipole operator[2], we have $\langle g|\hat{d}|g\rangle = \langle e|\hat{d}|e\rangle = 0$ since the operator is odd under spatial inversion and $|g\rangle$ ($|e\rangle$) typically have well-defined parity. However, the matrix element between the ground and excited state can be non-zero if the two states have opposite parity (this is the case we will assume, otherwise the considered transition would not be optically active) so that the dipole operator effectively reads

$$\hat{d} = d\,|g\rangle\langle e| + d^*\,|e\rangle\langle g| \ . \tag{2.4}$$

By absorbing the phase of d (if any) into the definition of $|e\rangle$ (which can always be done and has no effect on H_a), Eq. (2.4) becomes

$$\hat{d} = d\,(\sigma_+ + \sigma_-)\,. \tag{2.5}$$

with $d > 0$.

2.1.3 General form of the atom-field Hamiltonian

It can be shown that, so long as one considers typical field's wavelengths which are much longer than the atomic size (electric-dipole approximation), the atom-field Hamiltonian has the form (see Appendix for some more details)

$$H = H_a + \sum_k \omega_k a_k^\dagger a_k - \hat{d}\cdot\hat{E} \tag{2.6}$$

with $\hat{E}$ the electric field operator at the atomic position (which is a fixed parameter).

Notice that the atom couples to the field solely via its electric-dipole moment consistently with the above approximation (lowest-order non-zero term in the multipole expansion).

Approximating now the free atomic Hamiltonian simply as (2.3) (for the reasons described above), using (2.5) and recalling that, once expanded into the field's normal modes, the electric field $\hat{E}$ results in terms $\sim (a_k^\dagger - a_k)$, we end up with Hamiltonian

$$H = \omega_0 \sigma_+ \sigma_- + \sum_k \omega_k a_k^\dagger a_k + \sum_k \left[g_k(\sigma_+ + \sigma_-)a_k + \text{H.c.}\right] \tag{2.7}$$

[2]The electric dipole operator is generally a vector, but we treat it as a scalar having in mind that we only consider a field of given polarization. Thus $\hat{d}$ is in fact the component of the electric dipole operator along the electric field's direction.

Such kind of Hamiltonians are generally known as "spin-boson Hamiltonians". Here, g_k is the coupling strength between the atom and mode k, which is typically $\propto$ the elecric dipole momentum d (as is reasonable) and the kth *mode function* at the atom's position[3]. The latter, loosely speaking, measures the field amplitude of the considered kth mode at the atom's position.

2.1.4 Rotating-wave approximation

The rotating-wave approximation (RWA) is ubiquitous in quantum and classical optics and will be throughout this thesis. The RWA consists in neglecting the so called counter-rotating terms $\sim \sigma_- a_k$ and $\sim \sigma_+ a_k^\dagger$ in the interaction terms of Hamiltonian (2.7), keeping only terms $\sim \sigma_- a_k^\dagger$ and $\sim \sigma_+ a_k$ (containing an annihilation and a creation ladder operator).

To justify the RWA, we define $H_0 = H_a + H_f$ and $V = \sum_k [g_k(\sigma_+ + \sigma_-)a_k + \text{H.c.}]$ (so that $H = H_0 + V$). We next jump to the interaction picture with respect to H_0. In this picture, ladder operators become time-dependent[4] (they "rotate"): $\sigma_- \to \sigma_- e^{-i\omega_0 t}$ and $a_k \to a_k e^{-i\omega_k t}$, while the joint atom-field state $|\Psi_t\rangle$ evolves as

$$\frac{d}{dt}|\Psi_t\rangle = -i\, V_t\, |\Psi_t\rangle \tag{2.8}$$

with the effective time-dependent Hamiltonian given by

$$V_t = e^{iH_0 t}\, V\, e^{-iH_0 t} = \sum_k g_k(\sigma_+ a_k e^{-i(\omega_k - \omega_0)t} + \sigma_- a_k e^{-i(\omega_k+\omega_0)t}) + \text{H.c.} \tag{2.9}$$

Now, in the vast majority of matter-light systems, the atom-field coupling is *weak*. Concretely, this means that $g_k \ll \omega_0$[5]. One can see that, without the rotating exponentials, the characteristic time scale of the dynamics would be $\sim g_k^{-1}$ (inverse of the interaction strength)[6]. It follows that, so long as we look at evolution times of the order of $\sim g_k^{-1}$ (or longer), which is typically what we are interested in, terms $\sim e^{-i(\omega_k+\omega_0)t}$ rotate very quickly since

$$\omega_0 + \omega_k > \omega_0 \gg g_k$$

in a way that they do not significantly contribute to the dynamics (since they average to zero in a time interval $\sim g_k^{-1}$). This justifies why these counter-rotating terms can be neglected. Finally, going back to the Schrödinger picture, we are left with the atom-field Hamiltonian

$$H = \omega_0 \sigma_+ \sigma_- + \sum_k \omega_k a_k^\dagger a_k + \sum_k (g_k\, \sigma_- a_k^\dagger + \text{H.c.})\,. \tag{2.10}$$

Hamiltonian (2.10) is the basic Hamiltonian that we will use throughout this thesis (and which is used in the vast majority of quantum optics literature).

Before concluding, it is worth noting that, after dropping counter-rotating terms in (2.9), among the rotating terms the biggest contribution to the dynamics comes from

[3] For instance, in free space mode functions are plane waves $\frac{e^{i\mathbf{k}\cdot\mathbf{r}}}{\sqrt{V}}$, which could be thought as well as the stationary-state wavefunctions of a single photon.

[4] A generic operator $\hat{A}$ evolves in time according to $\dot{\hat{A}} = i[H_0, \hat{A}]$.

[5] We use g_k for simplicity, although in general it should be $|g_k|$

[6] Actually, the rigorous statement is that the characteristic time scale is $\geq \min_k g_k^{-1}$

modes k such that $|\omega_k - \omega_0| \lesssim g_k$. Based on a resonance argument, one can see that this is reasonable: the atom is mostly sensitive to modes k, whose frequency differ from ω_0 by the coupling strength g_k. These are the modes that play a role in the dynamics.

With the atom-field Hamiltonian in its final form (2.10), we are ready to study the dynamics it governs. The key simplification brought by the RWA is a conservation law that dramatically reduces the complexity of the problem, as we now discuss.

2.2 Single-excitation dynamics

The RWA endows Hamiltonian (2.10) with a major property, which is the *conservation of the total number of excitations.* This conservation law is a tremendous simplification of many quantum optics problems, including those which will be the focus of the present thesis.

2.2.1 Conservation of the total number of excitations

Let $\hat{N} = \sigma_+\sigma_- + \sum_k a_k^\dagger a_k$, or equivalently $\hat{N} = |e\rangle\langle e| + \sum_k a_k^\dagger a_k$, be the total number of "excitations". This noun is intended in the following sense. When the atom is in state $|e\rangle$ and the field is in vacuum, we say that there is one excitation (which in this specific case lies on the atom; the field having zero excitations). Indeed, this state is an eigenstate of operator $\hat{N}$ with eigenvalue 1

$$\hat{N}(|e\rangle\,|\text{vac}\rangle) = (\sigma_+\sigma_-\,|e\rangle)\,|\text{vac}\rangle = |e\rangle\,|\text{vac}\rangle$$

This is also the case when the field is in any single-photon state like $\sum_{k'} \psi_{k'} a_{k'}^\dagger\,|\text{vac}\rangle$ and the atom is in $|g\rangle$:

$$\hat{N}\left(|g\rangle \sum_{k'} \psi_{k'} a_{k'}^\dagger\,|\text{vac}\rangle\right) = |g\rangle \left(\sum_k a_k^\dagger a_k \sum_{k'} \psi_{k'} a_{k'}^\dagger\,|\text{vac}\rangle\right) = |g\rangle \sum_{k'} \psi_{k'} a_{k'}^\dagger\,|\text{vac}\rangle \tag{2.11}$$

(the difference being that the excitation is now in the field). If, instead, the field is in a single-photon state and the atom is in $|e\rangle$ then we have two excitations (i.e. $N = 2$) and so on.

Now it can be checked easily that Hamiltonian (2.10) commutes with $\hat{N}$. The reason why this happens is that any term appearing in H manifestly conserves the total number of excitations since it is a product of a raising and a lowering ladder operator (atomic or photonic). Therefore, H can be block-diagonalized each block corresponding to an eigenspace of $\hat{N}$[7]. Another notable consequence is that if we start with a joint state lying fully within a given eigenspace of $\hat{N}$, the evolved state at any time is ensured to remain in the same subspace.

[7]The eigenspace corresponding to $N = 0$ is trivial, consisting of the only state $|g\rangle\,|\text{vac}\rangle$ (which is also the total ground state of the system).

2.2.2 Single-excitation subspace

Especially important is the eigenspace $N = 1$, the so called *single-excitation subspace* (or single-excitation sector) which we will call $\mathcal{H}_1$. This is spanned by the basis

$$\{|e\rangle\,|\mathrm{vac}\rangle\,,\ |g\rangle\, a_k^\dagger\,|\mathrm{vac}\rangle\}\,. \tag{2.12}$$

Many quantum optics phenomena – in particular *linear*/"low power" quantum optics – involve only single-excitation dynamics and this will be the case also in this thesis. For this reason, it is convenient to introduce a compact notation for the aforementioned basis defined by the following replacements

$$|e\rangle\,|\mathrm{vac}\rangle \to |e\rangle\ ,\quad |g\rangle\, a_k^\dagger\,|\mathrm{vac}\rangle \to |k\rangle\,. \tag{2.13}$$

Thus our basis for the single-excitation sector $\mathcal{H}_1$ reads $\{|e\rangle\,, \{|k\rangle\}\}$.

2.2.3 Equations of motion in the single-excitation sector

If we start with a joint state $|\Psi(0)\rangle$ lying fully within the single-excitation sector, then the joint state at any time $|\Psi(t)\rangle = e^{-iHt}\,|\Psi(0)\rangle$ will be in the same eigenspace. Accordingly, based on the previous section, the latter can be expanded as

$$|\Psi(t)\rangle = \alpha_e(t)\,|e\rangle + \sum_k \alpha_k(t)\,|k\rangle\ . \tag{2.14}$$

Here, $\alpha_e(t)$ and $\alpha_k(t)$ are the (generally complex) probability amplitudes to find the system in state $|e\rangle$ and $|k\rangle$, respectively, at time $t \geq 0$. Thus the set of coefficients $\{\alpha_e(t),\, \{\alpha_k(t)\}\}$ fully specify the joint state at time t.

To derive how $|\Psi(t)\rangle$ evolves in time, we write down the (time-dependent) S.E.

$$\frac{d}{dt}\,|\Psi(t)\rangle = -iH\,|\Psi(t)\rangle\ .$$

Replacing $|\Psi(t)\rangle$ with (2.14) and H with (2.10) yields the system of coupled differential equations

$$\dot{\alpha}_e = -i\omega_0\alpha_e - i\sum_k g_k^*\,\alpha_k\,,\quad \dot{\alpha}_k = -i\omega_k\alpha_k - ig_k\alpha_e \tag{2.15}$$

(note that we have an equation like the latter one for each value of k). It is convenient to measure energies from ω_0, which yields

$$\dot{\alpha}_e = -i\sum_k g_k^*\,\alpha_k\,,\quad \dot{\alpha}_k = -i(\omega_k-\omega_0)\alpha_k - ig_k\alpha_e\,. \tag{2.16}$$

We now conveniently express the same equations in the Laplace domain (see Appendix A) by taking the Laplace transform of either side of each equation

$$s\,\tilde{\alpha}_e - 1 = -i\sum_k g_k^*\tilde{\alpha}_k\,,\quad s\,\tilde{\alpha}_k = -i(\omega_k-\omega_0)\tilde{\alpha}_k - ig_k\tilde{\alpha}_e \tag{2.17}$$

[we do not show the argument "(s)" to make notation lighter]. An emission process (by definition) starts with the atom in the excited state and the field in the vacuum state, which is why we set $\alpha_e(0) = 1$ (initial condition). Solving the latter equation for $\tilde{\alpha}_k(s)$ gives[8]

$$\tilde{\alpha}_k = -i \, \frac{g_k}{s + i(\omega_k - \omega_0)} \, \tilde{\alpha}_e \, . \tag{2.18}$$

Once this is plugged in the former equation, we get a closed equation in the only unknown function $\tilde{\alpha}_e(s)$

$$s \, \tilde{\alpha}_e - 1 = -\tilde{F} \, \tilde{\alpha}_e \tag{2.19}$$

with $\tilde{F}$ standing for

$$\tilde{F}(s) = \sum_k \frac{|g_k|^2}{s + i(\omega_k - \omega_0)} \tag{2.20}$$

To analyze the physical meaning of this equation we go back to the time domain. By using basic properties of the Laplace transform (see Appendix A), Eq. (2.19) which returns the integro-differential equation

$$\frac{d\alpha_e}{dt} = -\int_0^t d\tau \, F(\tau) \, \alpha_e(t - \tau) \, . \tag{2.21}$$

with $F(\tau)$ given by

$$F(\tau) = \sum_k |g_k|^2 \, e^{-i(\omega_k - \omega_0)\tau} \;\; \text{(memory kernel)} \tag{2.22}$$

This equation governs, formally, the most general emission process of the atom as a function of the field structure (this being given by the coupling strengths function g_k and the dispersion law ω_k). A key property of this equation of motion is that it is non-local in the time domain: unlike a usual S.E. where $\frac{d\alpha_e}{dt}$ depends only on the current value of amplitude $\alpha_e(t)$, one can see that here it depends also on *past* values $\alpha_e(t - \tau)$ (in principle up to the initial time $t = 0$ i.e. $\tau = t$). This means that knowing $\alpha_e(t)$ alone is not sufficient to determine $\alpha_e(t+dt)$[9]. In this sense, we say that the system has "memory" or, in more rigorous terms, it is *non-Markovian*. This is a general fact: any open system (i.e. coupled to an external environment) is in general non-Markovian[10]. In the present case, the degree of non-Markovian behaviour is captured by the "memory kernel" function of τ. Typically, when the field has many degrees of freedom (e.g. the continuous electromagnetic field in free space) [11], this is a function which eventually decays with τ, the associated characteristic decay time thus behaving as a memory time: the slower the decay of the memory kernel (i.e. the longer the memory time), the more non-Markovian the system is.

[8] Notice the convenience in using Laplace transforms, which in fact turns our differential system into algebraic equations.

[9] For a S.E. -like equation, which is time local, this would instead be sufficient. This can be seen by setting $g_k = 0$ (meaning that the atom decouples from the field), in which case the equation of motion reduces to $\dot{\alpha}_e(t) = -i\omega_0\alpha_e(t)$ (time local).

[10] This is also true in classical mechanics, where however the study of non-Markovianity is far less problematic than the quantum counterpart.

[11] This is not necessarily the case as for a single-mode cavity (typical cavity-QED setup), which we will discuss later.

2.3 Spontaneous emission

The most natural, and in some respects inevitable, consequence of coupling an atom to an electromagnetic *continuum* is *spontaneous emission* (SE)[12]. This consists of the emission of a single photon from an initially excited atom, during which the probability of finding the atom in the excited state decays *exponentially* in time with a characteristic decay rate γ. Despite its ubiquity, spontaneous emission is a Markovian process with zero memory time, and therefore a special case of the general non-Markovian behaviour described in the previous section — specifically the limit in which the memory kernel decays to zero on a timescale much shorter than the atomic dynamics.

One way to explain why SE occurs is to use the theoretical framework in the previous section in the case that the field is a smooth continuum of modes (thus k and ω_k can become continuous variables in the thermodynamic limit) which coupled weakly to the atom. It turns out that very often, and in particular in free space, the coupling function $|g_k|$ only depends on k through the photon energy, in which case we can set $|g_k| = |g(\omega_k)|$[13].

In these cases, one can conveniently turn the memory kernel $F(\tau)$ in (2.21) into an integral over the continuous frequency ω as

$$F(\tau) = \sum_k |g_k|^2 \, e^{-i\omega_k \tau} = \int_{\omega_{\min}}^{\omega_{\max}} d\omega \, \rho(\omega) \, |g(\omega)|^2 \, e^{-i\omega\tau} \tag{2.23}$$

with $\rho(\omega)$ the density of electromagnetic modes (per unit frequency)[14]. In general terms, the integral over ω extends over a *lower*-bounded interval (i.e. $\omega_{\min}$ is finite), which can be upper-*un*bounded (i.e. $\omega_{\max}$ is infinite; as e.g. in free space) or upper-bounded (when $\omega_{\max}$ is finite, as e.g. in a photonic lattice as we will see later on). It is understood that ω_0 lies *within* the range $[\omega_{\min}, \omega_{\max}]$

Correspondingly, in the Laplace domain [cf. (2.20)]

$$\tilde{F}(s) = \int_{\omega_{\min}}^{\omega_{\max}} d\omega \, \frac{\rho(\omega)\, |g(\omega)|^2}{s + i(\omega - \omega_0)} \,, \tag{2.24}$$

which can be written as

$$\tilde{F}(s) = -i \int_{\omega_{\min}}^{\omega_{\max}} d\omega \, \frac{\rho(\omega)\, |g(\omega)|^2}{\omega - \omega_0 - is} \tag{2.25}$$

We expect that - for *weak coupling* - the dominant contribution to the dynamics comes from modes nearly-resonant with the atom, namely those at frequencies $\omega \simeq \omega_0$. Accordingly, we replace $s \to -0^+$

$$\tilde{F}(s) \simeq -i \int_{\omega_{\min}}^{\omega_{\max}} d\omega \, \frac{\rho(\omega)\, |g(\omega)|^2}{\omega - \omega_0 + i0^+} \,, \tag{2.26}$$

which makes $\tilde{F}(s)$ independent of s and ω_0 a pole of the integrand function. Applying

[12] A typical challenge of quantum optics is in a sense to investigate conditions in which spontaneous emission does *not* occur.

[13] More generally, instead of $|g(\omega_k)|^2$ one can sum $|g_{k'}|^2$ over all modes k' such that $\omega = \omega_{k'}$, which defines a function of ω only. Notice that one can arrange $F(\tau)$ as a continuous integral even for field comprising a set of discrete modes, in which cases $\rho(\omega)$ will be a sum of Dirac Delta function.

[14] In general, $g(\omega)$ can depend on the atom's position.

the residue theorem,

$$\tilde{F}(s) \simeq -i\left[\underbrace{\mathrm{PV}\int_{\omega_{\min}}^{\omega_{\max}} d\omega\, \frac{\rho(\omega)\,|g(\omega)|^2}{\omega-\omega_0}}_{=\Delta_L} + i\,\underbrace{\pi\rho(\omega_0)|g(\omega_0)|^2}_{=\gamma}\right] = i\Delta_L + \gamma\,, \tag{2.27}$$

where we defined the Lamb shift Δ_L and decay rate

$$\begin{aligned}\Delta_L &= \mathrm{PV}\int_{\omega_{\min}}^{\omega_{\max}} d\omega\, \frac{\rho(\omega)\,|g(\omega)|^2}{\omega-\omega_0}\,,\\ \gamma &= \pi\rho(\omega_0)|g(\omega_0)|^2\,.\end{aligned} \tag{2.28}$$

Replacing in Eq. (2.19) and solving for $\tilde{\alpha}_e(s)$

$$\tilde{\alpha}_e(s) = \frac{1}{s - i\Delta_L + \gamma}\,, \tag{2.29}$$

Transforming back to the time domain we finally get

$$\alpha_e(t) = e^{-(i\Delta_L+\gamma)t} = e^{-i\Delta_L t}e^{-\gamma t} \tag{2.30}$$

which in fact means (recall that we set $\omega_0 = 0$)

$$\alpha_e(t) = e^{-i(\omega_0+\Delta_L)t}\,e^{-\gamma t} \to |\alpha_e(t)|^2 = e^{-2\gamma t}\,. \tag{2.31}$$

We thus get that the atomic population exponentially decays to zero.

We point out the key (more or less implicit) ingredients[15] to get spontaneous emission:

(1) Weak coupling;

(2) *Continuum* of field frequencies;

(3) Atomic frequency ω_0 well inside the photonic continuum;

(4) Function $\rho(\omega)|g(\omega)|^2$ smooth around ω_0.

Notice that (4) is important and in practice means that ω_0 must be enough away from singularities of the field's density of states $\rho(\omega)$.

2.3.1 Local density of states

Since we study atoms emitting into photonic baths, it is fundamental to measure the number of photonic modes available at a given position $\mathbf{r}$ and frequency ω. The quantity that enables us to perform this quantification is the *local density of states* (LDoS), which is defined as follows,

$$\rho(\mathbf{r},\omega) = \sum_k |\langle \mathbf{r}|\psi(k)\rangle|^2\delta(\omega-\omega_k) \tag{2.32}$$

[15]The "length" of this list might be somewhat misleading: these conditions occur very naturally. Breaking them requires "engineering" the field appropriately as we will see.

where $|\psi(k)\rangle$ is the normal mode and ω_k is the dispersion relation.

Now, if we consider an atom, in the excited state, with frequency ω_0 coupled to a position $\mathbf{r}_0$, we saw by Section 2.3 that this atom will undergo spontaneous emission. One can compute the decay rate Γ of this emission by using the LDoS,

$$\Gamma = 2\pi g^2 \rho(\mathbf{r}_0, \omega_0) \tag{2.33}$$

2.4 Vacuum Rabi oscillations

We now consider the opposite extreme, in which the field consists of a single mode rather than a continuum. This occurs when, instead of a continuum, the field features just *one mode*. A dynamics where only a single mode of the field interacts with a single atom can be realized by putting the atom inside a high-finesse cavity[16]. Inside the cavity, only discrete modes exist with wavevectors $k_m = m\pi/L$ (L is the cavity length) and frequencies $\omega_m = vk_m$. If the cavity is sufficiently small, the spacing $\omega_{m+1} - \omega_m$ will be easily much larger than the atom-photon coupling strength g so that the atom will in fact interact only with the cavity mode of frequency closest to ω_0, which we will call ω_c. Thus the differential system (2.16) in this case reduces to

$$\dot{\alpha}_e = -i\omega_0\alpha_e - ig\alpha_c\,, \quad \dot{\alpha}_c = -i\omega_c\alpha_c - ig\alpha_e \tag{2.34}$$

(we dropped index k in α_k and g_k since there is now only one mode with g real). Correspondingly, Eq. (2.21)

$$\frac{d\alpha_e}{dt} = -i\omega_0\alpha_e(t) - \int_0^t d\tau\, \underbrace{\left(g^2\, e^{-i\omega_c\tau}\right)}_{\text{memory kernel}}\, \alpha_e(t-\tau)\,. \tag{2.35}$$

Notice that in this dynamics the memory-kernel function (modulus) does not decay at all, which witnesses a generally strongly non-Markovian behaviour. Accordingly, now we do not expect the atomic excitation to undergo an irreversible decay, i.e. we do not expect spontaneous emission to happen.

Eq. (2.34) is a system of two coupled linear differential equations which can be easily solved. To make things simple and understand what is going on, let us consider the resonance condition $\omega_c = \omega_0$, in which case one easily finds that [for the initial condition $\alpha_e(0) = 1$ and $\alpha_c(0) = 0$] the solution is

$$\alpha_e(t) = e^{-i\omega_0 t}\cos(2gt)\,, \quad \alpha(t) = -ie^{-i\omega_0 t}\sin(2gt)\,, \tag{2.36}$$

which implies that the probability to find the atom in $|e\rangle$ and the cavity with one photon are respectively given by

$$p_e(t) = |\alpha_e(t)|^2 = \cos^2(2gt)\,, \quad p_c(t) = |\alpha_c(t)|^2 = \sin^2(2gt) \tag{2.37}$$

(note that $p_e(t) + p_c(t) = 1$ at any time). This phenomenon is called *vacuum Rabi oscillations* and marks an extreme departure from spontaneous emission. Unlike spon-

[16] Serge Haroche was awarded the Nobel prize for realizing such kind of revolutionary experiments (the first ones around the 80s). He used Rydberg atoms entering one at a time in a cavity made out of highly-reflective superconducting mirrors.

taneous emission, we see that the atom at first decays until it ends up in the ground state (at $2gt = \pi/2$, i.e. $t = \pi/4\, g^{-1}$) and is subsequently re-excited until returning to the initial state $|e\rangle$ at time $2gt = \pi$, i.e. $t = \pi/2\, g^{-1}$. Correspondingly, a photon is first emitted into the cavity but then reabsorbed again by the atom (as witnessed by the behaviour of $p_c(t)$, which first increases and then returns to zero). This phenomenon then repeats periodically, the oscillation frequency being called the *vacuum Rabi frequency* $\Omega = 2g$. Therefore, in stark contrast to the irreversible nature of spontaneous emission, here the emission dynamics is fully reversible.

The two cases studied so far, a continuum field and a single cavity mode, represent opposite extremes. In between lies a broad and physically important regime in which the emitter couples to an extended structured bath with finite spatial extent. There, the emitted field can travel through the bath, reflect off a boundary, and return to the atom after a finite propagation time. This delayed feedback is the origin of the non-Markovian dynamics studied in the next section.

2.5 Non-Markovian emission due to photonic time delays

A paradigmatic setting in which retardation effects become important is a two-level atom coupled to a semi-infinite one-dimensional waveguide. The waveguide is terminated by a reflecting boundary, which can be idealized as a perfect mirror. An atom placed at a distance x_0 from the mirror emits into the guided modes; the component emitted towards the mirror is reflected and can interact again with the atom after a finite propagation time. This geometry provides a minimal realization of coherent time-delayed feedback and is closely related to the giant-atom problem, with the important difference that the second interaction with the field is generated by reflection at a boundary rather than by a second spatial coupling point.

We consider a two-level atom as reviewed in Section 2.1.2. In the rotating-wave approximation, the atom-field Hamiltonian given by Eq. (2.10) can be written for a continuum of frequencies as,

$$H = \omega_0 \sigma_+ \sigma_- + \int d\omega\, \omega\, a^\dagger_\omega a_\omega + \int d\omega\, \left[g(\omega)\sigma_+ a_\omega + g^*(\omega) a^\dagger_\omega \sigma_- \right]. \tag{2.38}$$

The main effect of the semi-infinite geometry is encoded in the frequency-dependent coupling $g(\omega)$. Because the electromagnetic field satisfies a boundary condition at the mirror, the normal modes are not simple travelling waves but standing-wave-like modes. Equivalently, by the method of images, the reflected field may be interpreted as radiation emitted by an image atom located symmetrically beyond the mirror.

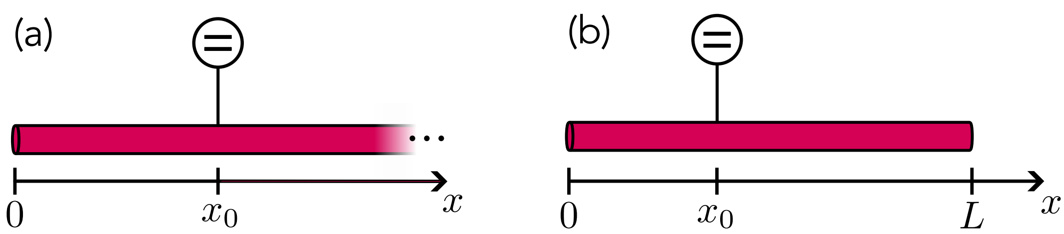

Figure 2.1: Atom coupled to (a) a semi-infinite waveguide, (b) a finite waveguide.

Assuming a linear dispersion relation around the atomic resonance,

$$\omega_k \simeq \omega_0 + v_g(k - k_0), \tag{2.39}$$

the relevant propagation time is the round-trip time between the atom and the mirror,

$$\tau = \frac{2x_0}{v_g}. \tag{2.40}$$

The corresponding resonant propagation phase is

$$\phi = \omega_0\tau = 2k_0x_0, \tag{2.41}$$

up to an additional reflection phase determined by the boundary condition at the mirror.

The delayed nature of the feedback becomes particularly transparent in the single-excitation subspace. Since the rotating-wave Hamiltonian conserves the total excitation number,

$$N = \sigma_+\sigma_- + \int d\omega\, a_\omega^\dagger a_\omega, \tag{2.42}$$

an initial state $|e\rangle$ evolves within the sector

$$|\psi(t)\rangle = \alpha_e(t)\,|e\rangle + \int d\omega\, \alpha_\omega(t)\,|\omega\rangle\,. \tag{2.43}$$

Here $\alpha_e(t)$ is the excited-state amplitude and $\alpha_\omega(t)$ is the amplitude for having emitted one photon in mode ω. Eliminating the photonic amplitudes gives an exact integro-differential equation for the atomic amplitude,

$$\dot{\alpha}_e(t) = -\int_0^t dt'\, F(t-t')\alpha_e(t'), \tag{2.44}$$

where the memory kernel is given by Eq. (2.22), but we can write it for a continuum of frequencies as,

$$F(t-t') = \int d\omega\, |g(\omega)|^2 e^{-i(\omega-\omega_0)(t-t')}. \tag{2.45}$$

In a standard Markovian treatment, the kernel is approximated by a delta function, leading to exponential spontaneous decay. In the semi-infinite waveguide, however, the mirror introduces an additional contribution localized at the round-trip time τ. Under the usual wide-band approximation and linearization of the dispersion relation, the kernel takes the causal form

$$F(t-t') \simeq \frac{\gamma}{2}\delta(t-t') - \frac{\gamma}{2}e^{i\phi}\delta(t-t'-\tau), \tag{2.46}$$

where γ is the decay rate into the waveguide in the absence of retardation. The relative sign depends on the reflection phase and on the precise boundary condition imposed at the mirror.

The resulting equation for the excited-state amplitude is therefore a delay differential equation,

$$\dot{\alpha}_e(t) = -\frac{\gamma}{2}\alpha_e(t) + \frac{\gamma}{2}e^{i\phi}\alpha_e(t-\tau)\Theta(t-\tau), \tag{2.47}$$

up to conventions in the definition of γ and in the reflection phase. The first term describes the local-in-time emission into the waveguide, while the second term describes the field emitted at an earlier time, reflected by the mirror, and returning to the atom after the delay time τ. The Heaviside step function enforces causality: for $t < \tau$, the emitted field has not yet returned to the atom, and the dynamics is purely Markovian,

$$\alpha_e(t) = e^{-\gamma t/2}\alpha_e(0). \tag{2.48}$$

For $t > \tau$, the atom is driven by its own past emission. The quantity $\alpha_e(t-\tau)$ represents the atomic amplitude at the earlier time at which the returning field was emitted. Thus, the semi-infinite waveguide acts as a coherent feedback loop with memory time τ.

The phase ϕ controls the interference between the instantaneous emission and the reflected field. If the returning field is in phase with the atomic dipole, it can partially re-excite the atom and generate non-exponential decay or population revivals. If it is out of phase, it can interfere destructively with the emission process and suppress the decay. In the short-delay limit $\gamma\tau \ll 1$, one may approximate

$$\alpha_e(t-\tau) \simeq \alpha_e(t), \tag{2.49}$$

obtaining

$$\dot{\alpha}_e(t) \simeq -\frac{\gamma}{2}\left[1 - e^{i\phi}\right]\alpha_e(t). \tag{2.50}$$

This expression gives a position-dependent effective decay rate,

$$\Gamma_{\text{eff}} = \gamma\left[1 - \cos\phi\right], \tag{2.51}$$

together with a coherent frequency shift proportional to $\sin\phi$. Depending on the chosen convention for the mirror reflection phase, the decay rate may equivalently appear with $1 + \cos\phi$. The essential physical point is that, in the Markovian regime, the mirror modifies the local density of states at the atomic position, whereas in the retarded regime the finite propagation time must be kept explicitly.

The delay equation can be solved constructively by the method of steps. During the first interval $0 < t < \tau$, the delayed term is absent. During the second interval $\tau < t < 2\tau$, the delayed amplitude is already known from the first interval and acts as a source term. Iterating the construction yields

$$\alpha_e(t) = e^{-\gamma t/2}\sum_{n=0}^{\infty}\frac{\left[\frac{\gamma}{2}e^{\gamma\tau/2+i\phi}(t-n\tau)\right]^n}{n!}\Theta(t-n\tau). \tag{2.52}$$

The term $n = 0$ describes the initial spontaneous decay before the atom receives any feedback. The term $n = 1$ corresponds to the first reflected wave packet returning from the mirror. Higher-order terms describe repeated cycles of emission, propagation to the mirror, reflection, and reinteraction with the atom. The atomic dynamics is therefore organized into temporal echoes separated by the delay time τ.

The semi-infinite waveguide becomes a one-dimensional cavity when a second mirror is introduced. The system can then be regarded as a finite waveguide of length L, terminated by two reflecting boundaries. This geometry is a natural bridge between the time-delayed feedback picture and the standard cavity-QED description of spontaneous emission in a resonator. If the atom is located at position x_0 inside the cavity, a photon emitted by the atom can propagate to the left mirror, to the right mirror, or perform multiple round trips before interacting again with the atom. The electromagnetic environment therefore stores the emitted excitation and returns it to the atom through a sequence of delayed echoes.

In the two-mirror geometry there are several relevant propagation times. The delays associated with the first reflection from the left and right mirrors are

$$\tau_L = \frac{2x_0}{v_g}, \qquad \tau_R = \frac{2(L - x_0)}{v_g}, \tag{2.53}$$

while the full cavity round-trip time is

$$T = \frac{2L}{v_g}. \tag{2.54}$$

Consequently, the excited-state amplitude obeys a delay equation with multiple retarded contributions. Schematically,

$$\dot{\alpha}_e(t) = -\frac{\gamma}{2}\alpha_e(t) + \frac{\gamma_L}{2}e^{i\phi_L}\alpha_e(t-\tau_L)\Theta(t-\tau_L) + \frac{\gamma_R}{2}e^{i\phi_R}\alpha_e(t-\tau_R)\Theta(t-\tau_R) + \cdots . \tag{2.55}$$

The dots denote additional echoes generated by repeated cavity round trips. These terms involve delays of the form

$$\tau_L + nT, \qquad \tau_R + nT, \qquad n = 1, 2, \ldots, \tag{2.56}$$

with phases determined by the corresponding optical path lengths and by the reflection phases at the two mirrors. If the mirrors are not perfectly reflecting, each subsequent echo is weighted by the appropriate products of reflection amplitudes. For mirror reflection amplitudes r_1 and r_2, a contribution involving n complete round trips is suppressed by factors proportional to $(r_1 r_2)^n$.

This time-domain formulation is complementary to the usual normal-mode picture of cavity QED. In the frequency domain, the two mirrors impose boundary conditions that select a discrete set of longitudinal resonances. The atom couples most strongly to those modes whose spatial profile is nonzero at the atomic position. In the high-quality-factor limit, when a single cavity resonance dominates the interaction and the round-trip time is short compared with the characteristic atomic decay time, the feedback series can be resummed into the familiar single-mode cavity-QED model, with coherent atom-cavity coupling g and cavity loss rate κ. In that regime, the dynamics is usually described in terms of vacuum Rabi oscillations and cavity leakage rather than an explicit delay differential equation.

However, the delay formulation is more general for long cavities, lossy resonators, or situations in which several longitudinal modes participate in the dynamics. It makes explicit that the cavity is not simply a memoryless reservoir: it returns the emitted radiation to the atom after well-defined propagation times. The atom therefore interacts not only with instantaneous vacuum fluctuations, but also with a structured history of its own field. This is the physical origin of non-exponential decay, revivals, interference effects, and the breakdown of the Markov approximation in one-dimensional resonators, as discussed in early studies of spontaneous emission near mirrors and inside cavities [23, 44–48].

2.6 QED in coupled-cavity arrays

In the previous section, we studied spontaneous emission in various single-mode and continuum environments, including the non-Markovian feedback that arises when the emitted field can return to the atom after propagating through the photonic bath. In this section, we take a step further and consider an atom coupled to an extended one-dimensional array of coupled cavities. This new structure supports a photonic band and allows the emitted excitation to propagate through the lattice after the atom has decayed, opening a rich set of dynamical phenomena. To model this system, we

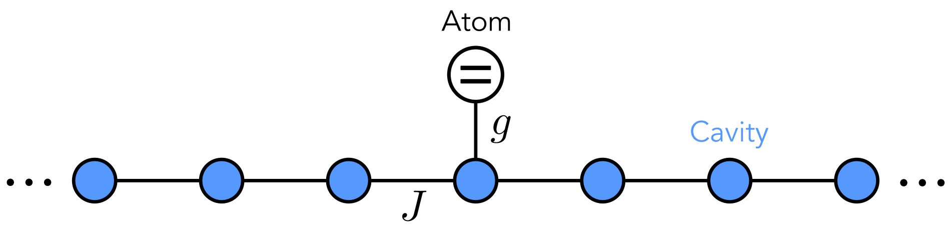

Figure 2.2: Two-level atom coupled with strength g to a homogeneous array of cavities. Photons can hop between cavities at a rate J.

can write the Hamiltonian of the lattice as

$$H = \sum_n \omega_c a_n^\dagger a_n - J \sum_n \left(a_{n+1}^\dagger a_n + \text{H. c.} \right) \tag{2.57}$$

where now a_n is the bosonic operator that annihilates a photon in a cavity that lies in the position n, ω_c is the cavity frequency, and J is the hopping rate between the cavities. In the single excitation sector, this Hamiltonian can be expressed as a tight-binding Hamiltonian,

$$H = \sum_n \omega_c |n\rangle\langle n| - J \sum_n \left(|n+1\rangle\langle n| + \text{H. c.} \right), \tag{2.58}$$

where $|n\rangle = a_n^\dagger |\text{vac}\rangle$ means a single photon at cavity n. Assuming periodic boundary conditions, we can use the Bloch theorem to write this Hamiltonian in the diagonal form

$$H = \sum_k \omega_k a_k^\dagger a_k = \sum_k \omega_k |k\rangle\langle k| . \tag{2.59}$$

where the dispersion relation is

$$\omega_k = \omega_c - 2J \cos k, \tag{2.60}$$

the eigenstates are,

$$|k\rangle = \frac{1}{\sqrt{N}} \sum_n e^{ikn} |n\rangle , \tag{2.61}$$

and N is the number of lattice sites. Now we introduce an atom coupled to the cavity at the position $n = 0$ [see Fig. 2.2], the Hamiltonian of the full system can be expressed as following,

$$H = \omega_0 \sigma_+ \sigma_- + \sum_n \omega_c a_n^\dagger a_n - J \sum_n \left(a_{n+1}^\dagger a_n + \text{H. c.} \right) + g \left(\sigma_- a_0^\dagger + \text{H. c.} \right) \tag{2.62}$$

In a similar fashion to what was done to the eigenstates at Eq. (2.61), one can write the annihilator operator in k space using the Bloch Theorem. Therefore, we represent $a_n = \frac{1}{\sqrt{N}} \sum_k e^{-ikn} a_k$. Then we can write the Hamiltonian as,

$$H = \omega_0 \sigma_+ \sigma_- + \sum_k \omega(k) a_k^\dagger a_k + \sum_k \frac{g}{\sqrt{N}} \left(\sigma_- a_k^\dagger + \mathrm{H.\,c.} \right). \tag{2.63}$$

We can compare this equation with the general atom-field Hamiltonian (2.10) and one can notice that the coupling strength $g_k = g/\sqrt{N}$ is constant for all the modes.

2.6.1 Spontaneous emission into an infinite array

In Section 2.6, we introduced the coupling between a qubit and a one-dimensional photonic bath. Here, we investigate the spontaneous emission dynamics of this system. In particular, we tune the atomic frequency inside the photonic band [see Fig. 2.3], such that the atom couples resonantly to two bath normal modes with wavevectors $\pm k_0$.

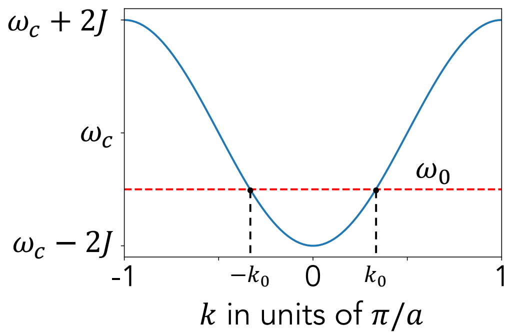

Figure 2.3: Dispersion relation of a homogeneous cavity array. The photonic band extends from $-2J$ to $2J$, centered around the cavity frequency ω_c. The atomic frequency ω_0, represented by the red dashed line, lies within the band and couples resonantly to the two modes $\pm k_0$.

To compute the decay rate, as discussed in Section 2.3.1, we first evaluate the local density of states (LDOS) at the position and frequency of the atom. From Eq. (2.32), we have

$$\rho(0, \omega_0) = \sum_k |\langle 0|k\rangle|^2 \delta(\omega_0 - \omega_k). \tag{2.64}$$

Using Eq. (2.61) together with the dispersion relation in Eq. (2.60), this expression becomes

$$\rho(0, \omega_0) = \frac{1}{N} \sum_k \left[\frac{\delta(k - k_0)}{\sqrt{4J^2 - (\omega_0 - \omega_c)^2}} + \frac{\delta(k + k_0)}{\sqrt{4J^2 - (\omega_0 - \omega_c)^2}} \right]. \tag{2.65}$$

In the thermodynamic limit $N \to \infty$, the summation becomes an integral that can be evaluated analytically, yielding

$$\rho(0, \omega_0) = \frac{1}{\pi} \frac{1}{\sqrt{4J^2 - (\omega_0 - \omega_c)^2}}. \tag{2.66}$$

Substituting this result into Eq. (2.33), we obtain the spontaneous emission rate

$$\Gamma_0 = \frac{2g^2}{\sqrt{4J^2 - (\omega_0 - \omega_c)^2}}. \tag{2.67}$$

The spontaneous emission dynamics are shown in Fig. 2.4. Panel (a) displays the exponential decay of the atomic population with the rate given by Eq. (2.67). Panel (b) shows the emitted photon density in real space. Since the emitter is located at the center of the array ($n = 0$), the photon propagates symmetrically along both directions of the lattice. This behavior is characteristic of Markovian spontaneous emission in an infinite translationally invariant photonic bath and serves as a reference for the finite-array case discussed in the next section.

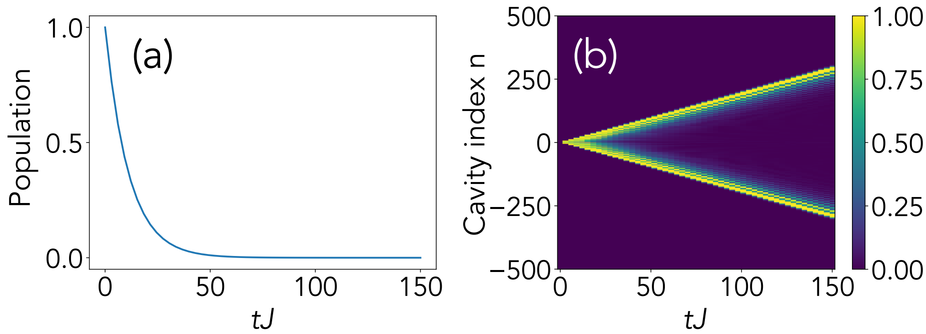

Figure 2.4: Spontaneous emission of an emitter coupled to an infinite cavity array. (a) Atomic population as a function of time. (b) Normalized Photon probability density in the lattice as a function of position and time.

2.6.2 Non-Markovian emission into a finite array

In the previous section, we considered the spontaneous emission of an atom coupled to an effectively infinite photonic lattice. In that limit, the emitted photon propagates away from the emitter without returning. In a finite lattice, however, the boundaries of the lattice play the role of mirrors. The emitted photon is reflected at the edges of the lattice and can later re-interact with the emitter. As a consequence, the atom experiences a delayed feedback from the photonic environment, giving rise to non-Markovian dynamics characterized by population revivals and memory effects.

This behavior is closely related to the discussion presented in Section 2.5 for an emitter coupled to a waveguide in the presence of mirrors. In the present case, the finite cavity array effectively behaves as a structured waveguide with reflecting boundaries. The propagation time of the emitted photon from the emitter to the array edges and back defines a characteristic delay time that determines the onset of non-Markovian effects.

To investigate this scenario, we consider a finite one-dimensional cavity array containing N cavities with open boundary conditions. The atom is coupled closer to the right edge of the lattice. Therefore, the photon that travels to the right edge travels a shorter path compared to the photon going to the left edge.

At short times, before the emitted photon reaches the boundaries, the atom cannot distinguish between a finite and an infinite lattice. Accordingly, the initial decay is approximately exponential with a rate close to that obtained in Eq. (2.67).

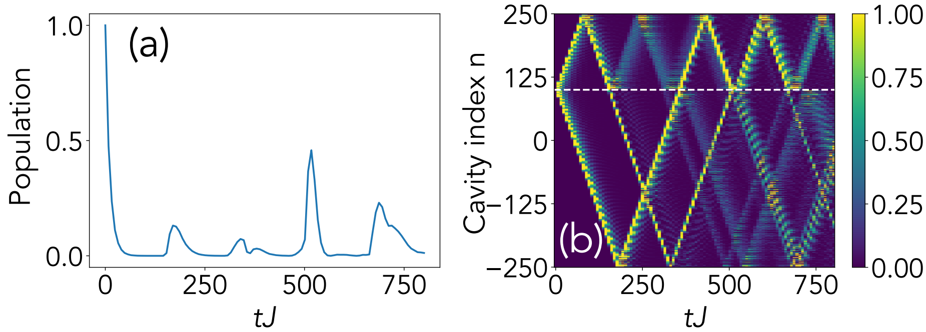

Figure 2.5: Spontaneous emission of an atom coupled to a finite cavity array. (a) Atomic population as a function of time. (b) Normalized photon density as a function of time. The dashed line shows the atomic position in the lattice.

Fig. 2.5(a) shows the atomic population dynamics in a finite cavity array. At early times, the population decays approximately exponentially, similarly to the infinite-array case. At later times, however, clear revivals emerge due to the back-reflection of the emitted photon from the lattice boundaries. These revivals are a direct signature of non-Markovian dynamics, since the evolution of the atom depends on its previous interaction history with the environment.

The photon density plotted in Fig. 2.5(b) provides a direct visualization of this mechanism. The photon wavepacket initially propagates away from the emitter along both directions of the lattice. Upon reaching the boundaries, the excitation is reflected back toward the atom, where it can be partially reabsorbed. This process repeats multiple times, leading to successive population revivals.

The following two sections are devoted to reviewing properties of bare photonic lattices (implemented via arrays of coupled cavities), in particular the effect of introducing a synthetic potential (Section 2.7) and lattices with topological properties (2.9). These two ingredients will provide the theoretical basis for the investigations carried out in Chapters 3 and 4, where we study how engineered synthetic potentials affect the emission dynamics of an emitter coupled to a one-dimensional photonic lattice in Chapter 3 and to a two-dimensional photonic lattice in Chapter 4.

2.7 Coupled-cavity array with a synthetic potential

In this section, we introduce the concept of the synthetic potential. To do so, let us consider a generic lattice in D dimensions, whose primitive vectors are $\{\mathbf{e}_1, \mathbf{e}_2, \cdots, \mathbf{e}_D\}$. An arbitrary lattice site is then labeled by

$$\mathbf{R} = \sum_{i=1}^{D} n_i \mathbf{e}_i, \qquad n_i \in \mathbb{Z}. \tag{2.68}$$

The Hamiltonian of such a lattice reads

$$H = \sum_{\mathbf{R}} \omega_a \, a_{\mathbf{R}}^\dagger a_{\mathbf{R}} + J \sum_{\langle \mathbf{R}, \mathbf{R}' \rangle} \left(a_{\mathbf{R}}^\dagger a_{\mathbf{R}'} + \mathrm{H.\,c.} \right), \tag{2.69}$$

where $a_{\mathbf{R}}$ ($a^\dagger_{\mathbf{R}}$) annihilates (creates) a photon in the cavity at site $\mathbf{R}$, ω_a is the bare cavity frequency, J is the nearest-neighbor hopping amplitude, and $\langle \mathbf{R}, \mathbf{R}' \rangle$ denotes a sum restricted to nearest-neighbor pairs. To introduce a synthetic potential, we promote the cavity frequency to a site-dependent quantity, $\omega_a \to \omega_a(\mathbf{R})$, which imprints a spatially varying energy landscape on the photons. For greater generality, we also define a unit vector $\hat{\mathbf{m}}$ that selects the direction along which the potential varies. The Hamiltonian of the lattice in the presence of a synthetic potential then takes the form

$$H = \sum_{\mathbf{R}} \omega_a(\mathbf{R}\cdot\hat{\mathbf{m}})\, a^\dagger_{\mathbf{R}} a_{\mathbf{R}} + J \sum_{\langle \mathbf{R},\mathbf{R}'\rangle} \left(a^\dagger_{\mathbf{R}} a_{\mathbf{R}'} + \mathrm{H.\,c.} \right). \tag{2.70}$$

As an example, let us consider a square lattice, with an linear synthetic potential, $\omega_a = v_0 \mathbf{R}\cdot\hat{\mathbf{m}}$, such that $\hat{\mathbf{m}}$ is along the x direction. We can see from Fig. 2.6 that the onsite potential changes linearly along the x direction but remains the same along the y direction.

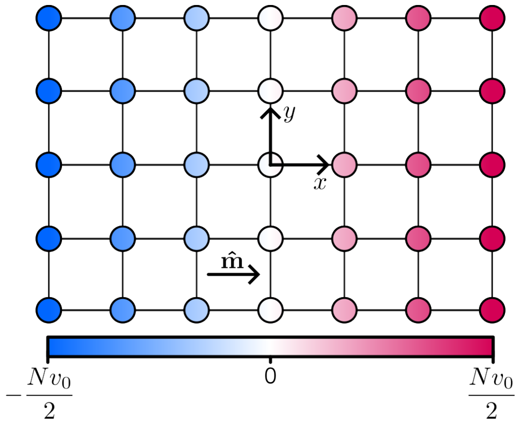

Figure 2.6: Square lattice with a linear synthetic potential. The unit vector $\hat{\mathbf{m}} = \hat{\mathbf{x}}$, gives the directionality of the potential gradient. As shown in this example, it varies along x and is constant along y.

This framework can be extended to a bipartite lattice composed of two sublattices, A and B, through the Hamiltonian

$$H = \sum_{\mathbf{R}} \left[\omega_a(\mathbf{R}\cdot\hat{\mathbf{m}})\, a^\dagger_{\mathbf{R}} a_{\mathbf{R}} + \omega_b(\mathbf{R}\cdot\hat{\mathbf{m}})\, b^\dagger_{\mathbf{R}} b_{\mathbf{R}} \right] + J \sum_{\langle \mathbf{R},\mathbf{R}'\rangle} \left(a^\dagger_{\mathbf{R}} b_{\mathbf{R}'} + \mathrm{H.\,c.} \right), \tag{2.71}$$

where $b_{\mathbf{R}}$ ($b^\dagger_{\mathbf{R}}$) annihilates (creates) a photon in a cavity on sublattice B at site $\mathbf{R}$, and $\omega_b(\mathbf{R}\cdot\hat{\mathbf{m}})$ encodes the synthetic potential profile on sublattice B. An instance of the application for the case of the bipartite lattice will be seen in Chapter 4.

2.7.1 One-dimensional coupled-cavity array with linear synthetic potential

An important and longstanding consequence of synthetic potentials in periodic systems is the emergence of Bloch oscillations. To introduce this phenomenon, we consider a one-dimensional coupled-cavity array with nearest-neighbor hopping, as discussed in previous sections, but now in the presence of a linear synthetic potential of the form $\omega_a = Fn$, where n labels the cavity position and F plays the role of an effective force.

We can see the sketch of the lattice in Fig. 2.7, where we represent the frequency of each cavity by the yellow bar, and we assume a positive value if the bar goes upwards and a negative value if the bar goes downward relative to the position of the lattice. This potential profile gives rise to a force pointing to the left.

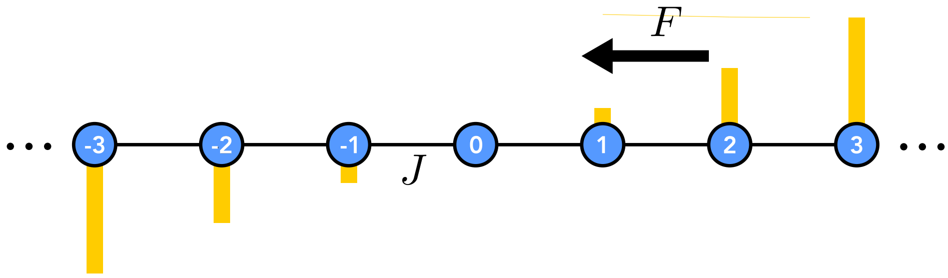

Figure 2.7: One-dimensional lattice with a linear synthetic potential. We assume that the cavity frequencies vary with the position following the expression $\omega_a = Fn$. The yellow bar depicts the potential variation, where the bar going down (up) represents negative (positive) values for the cavity frequency at that position.

Starting from the general equation Eq. (2.69), the Hamiltonian of this system reads

$$H = \sum_n Fn\, a_n^\dagger a_n - J \sum_n \left(a_{n+1}^\dagger a_n + \mathrm{H.\,c.} \right) , \tag{2.72}$$

where the first term accounts for the position-dependent cavity frequencies induced by the synthetic potential, while the second term describes photon hopping between neighboring cavities.

Field spectrum and eigenstates

The presence of the synthetic potential in Eq. (2.72) breaks the translational invariance of the lattice. As a consequence, Bloch's theorem no longer applies and momentum eigenstates cease to be stationary states of the system. Nevertheless, despite the absence of translational symmetry, both the energy spectrum and the stationary states of H can still be obtained analytically (see, e.g., Refs. [49–51]) as

$$\omega_n = nF\,, \tag{2.73}$$

$$|\varphi_n\rangle = \sum_m J_{m-n}(\xi)\,|m\rangle \ , \tag{2.74}$$

with $H\,|\varphi_n\rangle = \omega_n\,|\varphi_n\rangle$, where n runs over all integers. Here, $J_\alpha(x)$ denotes the Bessel function of the first kind of order α and argument x, while

$$\xi = \frac{2J}{F} \tag{2.75}$$

defines a characteristic length scale which, from now on, will be referred to as the *localization length*. Throughout this section, we assume an infinitely long cavity array, which is appropriate since our goal in this thesis is to study qubit emission in the bulk of the lattice.

Each eigenstate (2.74) can also be formally generated by applying a suitable displacement operator to the localized cavity state $|n\rangle$. Such an operator can be defined in terms of extended Susskind–Glogower (SG) operators (see, e.g., Refs. [52, 53]), which in the present context coincide with the discrete translation operator and its inverse. According to Eq. (2.73), and as illustrated in Fig. 2.8(b), the field spectrum becomes

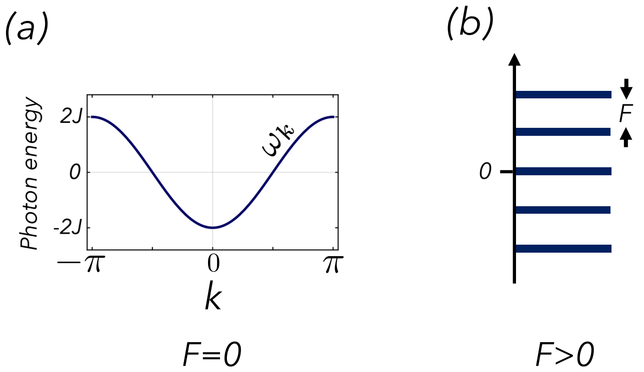

Figure 2.8: Single-photon energy spectrum of the cavity array for (a) $F = 0$, the system simplifies to the one studied in Section 2.6, corresponding to a continuous finite band. (c) $F > 0$, the spectrum becomes discrete, forming the so-called Wannier–Stark ladder with energy spacing F.

discrete for any finite $F > 0$, forming a ladder structure known as the *Wannier–Stark ladder*. Adjacent energy levels are equally spaced by the force, namely $\omega_{n+1} - \omega_n = F$. In contrast to the translationally invariant case discussed previously, where eigenstates are extended Bloch waves [see Eq. (2.61)], the eigenstates $|\varphi_n\rangle$ are now spatially localized around the nth cavity, with characteristic width set by the localization length ξ [cf. Eq. (2.75)]. This motivates the notation used for the eigenstates, whose label intentionally coincides with the cavity index.

Fig. 2.9 shows the spatial profile of the eigenstates for the representative cases $n = -10$ and $n = 10$, considering both a large and a small localization length [panels (a) and (b), respectively]. All eigenstates share the same functional form, differing only by a spatial displacement determined by n. Furthermore, for $|m - n| \gtrsim \xi$, the wavefunction decays exponentially with the distance from its center.

It is worth noting that the spectrum (2.73) coincides with the one obtained in the limit of vanishing hopping, $J = 0$, where the cavities become fully decoupled and the eigenstates reduce trivially to $|\varphi_n\rangle = |n\rangle$. Indeed, in this limit one has $\xi = 0$ [cf. Eq. (2.75)]. Equations (2.73) and (2.74) therefore show that photon hopping does not modify the equally spaced energy spectrum, but instead affects the spatial structure of the eigenstates by delocalizing them over multiple cavities.

An important feature that will be relevant in Section 3.3.3 is the oscillatory structure of the wavefunctions for sufficiently large ξ [see Fig. 2.9(a)]. In the vicinity of cavity n, namely near the center of the wavefunction support, the amplitude $\langle m\,|\varphi_n\rangle$ exhibits an approximately sinusoidal behaviour. More precisely, in the regime $|n - m| \ll \sqrt{\xi}$ one can use the asymptotic expansion

$$J_{m-n}(\xi) = \sqrt{\frac{2}{\pi\xi}}\,\sin\left[(n-m)\frac{\pi}{2} + \xi + \frac{\pi}{4}\right], \tag{2.76}$$

which corresponds to the standard asymptotic form of Bessel functions [54].

Finally, we point out that when $\xi \gtrsim 1$, which corresponds to sufficiently weak forces,

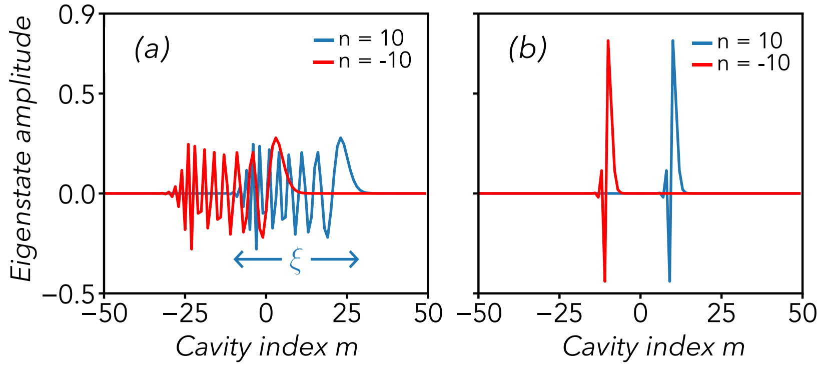

Figure 2.9: Wavefunctions of the field eigenstates $|\varphi_n\rangle$. We show the representative cases $n = -10$ and $n = 10$ for $\xi = 15$ (a) and $\xi = 1$ (b). Each wavefunction $\langle m\,|\varphi_n\rangle$ is localized around cavity n with characteristic localization length ξ. Near its center, the wavefunction displays spatial oscillations before eventually decaying exponentially for $|m - n| \gtrsim \xi$. For sufficiently large ξ, as in panel (a), the eigenstates become highly delocalized and strongly overlap with one another.

neighboring eigenstates strongly overlap with one another. This overlap increases progressively as the localization length becomes larger.

Bloch oscillations

Having characterized the stationary eigenstates of the lattice in the presence of the synthetic force, we now turn to the corresponding dynamical behaviour. One of the most remarkable consequences of the Wannier–Stark spectrum is the emergence of Bloch oscillations.

Since the force F breaks translational invariance, the plane waves (2.61) are no longer stationary states of the Hamiltonian. Nevertheless, their time evolution remains particularly simple. In fact, it can be shown that

$$e^{-iH_B t}\,|k\rangle \propto |k(t)\rangle \;, \tag{2.77}$$

where the quasi-momentum satisfies the semiclassical equation of motion

$$\frac{dk}{dt} = -F\,. \tag{2.78}$$

Therefore, if the initial quasi-momentum at time t_i is k_i, its subsequent evolution is given by

$$k(t) = k_i - F(t - t_i)\,. \tag{2.79}$$

Equation (2.79) is formally analogous to Newton's second law for a classical particle subjected to a constant force. In the present lattice system, however, the quasi-momentum is restricted to the first Brillouin zone (FBZ), $-\pi < k \leq \pi$, and therefore cannot increase indefinitely. As a consequence, once $k(t)$ reaches the left boundary of the FBZ, namely $k(t) = -\pi$, it reappears at the right boundary and continues its linear evolution until it reaches the left boundary again (see Fig. 2.10). The resulting dynamics is periodic and gives rise to the celebrated phenomenon of Bloch oscillations

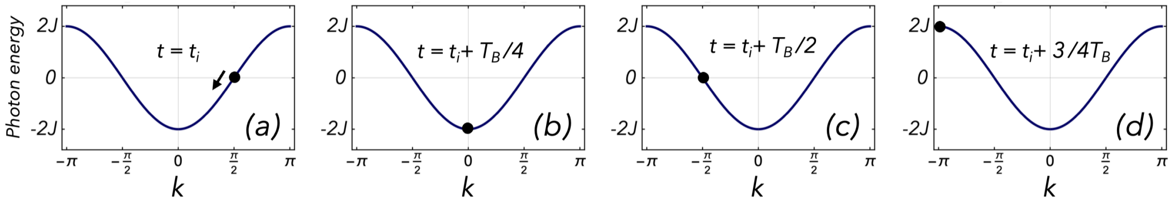

Figure 2.10: Sketch of the time evolution of the quasi-momentum in the presence of a force pointing to the left, illustrating Bloch oscillations in momentum space. We consider the initial condition $k(t_i) = k_i = \pi/2$ [panel (a)]. Panels (b), (c), and (d) show the evolved momentum at times $t = t_i + T_B/4$, $t = t_i + T_B/2$, and $t = t_i + 3T_B/4$, respectively, where T_B is the Bloch oscillation period [cf. Eq. (2.80)]. At time $t = t_i + T_B$ (not shown), the photon momentum returns to its initial value. Note that the photon velocity $v(t) = d\omega_k/dk$ vanishes whenever $k(t) = 0, \pm\pi$, corresponding to the band edges where the slope of ω_k is zero. At these points the photon reverses its direction of motion. In the example shown here, the first reversal occurs at time $t = t_i + T_B/4$, when the photon reaches the lower band edge.

[55, 56], whose period follows directly from Eq. (2.79):

$$T_B = \frac{2\pi}{F}\,. \tag{2.80}$$

Unlike a free massive particle undergoing unbounded uniformly accelerated motion, here the periodicity of the lattice causes the photon to perform a bounded oscillatory motion in real space. This behaviour originates from the periodic dispersion relation [see Eq. (2.60) and Fig. Fig. 2.8(a)], which leads to a time-dependent acceleration

$$a(t) = \left(\frac{d^2\omega_k}{dk^2}\right) F\,. \tag{2.81}$$

In particular, the photon group velocity $v(t) = d\omega_k/dk$ vanishes at the band edges $k(t) = 0, \pm\pi$, where the slope of the dispersion relation is zero. At these points, the photon reverses its direction of motion in real space.

To make this more explicit, we substitute (2.79) into the group velocity

$$v_k = \frac{d\omega_k}{dk} = 2J \sin k \tag{2.82}$$

[cf. Eq. (2.60)], obtaining the time-dependent velocity

$$v(t) = 2J \sin[k_i - F(t - t_i)]\,. \tag{2.83}$$

Integrating this expression and using $F = 2\pi/T_B$, we find that the photon undergoes a real-space oscillatory motion with period T_B described by

$$x(t) = x_i - \xi \cos k_i + \xi \cos\left(k_i - 2\pi\,\frac{t - t_i}{T_B}\right)\,, \tag{2.84}$$

where $x_i = x(t_i)$. Remarkably, the oscillation amplitude is precisely given by the localization length ξ [cf. Eq. (2.75)], thus establishing a direct connection between the spatial structure of the Wannier–Stark eigenstates and the dynamical Bloch oscillations.

Finally, these real-space oscillations are in phase with the evolution of the photon energy,

$$\omega(t) = -2J\cos\left(k_i - 2\pi\,\frac{t-t_i}{T_B}\right), \tag{2.85}$$

which implies that whenever the photon returns to its initial position x_i, its energy also recovers the initial value $\omega(t_i) = -2J\cos k_i$.

2.8 Giant atoms

In Section 2.1.2, we introduced atomic emitters as point-like two-level systems coupled to a lattice at a single site, as justified by the dipole approximation. Here we consider a different class of emitters, known as *giant atoms*, which couple to a structured bath at multiple spatially separated points, giving rise to intrinsically non-local light–matter interactions. Because the coupling occurs at several points, interference between them can be exploited to control the emitted field, for instance, to make the emission directional.

This type of emitter was first realized experimentally in the context of surface acoustic waves (SAWs) [57]. Since then, giant atoms have attracted considerable attention due to several remarkable phenomena, including frequency-dependent couplings [58] and decoherence-free interactions [30]. An instance of a giant artificial atom coupled to a set of resonators is depicted in Fig. 1.1(c) and (d).

To gain insight into their behavior, we follow an approach similar to that introduced in Section 2.6. We consider a one-dimensional chain of coupled cavities and couple a giant atom to several sites along the chain.

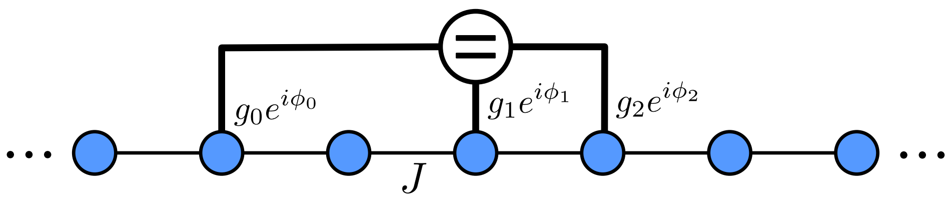

Figure 2.11: Giant atom coupled to a one-dimensional coupled-cavity array. The emitter interacts with several distinct cavities (coupling points), with coupling strengths g_ℓ and phases ϕ_ℓ.

The Hamiltonian reads

$$H = \omega_0\sigma_+\sigma_- + \sum_n \omega_c a_n^\dagger a_n - J\sum_n\left(a_{n+1}^\dagger a_n + \mathrm{H.\,c.}\right) + H_{\mathrm{int}}, \tag{2.86}$$

where the interaction Hamiltonian is given by

$$H_{\mathrm{int}} = \sum_{\ell=1}^{\mathcal{N}}\left(g_\ell e^{i\phi_\ell}\sigma_- a_\ell^\dagger + \mathrm{H.\,c.}\right). \tag{2.87}$$

Here, g_ℓ is the coupling strength at the ℓ-th connection point (or "leg"), ϕ_ℓ is the associated phase, and $\mathcal{N}$ is the total number of coupling points. After transforming the photonic operators into momentum space, the Hamiltonian becomes

$$H = \omega_0 \sigma_+ \sigma_- + \sum_k \omega(k) a_k^\dagger a_k + \sum_k g(k) \left(\sigma_- a_k^\dagger + \text{H. c.} \right), \tag{2.88}$$

where the momentum-dependent coupling function is

$$g(k) = \frac{1}{\sqrt{N}} \sum_\ell g_\ell e^{i(\phi_\ell - k\ell)}. \tag{2.89}$$

The function $g(k)$ represents the effective coupling between the emitter and the bath mode with momentum k. Due to interference between the different coupling points, the coupling becomes momentum dependent.

2.8.1 Giant-atom-enabled chiral emission

As a simple illustrative example, let us consider a giant atom coupled to two sites, $\ell = 0$ and $\ell = 1$. Assuming equal coupling strengths $g_0 = g_1 = g$ and defining the phase difference $\varphi = \phi_1 - \phi_0$, the coupling function becomes

$$g(k) \propto 1 + e^{i(\varphi - k)}. \tag{2.90}$$

The two coupling points contribute coherently to the interaction with each bath mode, as a result, destructive interference can suppress the coupling to selected momenta.

Now, setting the emitter resonant with the center of the band, $\omega_0 = 0$, the resonance condition $\omega(k) = \omega_0$ selects two resonant modes with momenta $k_0 = \pm\pi/2$. Evaluating the coupling function at these points, we find

$$g(k_0) = 0, \quad g(-k_0) \neq 0 \quad \text{for } \varphi = -\frac{\pi}{2}, \tag{2.91}$$

$$g(-k_0) = 0, \quad g(k_0) \neq 0 \quad \text{for } \varphi = \frac{\pi}{2}. \tag{2.92}$$

Thus, by tuning the relative phase φ, the emitter can be made to decouple from one of the propagating modes. Consequently, the emitter radiates only into one propagation direction, giving rise to *chiral emission*. Therefore, giant atoms provide a mechanism to engineer directional light–matter interactions through interference between spatially separated coupling points.

To quantify how the giant atom modifies spontaneous emission, it is useful to introduce an effective local density of states,

$$\tilde{\rho}(\chi, \omega) = \sum_k |\langle \chi | k \rangle|^2 \delta\left(\omega - \omega_k\right), \tag{2.93}$$

where the state $|\chi\rangle = e^{i\phi_0} |0\rangle + e^{i\phi_1} |1\rangle$ [32], represents the spatial profile of the giant-atom coupling. Proceeding as in Section 2.6.1 and taking the thermodynamic limit, we obtain

$$\tilde{\rho}(\chi, \omega_0) = \frac{1}{\pi} \left(2 - \frac{\omega_0}{J} \cos\varphi \right) \frac{1}{\sqrt{4J^2 - (\omega_0 - \omega_c)^2}}. \tag{2.94}$$

The decay rate can then be written in terms of the local density of states as follows,

$$\Gamma = 2\pi\tilde{g}^2\tilde{\rho}(\chi, \omega_0), \tag{2.95}$$

where

$$\tilde{g} = \sqrt{\sum_{\ell} |g_\ell|^2}. \tag{2.96}$$

Therefore,

$$\Gamma = \frac{2g^2}{\sqrt{4J^2 - (\omega_0 - \omega_c)^2}} \left(2 - \frac{\omega_0}{J}\cos\varphi\right). \tag{2.97}$$

Notice that Γ_0 coincides with the spontaneous emission rate of a point-like atom [Eq. (2.67)]. The giant atom modifies this rate through the interference factor,

$$\Gamma = \Gamma_0 \left(2 - \frac{\omega_0}{J}\cos\varphi\right), \qquad \text{where} \qquad \Gamma_0 = \frac{2g^2}{\sqrt{4J^2 - (\omega_0 - \omega_c)^2}}. \tag{2.98}$$

Fig. 2.12(a) shows the exponential decay of the atomic population, in agreement with the analytical decay rate predicted by Eq. (2.98). In Fig. 2.12(b), we plot the normalized photon probability density for $\varphi = \pi/2$. Due to destructive interference between the two coupling points, emission into one propagation direction is suppressed, leading to unidirectional photon emission.

Conversely, in Fig. 2.12(c), choosing $\varphi = -\pi/2$ reverses the preferred propagation direction. This directional selectivity enabled by giant atoms will be further explored in Chapter 4 in a two-dimensional context.

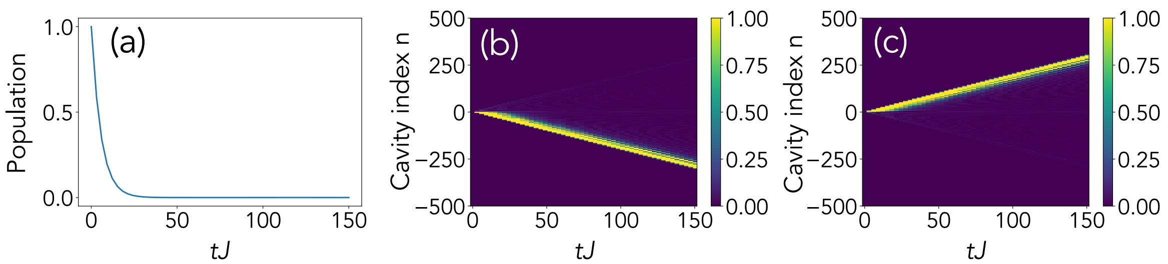

Figure 2.12: Spontaneous emission of a giant atom coupled to a coupled-cavity array. (a) Atomic excited-state population as a function of time. (b) Normalized photon probability density for $\varphi = \pi/2$, showing directional emission. (c) Same as in (b), but for $\varphi = -\pi/2$, where the propagation direction is reversed.

2.9 Topological photonic lattices

Photonic lattices are not only useful because they provide structured photonic reservoirs with engineered dispersion relations. In two dimensions, they can also host photonic bands with non-trivial geometrical and topological properties. This means that the properties of a photon propagating in the lattice are not determined only by the band frequency $\omega_n(\mathbf{k})$, but also by the structure of the corresponding Bloch eigenmode as a function of the quasi-momentum $\mathbf{k}$.

Let us consider a two-dimensional lattice whose unit cells are labeled by

$$\mathbf{R} = n_1\mathbf{e}_1 + n_2\mathbf{e}_2, \qquad n_1, n_2 \in \mathbb{Z}, \tag{2.99}$$

where $\mathbf{e}_1$ and $\mathbf{e}_2$ are primitive lattice vectors. A generic tight-binding photonic Hamiltonian can be written as

$$H_B = \sum_{\mathbf{R},\mu} \omega_\mu a^\dagger_{\mathbf{R},\mu} a_{\mathbf{R},\mu} + \sum_{\mathbf{R},\mathbf{R}'} \sum_{\mu,\nu} \left(J_{\mu\nu}(\mathbf{R}-\mathbf{R}') a^\dagger_{\mathbf{R},\mu} a_{\mathbf{R}',\nu} + \text{H.c.} \right), \tag{2.100}$$

where $a_{\mathbf{R},\mu}$ annihilates a photon in the internal mode μ of the unit cell $\mathbf{R}$. The index μ can label different resonators in the unit cell, different polarizations, orbitals, or synthetic degrees of freedom. Such internal structure is essential for obtaining nontrivial band topology, since a single isolated mode per unit cell usually gives only a scalar Bloch Hamiltonian.

For a translationally invariant lattice, we introduce the momentum-space operators

$$a_{\mathbf{k},\mu} = \frac{1}{\sqrt{N}} \sum_{\mathbf{R}} e^{-i\mathbf{k}\cdot\mathbf{R}} a_{\mathbf{R},\mu}, \tag{2.101}$$

where N is the number of unit cells and $\mathbf{k}$ belongs to the first Brillouin zone. Therefore, we can define a matrix $h(\mathbf{k})$ such that its elements reads,

$$[h(\mathbf{k})]_{\mu\nu} = \omega_\mu \delta_{\mu\nu} + \sum_{\mathbf{d}} \left[J_{\mu\nu}(\mathbf{d}) e^{-i\mathbf{k}\cdot\mathbf{d}} + J^*_{\mu\nu}(\mathbf{d}) e^{i\mathbf{k}\cdot\mathbf{d}} \right], \tag{2.102}$$

such that $\mathbf{d} = \mathbf{R} - \mathbf{R}'$. The Hamiltonian then takes the Bloch form

$$H_B = \sum_{\mathbf{k}} \mathbf{a}^\dagger_{\mathbf{k}} h(\mathbf{k}) \mathbf{a}_{\mathbf{k}}, \tag{2.103}$$

where $\mathbf{a}_{\mathbf{k}}$ is a column vector collecting the annihilation operators of the internal modes in the unit cell. The normal modes are obtained from the eigenvalue problem

$$h(\mathbf{k}) \left| u_{n\mathbf{k}} \right\rangle = \omega_n(\mathbf{k}) \left| u_{n\mathbf{k}} \right\rangle, \tag{2.104}$$

where n labels the photonic band, $\omega_n(\mathbf{k})$ is the band dispersion, and $|u_{n\mathbf{k}}\rangle$ is the periodic part of the Bloch eigenmode.

The central geometrical object associated with an isolated band is the Berry connection [59, 60],

$$\mathbf{A}_n(\mathbf{k}) = i \left\langle u_{n\mathbf{k}} \right| \nabla_{\mathbf{k}} \left| u_{n\mathbf{k}} \right\rangle. \tag{2.105}$$

This quantity plays the role of a gauge potential in momentum space. Under a local gauge transformation, each Bloch state transforms as,

$$\left| u_{n\mathbf{k}} \right\rangle \to e^{i\chi_n(\mathbf{k})} \left| u_{n\mathbf{k}} \right\rangle, \tag{2.106}$$

under which

$$\mathbf{A}_n(\mathbf{k}) \to \mathbf{A}_n(\mathbf{k}) - \nabla_{\mathbf{k}} \chi_n(\mathbf{k}). \tag{2.107}$$

Thus, the Berry connection itself is not gauge invariant. The associated gauge-invariant quantity is the Berry curvature,

$$\Omega_n(\mathbf{k}) = [\nabla_{\mathbf{k}} \times \mathbf{A}_n(\mathbf{k})]_z \,. \tag{2.108}$$

Equivalently, in two dimensions it can be written as

$$\Omega_n(\mathbf{k}) = i \left(\langle \partial_{k_x} u_{n\mathbf{k}} | \partial_{k_y} u_{n\mathbf{k}} \rangle - \langle \partial_{k_y} u_{n\mathbf{k}} | \partial_{k_x} u_{n\mathbf{k}} \rangle \right) . \tag{2.109}$$

The Berry curvature measures how the Bloch eigenmode twists as $\mathbf{k}$ is varied across the Brillouin zone. It is therefore a property of the eigenvectors of the Bloch Hamiltonian. In this sense, two bands with similar dispersion relations can nevertheless have very different geometrical and topological properties.

The global topological invariant of an isolated two-dimensional band is the Chern number,

$$C_n = \frac{1}{2\pi} \int_{\mathrm{BZ}} d^2\mathbf{k}\, \Omega_n(\mathbf{k}). \tag{2.110}$$

The integral is taken over the whole first Brillouin zone. Since the Brillouin zone is a closed two-dimensional manifold, the Chern number is an integer. Importantly, this integer cannot change under a smooth deformation of the Hamiltonian, as long as the band remains separated from all other bands by a finite gap. A change of C_n is therefore possible only if the bulk gap closes and reopens.

This provides a useful physical interpretation of topological phase transitions. If a control parameter of the lattice is varied, the topology of a band can change only at points where two bands touch. At such points the Berry curvature can be strongly concentrated, and after the gap reopens the integral in Eq. (2.110) may differ by an integer. Thus, band topology is tied to the way in which gaps open and close in momentum space.

A particularly transparent description is obtained for a generic two-band model, whose Bloch Hamiltonian can be written as

$$h(\mathbf{k}) = d_0(\mathbf{k})\mathbb{I} + \mathbf{d}(\mathbf{k}) \cdot \boldsymbol{\sigma}, \tag{2.111}$$

where $\boldsymbol{\sigma} = (\sigma_x, \sigma_y, \sigma_z)$ are Pauli matrices acting on the internal two-dimensional space of the unit cell. The corresponding bands are

$$\omega_\pm(\mathbf{k}) = d_0(\mathbf{k}) \pm |\mathbf{d}(\mathbf{k})|. \tag{2.112}$$

The gap between the two bands is therefore

$$\Delta\omega(\mathbf{k}) = 2|\mathbf{d}(\mathbf{k})|. \tag{2.113}$$

A topological phase transition can occur only when

$$\mathbf{d}(\mathbf{k}_0) = 0 \tag{2.114}$$

for some momentum $\mathbf{k}_0$, since this is the condition for the two bands to touch.

In such two-band systems, the Berry curvature of the upper and lower bands can be expressed directly in terms of the unit vector [60]

$$\hat{\mathbf{d}}(\mathbf{k}) = \frac{\mathbf{d}(\mathbf{k})}{|\mathbf{d}(\mathbf{k})|}. \tag{2.115}$$

One finds

$$\Omega_{\pm}(\mathbf{k}) = \mp\frac{1}{2}\hat{\mathbf{d}}(\mathbf{k}) \cdot \left(\partial_{k_x}\hat{\mathbf{d}}(\mathbf{k}) \times \partial_{k_y}\hat{\mathbf{d}}(\mathbf{k})\right). \tag{2.116}$$

The Chern number therefore counts how many times the vector $\hat{\mathbf{d}}(\mathbf{k})$ wraps around the Bloch sphere as $\mathbf{k}$ spans the Brillouin zone. This gives a geometrical meaning to the topological invariant: a topologically trivial band corresponds to a map that can be continuously contracted, whereas a topological band corresponds to a map with non-zero winding.

For photonic systems, non-zero Chern numbers are especially important because they imply the existence of robust boundary channels. These are the topological edge modes, which propagate along the boundary of a finite lattice or along an interface between two regions with different topological invariants. Their existence is a manifestation of the bulk-boundary correspondence: a difference in bulk topology across an interface must be compensated by gapless modes localized at the interface.

2.9.1 Topological edge modes

The emergence of edge modes can be understood from a simple continuum argument based on the closing and reopening of a bulk gap [60]. Consider a two-dimensional topological photonic lattice described, near a gap-closing point, by an effective two-band Hamiltonian of the form

$$h_{\text{eff}}(\mathbf{q}) = vq_x\sigma_x + vq_y\sigma_y + m\sigma_z. \tag{2.117}$$

Here $\mathbf{q} = (q_x, q_y)$ is the momentum measured from the gap-closing point, v is an effective velocity, and m is a mass term controlling the size and sign of the gap. The spectrum is

$$\omega_{\pm}(\mathbf{q}) = \pm\sqrt{v^2q_x^2 + v^2q_y^2 + m^2}, \tag{2.118}$$

so that the bulk gap is $2|m|$. The gap closes when $m = 0$ and reopens when m changes sign. In many two-dimensional topological models, the two signs of m correspond to two phases with different Chern numbers.

We now consider an interface between two domains characterized by opposite signs of the mass. For concreteness, we take the mass to depend on the x coordinate,

$$m = m(x), \qquad \lim_{x\to-\infty} m(x) < 0, \qquad \lim_{x\to+\infty} m(x) > 0. \tag{2.119}$$

The interface is located near $x = 0$, where the mass changes sign. We therefore replace

$$q_x \to -i\partial_x, \qquad q_y \to k_y, \tag{2.120}$$

and obtain the effective Hamiltonian

$$h_{\text{edge}}(k_y) = -iv\sigma_x\partial_x + vk_y\sigma_y + m(x)\sigma_z. \tag{2.121}$$

Let us first look for a localized solution at $k_y = 0$ and zero frequency, namely

$$h_{\text{edge}}(0)\psi(x) = 0. \tag{2.122}$$

This gives

$$\left[-iv\sigma_x\partial_x + m(x)\sigma_z\right]\psi(x) = 0. \tag{2.123}$$

Multiplying by σ_x and using $\sigma_x\sigma_z = -i\sigma_y$, we obtain

$$\left[v\partial_x + m(x)\sigma_y\right]\psi(x) = 0. \tag{2.124}$$

We can choose $\psi(x)$ to be an eigenstate of σ_y,

$$\sigma_y\chi_s = s\chi_s, \qquad s = \pm 1, \tag{2.125}$$

and write

$$\psi_s(x) = f_s(x)\chi_s. \tag{2.126}$$

The envelope function then satisfies

$$\partial_x f_s(x) = -s\frac{m(x)}{v} f_s(x), \tag{2.127}$$

with solution

$$f_s(x) = \mathcal{N} \exp\left[-s\frac{1}{v}\int_0^x m(x')\,dx'\right]. \tag{2.128}$$

Only one choice of s gives a normalizable state localized near the interface. For the mass profile in Eq. (2.119), this is the value of s such that the exponent is negative for both $x \to +\infty$ and $x \to -\infty$. Thus, the change of sign of the mass produces a bound photonic mode localized at the domain wall.

The dispersion of this bound state is obtained by restoring the term $vk_y\sigma_y$ in Eq. (2.121). Since the bound state is an eigenstate of σ_y, one immediately finds

$$\omega_{\text{edge}}(k_y) = svk_y. \tag{2.129}$$

The edge mode is therefore gapless and propagates along the interface with group velocity

$$v_{\text{edge}} = \frac{\partial\omega_{\text{edge}}}{\partial k_y} = sv. \tag{2.130}$$

Its propagation direction is fixed by the sign of the mass gradient, or equivalently by which topological phase lies on each side of the interface.

This derivation shows explicitly how the existence of edge modes follows from the bulk gap closing and reopening. In the bulk, a nonzero mass m opens a gap. Across the interface, the mass changes sign, meaning that the system must locally pass through the gap-closing point $m = 0$. The resulting bound state is the remnant of this gap closing in an inhomogeneous geometry. In a full lattice model, the number of such edge modes is fixed by the difference between the Chern numbers of the two domains,

$$N_{\text{edge}} = C_{\text{left}} - C_{\text{right}}, \tag{2.131}$$

up to the sign convention that fixes the propagation direction.

From the point of view of waveguide QED, a topological edge mode acts as a one-dimensional photonic channel embedded in a two-dimensional lattice. A quantum emitter whose frequency lies inside the bulk band gap cannot efficiently decay into bulk modes, since these are off-resonant. If the emitter is placed near the boundary or near a topological interface, it can instead emit into the edge channel. When only one propagation direction is available at the relevant frequency, the resulting spontaneous emission is chiral. This provides a route to directional light–matter interaction in which the propagation properties of the emitted photon are protected by the topology of the photonic bath.

2.9.2 The honeycomb lattice

In this section, we review the topological features of the honeycomb lattice. This photonic lattice plays a central role in Chapter 4, where we study it under a synthetic potential. Here, however, we consider a simpler version to introduce its topology where the lattice consists of two sublattices, a and b featuring a staggered cavity frequency Δ [see Fig. 4.1].

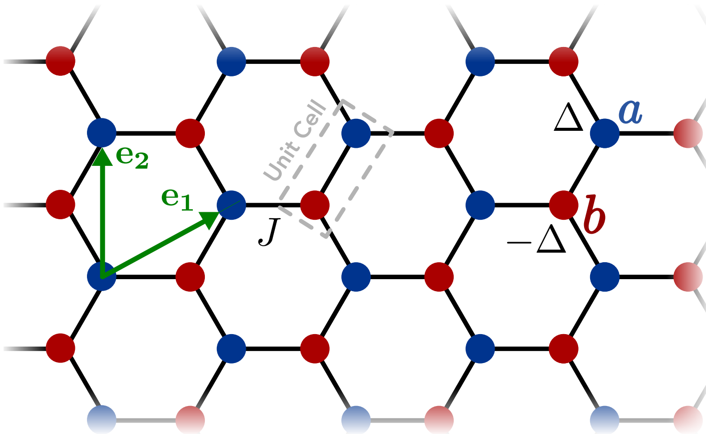

Figure 2.13: The Honeycomb lattice. This lattice unit cell features two sites a and b each one having the the frequency $\omega_a = \Delta$ and $\omega_b = -\Delta$ respectively. The bare lattice does not break time reversal symmetry, it breaks inversion symmetry due to sublattice detuning measured by Δ.

The Hamiltonian can be written as a special case of Eq. (2.71),

$$H_B = \Delta \sum_{\mathbf{R}} (a^\dagger_{\mathbf{R}} a_{\mathbf{R}} - b^\dagger_{\mathbf{R}} b_{\mathbf{R}}) + J \sum_{\langle \mathbf{R},\mathbf{R}' \rangle} (a^\dagger_{\mathbf{R}} b_{\mathbf{R}'} + \mathrm{H.\,c.})\,. \tag{2.132}$$

Here, $\mathbf{R} = n\mathbf{e}_1 + m\mathbf{e}_2$ labels the unit cells, $n = -N_1/2, \ldots, N_1/2 - 1$ and $m = -N_y/2, \ldots, N_y/2 - 1$, where

$$\mathbf{e}_1 = \left(\frac{3a}{2}, \frac{\sqrt{3}a}{2} \right), \quad \mathbf{e}_2 = \left(0, \sqrt{3}a \right) \tag{2.133}$$

are the primitive vectors, and a is the nearest-neighbor distance [17]. In the second sum, $\langle \mathbf{R}, \mathbf{R}' \rangle$ means that the sum runs over nearest-neighbor sites, while $a_{\mathbf{R}} \equiv a_{nm}$ and

[17]The notation distinguishes between N_1, the number of unit cells along the $\mathbf{e}_1$ direction, and N_y,

$b_{\mathbf{R}} \equiv b_{nm}$ are standard bosonic ladder operators. In Eq. (2.132), the parameter Δ is the *sublattice detuning*, since 2Δ is the difference between the bare frequencies of the a- and b-sites associated with the two sublattices, while J denotes the photon hopping rate [see Fig. 4.1]. For $\Delta = 0$, Eq. (2.132) is the bosonic analog of the tight-binding Hamiltonian of pristine graphene. Importantly, a nonzero detuning Δ breaks inversion symmetry in the lattice. We point out that, for any values of J and Δ, the free field Hamiltonian (2.132) does not break time-reversal symmetry.

2.9.3 Spectrum and normal modes of H_B

Under periodic boundary conditions, the lattice bare Hamiltonian H_B enjoys discrete translational invariance with respect to the Bravais lattice $\mathbf{R}$. Accordingly, it is convenient to introduce the momentum ladder operators as

$$a_{\mathbf{k}} = \frac{1}{\sqrt{N}} \sum_{\mathbf{R}} e^{-i\mathbf{k}\cdot\mathbf{R}} a_{\mathbf{R}}\,, \qquad b_{\mathbf{k}} = \frac{1}{\sqrt{N}} \sum_{\mathbf{R}} e^{-i\mathbf{k}\cdot\mathbf{R}} b_{\mathbf{R}}\,, \tag{2.134}$$

where $N = N_1 N_y$ is the number of unit cells and $\mathbf{k}$ runs over the first Brillouin zone. This has hexagonal shape [see Fig. 2.14(a)] with vertices K and K' (Dirac points) of coordinates

$$\mathbf{K} = -\mathbf{K}' = \left(\frac{2\pi}{3a}, -\frac{2\pi}{3\sqrt{3}\,a}\right). \tag{2.135}$$

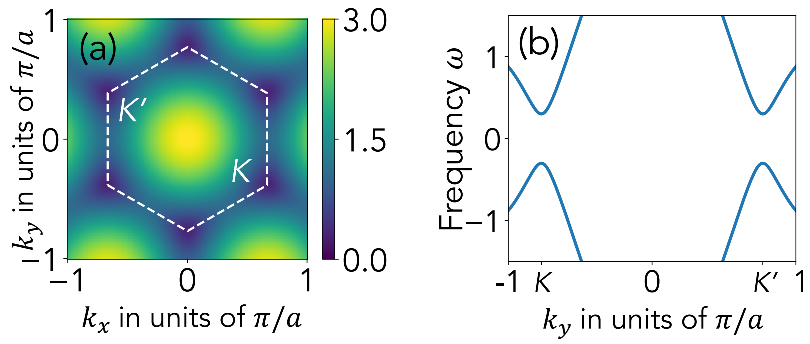

Figure 2.14: Bare lattice spectrum. (a) Density plot of $\omega_{\mathbf{k}}$ [cf. Eqs. (2.139) and (2.140)]. The dashed line marks the boundary of the first Brillouin zone, whose two inequivalent vertices are the Dirac points K and K' (each of the four remaining vertices of the hexagon is equivalent to either K or K'). (b) Band dispersion along the k_y direction for $k_x = 0$, restricted to frequencies $|\omega| \leq 5\Delta$ to highlight the dispersion near the K and K' valleys. In both panels, we set $\Delta = 0.3J$ and frequencies are expressed in units of J.

Upon inversion of (2.134), Hamiltonian (2.132) can be arranged in the block-diagonal form (see e.g. Refs. [61, 62])

$$H_B = \sum_{\mathbf{k}} \begin{pmatrix} a_{\mathbf{k}}^\dagger & b_{\mathbf{k}}^\dagger \end{pmatrix} h(\mathbf{k}) \begin{pmatrix} a_{\mathbf{k}} \\ b_{\mathbf{k}} \end{pmatrix}, \tag{2.136}$$

the number of unit cells along the $\mathbf{e}_2$ direction. This choice is convenient because $\mathbf{e}_2$ is aligned with the y axis.

where the 2×2 Block Hamiltonian is defined as

$$h(\mathbf{k}) = \begin{pmatrix} \Delta & Jf(\mathbf{k}) \\ Jf^*(\mathbf{k}) & -\Delta \end{pmatrix} \tag{2.137}$$

with

$$f(\mathbf{k}){=}e^{ik_xa}{+}2e^{-ik_xa/2}\cos\left(\frac{\sqrt{3}}{2}ak_y\right). \tag{2.138}$$

Through diagonalization of $h(\mathbf{k})$, Hamiltonian H_B can be eventually expressed in the diagonal form

$$H_B = \sum_{\mathbf{k}} \omega_{\mathbf{k}} \left(\alpha^\dagger_{\mathbf{k}} \alpha_{\mathbf{k}} - \beta^\dagger_{\mathbf{k}} \beta_{\mathbf{k}} \right) \tag{2.139}$$

with

$$\omega_{\mathbf{k}} = \sqrt{\Delta^2 + J^2 |f(\mathbf{k})|^2}\,, \tag{2.140}$$

and

$$\alpha_{\mathbf{k}} = \cos\frac{\theta_{\mathbf{k}}}{2}\, a_{\mathbf{k}} + e^{-i\varphi_{\mathbf{k}}} \sin\frac{\theta_{\mathbf{k}}}{2}\, b_{\mathbf{k}}, \tag{2.141}$$

$$\beta_{\mathbf{k}} = -e^{i\varphi_{\mathbf{k}}} \sin\frac{\theta_{\mathbf{k}}}{2}\, a_{\mathbf{k}} + \cos\frac{\theta_{\mathbf{k}}}{2}\, b_{\mathbf{k}}. \tag{2.142}$$

where

$$\theta_{\mathbf{k}} = \arccos(\Delta/\omega_{\mathbf{k}}),\;\; \varphi_{\mathbf{k}} = \arg f_{\mathbf{k}}. \tag{2.143}$$

The spectrum thus consists of two symmetric bands with dispersion $\pm\omega_{\mathbf{k}}$ separated by the energy gap $\Delta\omega = 2|\Delta|$ [see Fig. 2.14(a) and (b)]. Importantly, each band features a valley around each Dirac point [see Fig. 2.14(b)], which in the remainder we will refer to as valley $\mathbf{K}$ and valley $\mathbf{K}'$.

2.9.4 Valleys K and K'

In each valley, sufficiently near the Dirac point, the band dispersion can be approximated as quadratic. Indeed, defining $\mathbf{K}_{+1}{=}\mathbf{K}$, $\mathbf{K}_{-1}{=}\mathbf{K}'{=}{-}\mathbf{K}$, we can approximate (2.138) in valley $\tau = \pm 1$ as

$$f(\mathbf{K}_\tau + \mathbf{q}) \simeq -\frac{3a}{2}(\tau q_y - i q_x) \tag{2.144}$$

for $q \ll |\mathbf{K}_\tau|$, that is $q \ll 1/a$. Accordingly, in this regime, and upon a suitable local redefinition of momentum coordinates, the Block Hamiltonian (2.137) in each valley takes the form

$$h_\tau(\mathbf{q}) = v\,(\tau q_x \sigma_x + q_y \sigma_y) + \Delta \sigma_z\,, \tag{2.145}$$

where we defined the characteristic speed

$$v = \frac{3}{2} a J\,. \tag{2.146}$$

Hamiltonian (2.145) has eigenvalues $\pm\sqrt{\Delta^2 + v^2 q^2}$, in agreement with the lowest-order expansion of the band dispersion (2.140) around each Dirac point.

Based on (2.145), the effective total Hamiltonian in valley τ for low frequencies takes the form of a two-dimensional massive Dirac Hamiltonian [61, 62]

$$H_\tau = v\,(\tau p_x \sigma_x + p_y \sigma_y) + \Delta \sigma_z\,, \tag{2.147}$$

with p_x (p_y) the effective momentum operator along the x (y) axis.

2.9.5 Topological properties of valleys

Based on the eigenstates of (2.145) and on Eq. (2.116), one can show that the Berry curvature [59] in each valley is given by [63]

$$\mathbf{\Omega}_\tau(\mathbf{q}) = \tau\,\frac{v^2\Delta}{2\,(\Delta^2 + v^2|\mathbf{q}|^2)^{3/2}}\,\hat{z}\,. \tag{2.148}$$

Therefore, the breaking of inversion symmetry ($\Delta \neq 0$) endows the two valleys with non-zero and opposite Berry curvatures. Also notice that $\mathbf{\Omega}_\tau$ is an odd function of Δ. Thus, although the *total* Berry curvature $\mathbf{\Omega}_- + \mathbf{\Omega}_+$ correctly integrates to zero as required by time-reversal symmetry [59], the *valley-polarized* Berry curvature remains finite and gives rise to a nontrivial geometric phase for a particle adiabatically encircling a single Dirac valley $\mathbf{K}_\tau$. Accordingly, each valley has a Chern number $C_\tau = \frac{1}{2}\tau\,\mathrm{sgn}(\Delta)$. As Δ goes from a positive to a negative value, a valley-polarized phase transition takes place with the gap closing at $\Delta = 0$.

Chapter 3

Non-Markovian decay of an atom due to Bloch oscillations

The study of qubits coupled to tailored low-dimensional photonic environments, mostly at the few-photon level, lies at the forefront of modern quantum optics, and especially waveguide QED [1, 3, 64], with potential applications for the effective processing of quantum information. Relying on the progress of experimental capabilities which nowadays enable the fabrication of unconventional photonic baths, e.g. lattices or 1D continuous waveguides, coupled to qubits in platforms such as photonic crystals in the optical domain [8], superconducting circuits in the microwaves [13, 14, 40] and matter-wave emulators [65, 66], the search for novel qubit-photon interaction paradigms is gaining momentum.

Within this general framework and concerning emission properties, two major classes of phenomena that do not occur in conventional quantum optics are receiving considerable attention, both at the theoretical and experimental level. One class explores the effect of a *band structure* of the photonic bath, which can cause effects such as fractional decay [5, 65, 67, 68], qubit-photon bound states [7, 9, 69] or dipole-dipole dispersive interactions with tunable-range [13, 70–73]. These phenomena require implementing a *periodic* photonic bath, namely a lattice, e.g. through an array of coupled cavities or resonators, in order to endow its spectrum with bands and bandgaps. Another important class of investigated phenomena focus on the non-Markovian regime where photon retardation times (time delays) become comparable or larger than the qubit decay time [23, 44–46], which can give rise to qubit revivals [24, 35], photon trapping [74], enhanced Dicke superradiance [75] or photonic cluster states [76]. These phenomena typically require implementing a one-dimensional photonic bath, which could also be just a standard continuous waveguide or transmission line, along with the introduction of a mechanism enforcing the emitted photon to return to the qubit, e.g. one or more mirrors, in a time larger than the qubit decay time.

In this chapter, we investigate the emission of a qubit into an infinitely long 1D coupled-cavity array where emitted light is accelerated by a synthetic *force* [see Fig. 3.1], which can be easily implemented in the lab through an engineered gradient of cavity frequencies mimicking a linear potential sensed by the photons. Despite the qubit being weakly coupled to the lattice, based on Bloch oscillations [55, 56] the synthetic force drives the emitted photon along the band until it hits a band edge. This gives rise to a confined motion of emitted light even in real space, despite no actual mirrors being present, resulting in rich non-Markovian dynamics. We identify two distinct regimes depending on the ratio between the Bloch oscillation period and the qubit decay time. When this ratio is small (strong-force regime), the system undergoes vacuum Rabi oscillations that are chiral in the sense that the qubit periodically exchanges energy with an extended region of the array lying either to its right or left, and this chirality can be controlled by tuning the qubit frequency. For large values of the aforementioned ratio (weak-force regime), the qubit instead shows a non-Markovian decay that features a series of revivals and secondary emitted wavepackets each one undergoing a round trip (before hitting back the qubit) whose duration and traveled distance depend on the force strength.

This chapter is organized as follows. In Section 3.1, we introduce the model and Hamiltonian. The field spectrum, the Wannier–Stark eigenstates, and Bloch oscillations were reviewed in Sections 2.7.1 and 2.7.1 of Chapter 2, and we draw on those results throughout. In Section 3.2, we present a numerical study of qubit emission in the regimes of strong and weak synthetic force, showing chiral vacuum Rabi oscillations and non-Markovian revivals. In Section 3.3, we develop a theoretical analysis of these phenomena, formulating a precise definition of the two regimes and showing explicitly that a qubit tuned to the band center obeys a delay differential equation analogous to that of a multi-mode cavity-QED system. In Section 3.4, we discuss potential experimental implementations. Finally, in Section 3.5, we present our conclusions and outline future directions. Some technical details are provided in the appendices.

3.1 Model and Hamiltonian

In this section, we explore further the lattice considered in Section 2.7.1. We consider a two-level qubit (quantum emitter) with ground (excited) state $|g\rangle$ ($|e\rangle$) and frequency ω_0, locally coupled to an infinite 1D array of coupled cavities labeled by integer n [see Fig. 3.1].

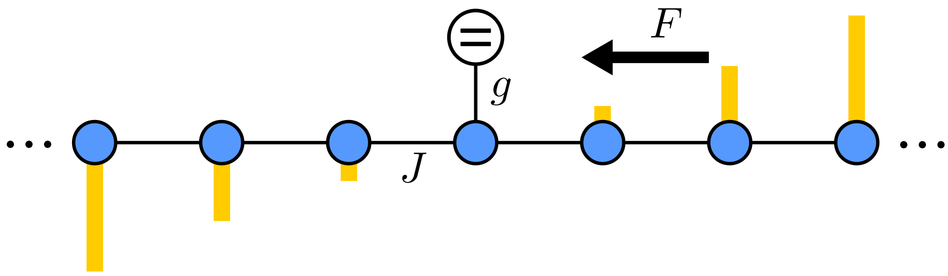

Figure 3.1: Qubit coupled to a one-dimensional finite lattice featuring a linear gradient on the cavity frequencies. The qubit couples at the central cavity with a strength g. The yellow bar depicts the potential variation, where the bar going down (up) represents negative (positive) values for the cavity frequency at that position.

The total Hamiltonian reads

$$H = \omega_0 \sigma_+ \sigma_- + H_B + g(a_{n_0}^\dagger \sigma_- + \text{H.c.})\,, \tag{3.1}$$

where H_B is the free Hamiltonian of the field given by,

$$H_B = \sum_n (nF)\, a_n^\dagger a_n - J \sum_n (a_{n+1}^\dagger a_n + \text{H.c.})\,. \tag{3.2}$$

The qubit is locally coupled under the rotating-wave approximation to cavity n_0 with strength g [cf. Eq. (3.1) and Fig. 3.1 where $n_0 = 0$]. In Eq. (3.2), the second sum is the standard tight-binding Hamiltonian describing photon hopping between nearest-neighbour cavities with $J > 0$ the hopping rate. The first sum instead accounts for the bare Hamiltonian of every single cavity: note that cavity frequencies are *non-uniform* in that they increase linearly with the cavity index n with slope F. Accordingly, the first sum in Eq. (3.2) is naturally interpreted as an effective scalar potential on the photons whose corresponding *force* (opposite of gradient) is measured by F.

The energy spectrum and eigenstates of H_B, together with the resulting Bloch oscillations, were reviewed in Sections 2.7.1 and 2.7.1 of Chapter 2. The key results (the Wannier-Stark ladder (2.73), the Bessel-function eigenstates (2.74), and the oscillation period (2.80)) will be used extensively in what follows.

3.2 Dynamics of qubit emission via numerical simulations

The goal of this chapter is to study the emission properties of the qubit, i.e., the dynamics arising from the initial state $|\Psi(0)\rangle = |e\rangle$ (qubit excited and field in the vacuum state). This section illustrates some typical properties of the emission dynamics based on numerical simulations in real and momentum space. Due to conservation of the total number of excitations, the joint evolved state at any time t can be arranged in the form

$$|\Psi(t)\rangle = \alpha_e(t)\,|e\rangle + \sum_n \beta_n(t)\,|n\rangle \tag{3.3}$$

with $\alpha_e(t)$ and $\beta_n(t)$ the probability amplitudes to find the system in state $|e\rangle$ and $|n\rangle$, respectively, at time $t \geq 0$. To perform the numerical simulation we represent the propagator as $U(t) = e^{-iHt}$, with H given by Eq. (3.1), in the basis $\{|e\rangle, \{|n\rangle\}\}$, which gives rise to a square matrix of dimension $N + 1$. With this matrix one can simply apply a numerical matrix exponentiation[1] to the column vector corresponding to the initial state $\alpha_e(0) = 1$ and $\beta_n(0) = 0$ for all n, and obtain the evolved amplitudes $\alpha_e(t)$ and $\beta_n(t)$ that fully specify $|\Psi(t)\rangle$.

An alternative yet useful representation of the dynamics is in terms of the single-photon momentum basis (2.61). In this picture, the evolved joint state reads

$$|\Psi(t)\rangle = \alpha_e(t)\,|e\rangle + \sum_k \alpha_k(t)\,|k\rangle\ , \tag{3.4}$$

which differs from (3.3) in that the field is now represented in the momentum space. In Section 3.2.2 we will use both pictures to get insight into the emission dynamics.

Throughout this chapter, we will consider values of g [cf. Fig. 3.1 and Eq. (3.1)] such that $g \ll J$. The rationale of this choice is that for $F = 0$ a qubit tuned within the photonic band (having width $\propto J$) is in the standard Markovian regime (a case which we will review at the beginning of Section 3.2.2). Accordingly, the occurrence of non-Markovian effects, if any, stems from the introduction of the synthetic force, which is the main focus of this chapter. Throughout this section, we will consider the case

[1]For this thesis the matrix exponentiation method used was the `expm_multiply` from the SciPy package, since it implements an efficient matrix exponentiation of a sparse matrix applied to a vector.

$n_0 = 0$, i.e. a qubit coupled to cavity $n_0 = 0$ as in Fig. 3.1.

In what follows, we analyze first chiral vacuum Rabi oscillations (Section 3.2.1) and then non-Markovian decay with revivals (Section 3.2.2), corresponding respectively to the regimes of strong and weak values of force F. A rigorous definition of these two regimes will be discussed in Section 3.3.1.

3.2.1 Chiral vacuum Rabi oscillations

As discussed in Section 2.7.1, for $F > 0$ the bare field spectrum is the discrete Wannier-Stark ladder [see Eq. (2.73) and Fig. 2.8(b)]. Accordingly, by tuning the qubit close to one of the field normal frequencies $\omega_n = nF$ and provided that the force (modes energy spacing) is large enough compared to the effective qubit-mode coupling strength (more on this in Section 3.3.1), one expects vacuum Rabi oscillations to occur since the qubit in fact interacts resonantly with only one field eigenstate $|\varphi_n\rangle$. This is indeed the case as shown in Fig. 3.2, where we consider the initial state $|\Psi(0)\rangle = |e\rangle$ and plot the time evolution of the qubit excited-state population $|\alpha_e(t)|^2$ [panel (a)] and real-space photon density $|\beta_n(t)|^2$ [panels (b)–(d)] for $g = 0.01J$, $F = 0.5J$ and the three representative qubit frequencies $\omega_0 = 0, \pm 3F$. While the qubit undergoes undamped

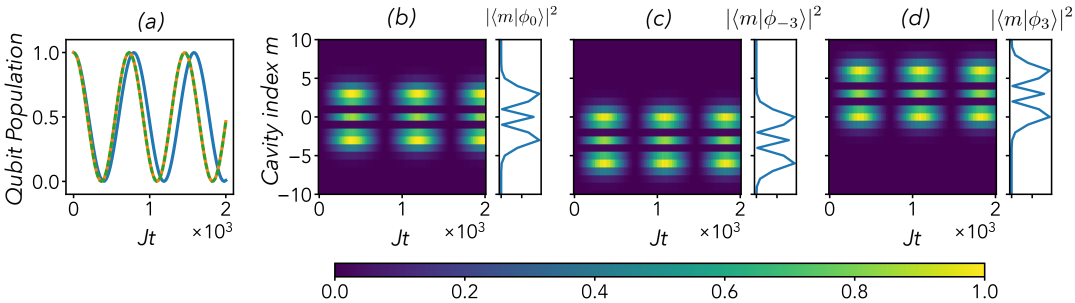

Figure 3.2: Vacuum Rabi oscillations under a strong synthetic force. (a) Time behaviour of the qubit excited-state population $|\alpha_e|^2$ for $\omega_0 = 0$ (solid blue curve), $\omega_0 = -3F$ (solid orange) and $\omega_0 = 3F$ (dashed). (b) Real-space photon density $|\beta_n|^2$ versus time for $\omega_0 = 0$ [panel (b)], $\omega_0 = -3F$ (c) and $\omega_0 = 3F$ (d). We consider the initial state $|\Psi(t = 0)\rangle = |e\rangle$. Throughout we set $n_0 = 0$, $g = 0.01J$ and $F = 0.5J$. Time is expressed in units of J^{-1}. In each of panels (b)-(d), the photon density is normalized to its maximum value for each respective case. To the right of each of panels (b)-(d), we also show for comparison the spatial profile of $|\langle m|\varphi_n\rangle|^2$ for $n = 0$ (b), $n = -3$ (c) and $n = 3$ (d). Simulation done with a lattice of $N = 24$ sites.

oscillations, a region of lattice gets periodically populated, which witnesses the expected qubit-field energy swap typical of vacuum Rabi oscillations. Notice that, despite the qubit being directly coupled to cavity $n_0 = 0$, several cavities in a range of size $\sim \xi$ [cf. Eq. (2.75)] get populated according to a pattern that features secondary maxima and minima. Even more interestingly, depending on the qubit frequency, such a region can be significantly displaced from cavity $n_0 = 0$ (qubit location) either to the left, as in panel (c), or to the right, as in panel (d). This shows the occurrence of chiral reversible emission into the lattice, whose chirality can be controlled by simply tuning the qubit frequency. The structured pattern of the emitted photon density reflects the shape of a specific field eigenstate [cf. Eq. (2.74) and Fig. 2.9], specifically $|\varphi_0\rangle$ in the case of panel (b), $|\varphi_{-3}\rangle$ in panel (c) and $|\varphi_3\rangle$ in (d). This is confirmed by the behaviour of $|\langle m|\varphi_n\rangle|^2$ for $n = 0, \pm 3$ which is displayed for comparison on the right of each of panels (b)-(d) [2].

Interestingly, unlike a number of recent works [77–80], the chiral nature of the above dynamics here is not due to topological properties, but rather to the fact that photonic eigenmodes of different frequencies are localized around different cavities of the array. A more detailed description of vacuum Rabi oscillations will be provided in Section 3.3.2.

3.2.2 Non-Markovian decay with revivals

We next investigate situations in which the qubit significantly interacts with a very large number of field eigenstates, which in particular requires F to be weak enough (compared to the coupling strength) so as to make the ladder spectrum dense [recall Eq. (2.73) and Fig. 2.8(b)]. Unlike vacuum Rabi oscillations in Section 3.2.1, the qubit is now expected to undergo an irreversible decay, although generally non-Markovian. In Fig. 3.3, we plot the time evolution of the qubit excitation (upper panels) and

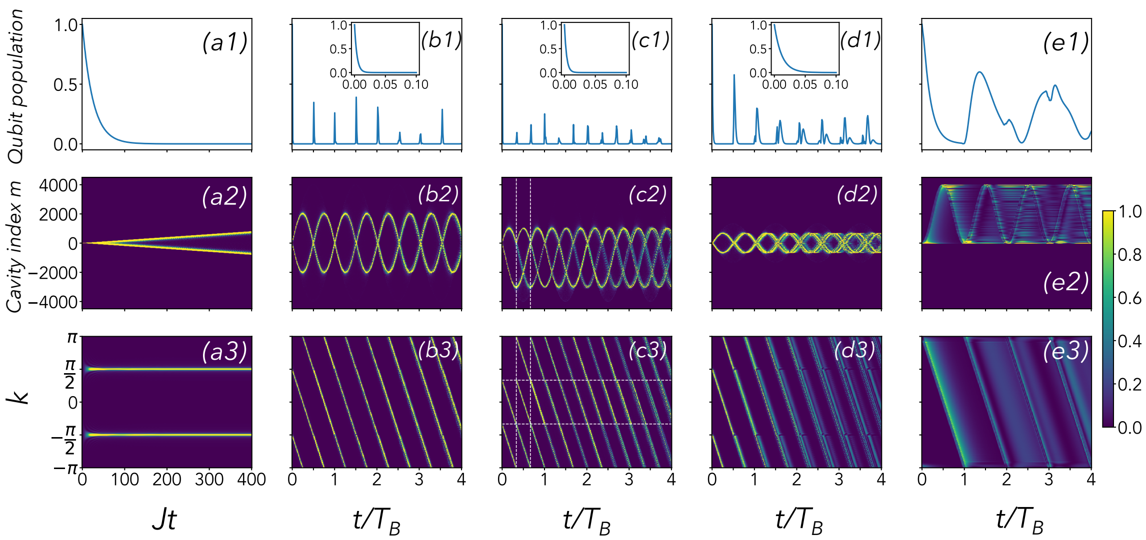

Figure 3.3: Emission dynamics under a weak synthetic force. Upper panels show the time behavior of the qubit population $|\alpha_e|^2$, while middle (lower) panels show the evolution of photon density in real (quasi-momentum) space $|\beta_m|^2$ ($|\alpha_k|^2$). We set $\omega_0 = 0$, $g = 0.2J$, $F = 0$ [panels (a1)-(a3)], $\omega_0 = 0$, $g = 0.2J$, $F = 10^{-3}J$ [panels (b1)-(b3)], $\omega_0 = -J$, $g = 0.2J$, $F = 10^{-3}J$ [panels (c1)-(c3)], $\omega_0 = 0$, $g = 0.2J$, $F = 3 \cdot 10^{-3}J$ [panels (d1)-(d3)] and $\omega_0 = 1.966J$, $g = 0.01J$, $F = 10^{-3}J$ [panels (e1)-(e3)]. The insets in panels (b1), (c1) and (d1) show a zoom of the qubit decay in the early stages of the dynamics. The vertical dashed lines in (c2) and (c3) mark the return times of the first two emitted wavepackets, while the pair of horizontal dashed lines in (c3) correspond to $k = \pm k_0$. In central and lower panels, photon density is rescaled to its maximum value. Time is units of J^{-1} in (a1), (a2) and (a3) and of $T_B = 2\pi/F$ in all the remaining cases. Simulation done with a lattice of $N = 9000$ sites.

[2]Note that this is an even function of m despite $\langle m|\varphi_0\rangle$ is not, which follows from the parity property of Bessel functions $J_{-n}(\xi) = (-1)^n J_n(\xi)$ [54]. For the specific value of F set in this example, Eq. (2.75) yields $\xi = 4$, which matches the range of the array being populated during the evolution [cf. Fig. 3.2(b)-(d)]

photon density in real and momentum space (central and lower panels, respectively) for different yet weak values of F.

In the trivial case $F = 0$ [cf. Fig. 3.3(a1)-(a3)], as expected (see e.g. Ref. [81]) the qubit undergoes standard Markovian emission with decay rate (for $\omega_0 = 0$)

$$\Gamma = \frac{g^2}{J}\,. \tag{3.5}$$

The emitted field [cf. Fig. 3.3(a2)] splits into a pair of wavepackets propagating away from the qubit at constant speed, one to the right and one to the left. This is because the qubit couples predominantly to almost resonant modes with $k \simeq \pm k_0$ such that $\omega_{\pm k_0} = \omega_0$, as confirmed by the emitted field evolution in momentum space shown in Fig. 3.3(a3). These modes have speed $v_{\pm k_0} = \pm 2J \sin k_0$, which for the considered case $\omega_0 = 0$ reduce to $v_{\pm k_0} = \pm 2J$ corresponding to the velocity of the right-propagating and left-propagating wavepackets.

We next discuss Fig. 3.3(b1)-(c3), where we set $F = 10^{-3}J$ while $\omega_0 = 0$ [panels (b1), (b2), (b3)] and $\omega_0 = -J$ [panels (c1), (c2), (c3)]. Clearly, introducing the weak force F dramatically changes the emission dynamics. The qubit population [cf. Fig. 3.3(b1) and (c1)] first decays exponentially with rate (3.5) and then generally shows a sequence of partial revivals with the field comprising a series of secondary wavepackets being emitted from the qubit at different times. Unlike the case $F = 0$, the emitted photon now undergoes an accelerated motion, as witnessed by the nonlinear time dependence of the average position of each wavepacket emitted to the left or right during the dynamics [cf. Fig. 3.3(b2) and (c2)]: this typically propagates away and slows down until an inversion of motion occurs, and next returns to the qubit at increasing speed. As the wavepacket hits back the qubit, this generally undergoes a partial revival [cf. Fig. 3.3(b1) and (c1)]. Interestingly, in striking contrast to the trivial dynamics for $F = 0$ [see Fig. 3.3(a3)], in momentum space [cf. Fig. 3.3(b3) and (c3)] each emitted wavepacket evolves linearly in time in agreement with Eq. (2.79) and Section 2.7.1. This motion is yet constrained owing to the finite size of the FBZ, which enforces a wavepacket reaching the left edge of the FBZ at $k{=}-\pi$ to instantaneously reappear from the right edge at $k{=}\pi$. In this momentum space, as an emitted wavepacket of momentum $\pm k_0$ is back to the qubit (return time) its momentum is reversed (i.e., $\pm k_0 \to \mp k_0$). Notice that, at this return time, a new pair of wavepackets of quasi-momenta $\pm k_0$ are generated, which is more apparent in panel (c3) as highlighted by the horizontal dashed lines showing that the momentum of an emitted wavepacket is always k_0 or $-k_0$ [the dashed vertical lines show the return times of the two wavepackets emitted at time $t = 0$ and are also displayed in panel (c2)].

The set of *return times* t_r at which emitted wavepackets are back to the qubit [see Fig. 3.3(b2)-(b3)] result from the combined effect of Bloch oscillations and the fact the qubit mostly couples to almost resonant plane waves $|k(t)\rangle$ such that $\omega_{k(t)} \simeq \omega_0$ (cf. Section 2.7.1). For $\omega_0{=}0$ [cf. Fig. 3.3(b2) and (b3)], t_r are multiple integers of half the Bloch oscillations period, i.e., $t_r = \nu T_B/2$ with $\nu = 1, 2, ...$ [cf. Eq. (2.80)]. To see this note that, based on the k-space picture in Section 2.7.1 and Fig. 2.10, at $t = 0$ the almost resonant momenta are $\pm k_0$ with $k_0 = \pi/2$. After a time $T_B/2$, we get $\pm k_0 \to k(t{=}T_B/2) = \mp k_0$: at this time, based on Eqs. (2.84) and (2.85) for $x_i = 0$ and $k_i = \pm k_0 = \pm\pi/2$, either wavepacket is thus back to the initial average position and its energy is again resonant with the qubit which can thus get (partially) re-

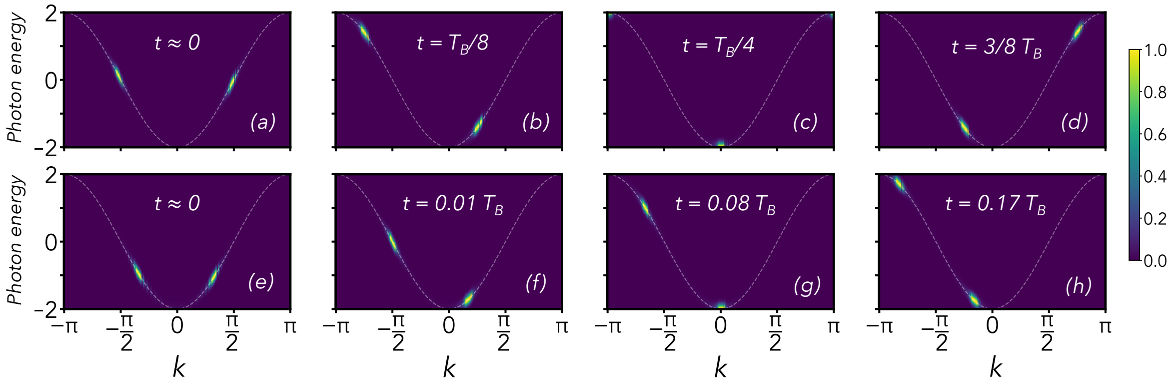

Figure 3.4: Time behavior of the photon density on the energy-momentum space for $\omega_0 = 0$, $g = 0.2J$ and $F = 10^{-3}J$ (upper panels) and $\omega_0 = -J$, $g = 0.2J$ and $F = 10^{-3}J$ (lower panels). At a given time t, we numerically compute $|\beta_k(t)|^2$ for each value of k within the FBZ and build up the string $\{k, \omega = -2J\cos k, |\beta_k(t)|^2\}$, which is then used to produce a density plot on the plane k-ω. The dashed line shows the photon dispersion law (2.60), superimposed on the density plot for comparison. The photon density is rescaled to its maximum value in each panel. Simulation done with a lattice of $N = 10000$ sites.

excited. The qubit next decays back by generating two new wavepackets with $k \simeq \pm k_0$ which again undergo an analogous evolution before returning to the qubit at time $t_r = T_B$, and so on. This is confirmed by Fig. 3.4(a)-(d) where, for the same case as in Fig. 3.3(b1), (b2) and (b3), we plot the time evolution of the photon density on the energy-momentum space. As expected, the emitted wavepackets propagate along the photon dispersion law (dashed curve), which makes them off-resonant with the qubit during the evolution until they both return to the band center thus re-establishing resonance. This representation additionally makes apparent the confining effect of band edges at $\omega = \pm 2J$ (where inversions of motion occur), which work as a pair of effective “mirrors" but in the energy domain, this being the ultimate reason of the non-Markovian nature of the dynamics.

For ω_0 not lying at the band center (but still far from the band edges), as in Fig. 3.3(c1), (c2) and (c3), wavepackets emitted to the right and those to the left now evolve *differently* in terms of both the distance traveled up to an inversion of motion and return times, as can be seen from panels (c2) and (c3). This is best understood in the energy-momentum space, displayed in the lower panels of Fig. 3.4: since ω_0 is no longer at the band center, the time taken by the emitted wavepacket of initial average momentum $+k_0$ to evolve into $-k_0$ is now shorter than the time taken by the wavepacket $-k_0$ to turn into $+k_0$ (for $0<\omega_0<2J$ the converse statement would hold) with the two times summing to T_B. By using again Eqs. (2.84) and (2.85), this entails that the former wavepacket travels a shorter distance before undergoing an inversion of motion and returns earlier to the qubit. This is reflected, in particular, by the first two qubit revivals in Fig. 3.3(c1), one shorter one longer than $T_B/2$. Since, as said, as a wavepacket is reabsorbed a new pair of wavepackets of opposite momenta $\pm k_0$ are generated, a series of return times of growing density arises as is apparent in Fig. 3.3(c2) and (c3), corresponding to an increasingly complex pattern of qubit revivals [see Fig. 3.3(c1)]. The series of return times can be predicted as a function of ω_0 by using Eq. (2.84), based on which a wavepacket $\pm k_0$ emitted at time t_i is back to the qubit at time $t_r(t_i, \pm k_0)$ given by (see Appendix B.1)

$$t_r(t_i, sk_0) = t_i + \left(\delta_{s,-1} + s\,\frac{k_0}{\pi}\right) T_B \quad \text{for } s = \pm 1 \; . \tag{3.6}$$

Taking $t_r(t_i, \pm k_0)$ as the initial time of the next generated pair of wavepackets (one with momentum k_0 one with $-k_0$) the return times of these can be calculated again through Eq. (3.6). Iterating this procedure (starting from $t_i = 0$) yields the series of all return times as a function of ω_0 (see Appendix B.1).

The above discussion holds for F weak enough and ω_0 not too close to a band edge. Evidence of this is provided by Fig. 3.3(d1)-(d3), where we reconsider the case $\omega_0 = 0$ as in panels (b1)-(b3) but now for a stronger force, and by Fig. 3.3(e1)-(e3) where ω_0 is parked in the vicinity of the upper band edge. In the first case, the trajectories of emitted wavepackets become less and less defined and, correspondingly, the qubit revivals increasingly wider and structured. In the latter case, zero plateaux in the qubit population not even occur, which can be understood from the fact that wavepackets emitted to the left take a negligible time to return to the qubit. The distance traveled by such wavepackets is also vanishing, explaining why – remarkably – emission is almost fully chiral in this case. This is confirmed by Eq. (2.84), which for $k_i \simeq \pi$ (corresponding to the upper band edge) reduces to

$$x(t) - x_i \simeq \xi \left[1 - \cos\left(2\pi\,\frac{t - t_i}{T_B}\right)\right] , \tag{3.7}$$

showing that $0 \lesssim x(t) - x_i \lesssim 2\xi$ in agreement with Fig. 3.3(e2).

In Fig. 3.3(b1)-(e3) we set values of the synthetic force of the order of $F{\sim}10^{-3}J$ in order to robustly satisfy the condition for entering the weak-force regime and thus better showcase the essential physics. Numerical simulations performed for $F{\sim}10^{-2}J$ (an order of magnitude larger) show that qubit revivals and photon bouncing become less sharp, yet their visibility remains sufficiently pronounced especially during the first one or two revivals.

A comprehensive analytical description of the complex emission dynamics in the weak-force regime is demanding and goes beyond the scope of this chapter. In Section 3.3.3, we will however demonstrate that in the regime $\omega_0 = 0$ (qubit tuned at the band center) and F weak enough the qubit decay is governed by a delay differential equation.

3.3 Theoretical analysis

In line with the standard approach to treat light-matter interactions in photonic lattices in quantum optics and open quantum systems [68, 82], it is natural to represent the dynamics in terms of the bare field's spectrum and eigenstates, which were reviewed in Section 2.7.1. Resorting again to the conservation of the total number of excitations, the joint evolved state at any time t during the emission process can also be written as

$$|\Psi(t)\rangle = \alpha_e(t)\,|e\rangle + \sum_n \alpha_n(t)\,|\varphi_n\rangle \; , \tag{3.8}$$

where $\alpha_n(t)$ is now the probability amplitude to find the system at time t in state $|\varphi_n\rangle$ [recall Eq. (2.74)]. Eq. (3.8) differs from Eqs. (3.3) and (3.4) in that it is expressed in terms of the field's eigenstates $\{|\varphi_n\rangle\}$.

Replacing (3.8) into the Schrödinger equation $i\frac{d}{dt}|\Psi(t)\rangle = H\,|\Psi(t)\rangle$ with H given by Eq. (3.1) gives rise to the system of differential equations (in a frame rotating at the qubit frequency ω_0)

$$\dot{\alpha}_e = -i\sum_n g_n\,\alpha_n\,,\quad \dot{\alpha}_n = -i(\omega_n-\omega_0)\alpha_n - ig_n\alpha_e \tag{3.9}$$

with ω_n the Wannier-Stark ladder spectrum given by Eq. (2.73) [see also Fig. 2.8(b)] and where we defined the coupling-mode function

$$g_n = g\langle n_0|\varphi_n\rangle = g\,J_{n_0-n}(\xi)\,. \tag{3.10}$$

3.3.1 Regimes of light-matter interaction

Similarly to a multi-mode perfect cavity (which also features a ladder spectrum of normal frequencies) [83, 84], the number of field eigenstates $|\varphi_n\rangle$ which must be accounted for to describe the qubit emission depends on how large the field energy *spacing* is $\Delta\omega_n = F$ compared to the *characteristic strength* of the coupling mode function g_n. Recalling that each field eigenstate is localized in a region of length $\sim\xi$ [cf. Eq. (2.75)], the latter can be estimated as

$$\bar{g} \sim \frac{g}{\sqrt{\xi}}\,. \tag{3.11}$$

Accordingly,

$$\frac{\bar{g}}{\Delta\omega_n} \sim \sqrt{\Gamma T_B}\,, \tag{3.12}$$

where we recall that Γ and T_B are respectively the qubit decay rate for $F = 0$ [cf. Eq. (3.5)] and the Bloch oscillations period [cf. Eq. (2.80)].

Therefore, the key parameter is the dimensionless quantity ΓT_B, namely the ratio between the period of Bloch oscillations and the qubit decay time (for $F = 0$). Accordingly, the strong (weak) force regime can be identified by the condition $\Gamma T_B \ll 1$ ($\Gamma T_B \gg 1$). The physical interpretation is that for $\Gamma T_B \ll 1$ the characteristic time taken by light to travel across the band is negligible compared to the qubit decay time. Conversely, for $\Gamma T_B \gg 1$, the qubit has enough time to decay to the ground state before a Bloch period is complete.

3.3.2 Strong-force: vacuum Rabi oscillations

For $\Gamma T_B \ll 1$ we are in the strong force regime, which is the one involved in Section 3.2.1 (indeed the parameters set in Fig. 3.2 yield $\Gamma T_B \sim 10^{-3}$). Accordingly, by tuning the qubit frequency such that $\omega_0 \simeq \omega_{n_c}$ for one selected field normal frequency ω_{n_c}, all field normal modes with $n \neq n_c$ can be neglected and one reduces to an effective Jaynes-Cummings model where the cavity mode is embodied by the field eigenstate $|\varphi_{n_c}\rangle$. Interestingly, recall that (in general) this mode has asymmetric spatial shape [cf. Fig. 2.9] and, even more remarkably, is not spatially centered at the qubit location being indeed localized around cavity n_c with characteristic width ξ [see Eq. (2.75) and Fig. 2.9]. These features are reflected in the form of the effective qubit-mode coupling strength which is given by [cf. Eq. (3.10)] $g_c = g\,J_{n_0-n_c}(\xi)$. In order for such interaction to be significant, the qubit must be thus placed within a distance $\sim\xi$ from the mode center, producing the condition $|n_0 - n_c| \lesssim \xi$ (recall Section 2.7.1). Hence, ξ plays the role of the cavity length with the last condition saying the qubit must be placed inside this effective cavity in order to appreciably interact with it.

From standard cavity QED theory [85], the effective Rabi frequency is given by $\Omega = \sqrt{\delta^2 + 4g_c^2}$ with δ the detuning from the cavity mode, which in the present system explicitly reads

$$\Omega = \sqrt{(\omega_0 - \omega_{n_c})^2 + 4g^2\, J^2_{n_0 - n_c}(\xi)} \tag{3.13}$$

with $\omega_{n_c} = n_c F$.

For $n_0 = 0$, this correctly matches the frequency of vacuum Rabi oscillations in Fig. 3.2 in the cases $\omega_0 = 0$, $n_c = 0$ and $\omega_0 = \pm 3F$, $n_c = \pm 3$. It is now apparent that for $n_c > n_0$ ($n_c < n_0$) and $\omega_0 \simeq \omega_{n_c}$ the effective cavity mode lies on the right (left) of the qubit, explaining why the chirality of vacuum Rabi oscillations can be controlled by tuning the qubit frequency.

3.3.3 Weak-force: delay differential equation

Let us now discuss the more involved weak-force regime $\Gamma T_B \gg 1$, in which case the qubit will see a dense set of field normal modes as discussed in Section 3.3.1. This demands a multi-mode description of the dynamics based on the differential system (3.9).

For the sake of argument and in line with Fig. 3.3 and Fig. 3.4, henceforth we will set $n_0 = 0$. Solving for each $\alpha_n(t)$ as a function of $\alpha_e(t)$ in the second identity of Eqs. (3.9) and replacing in the first identity gives rise to a closed integro-differential equation for $\alpha_e(t)$ only that reads

$$\frac{d\alpha_e}{dt} = -g^2 \int_0^t d\tau\, K(\tau)\, \alpha_e(t-\tau)\ . \tag{3.14}$$

Using $J_{-n}(\xi) = (-1)^n J_n(\xi)$ the memory kernel is given by

$$\begin{aligned} \mathcal{K}(\tau) &= \sum_{n=-\infty}^{\infty} [J_n(\xi)]^2\, e^{-i(Fn - \omega_0)\tau}\,, \\ &= e^{i\omega_0 \tau} J_0\left[\xi \sin\left(\pi \tfrac{\tau}{T_B}\right)\right]. \end{aligned} \tag{3.15}$$

where in the second identity we worked out the series as a Bessel function of the first kind of order zero yet with an oscillatory argument (see e.g. Ref. [51]). The memory kernel function thus has a periodic behaviour with a period given by T_B, witnessing the intrinsically non-Markovian nature of the qubit decay.

Eq. (3.14) fully describes the qubit decay dynamics, but it is hard to treat in general due to the complicated form of the memory kernel function. Thus in order to infer information about the physics of the problem, approximations are needed in order to arrange the equation in a more intuitive form. We show next that this task can be accomplished in the case that the qubit frequency lies at the band center, i.e. for $\omega_0 = 0$.

To show this, notice that, out of all the field eigenstates $|\varphi_n\rangle$, the qubit will predominantly interact with those of frequency such that $\omega_n \simeq \omega_0$ (almost resonant eigenstates) corresponding to slowly-varying terms in the first identity of (3.15). Now, since

$\omega_n = nF$ [cf. Eq. (2.73)], it turns out that these eigenstates are also such that $n \simeq 0$, i.e., they are the spatially nearest to the qubit location. More in detail, recalling Eq. (3.11), these are all states $|\varphi_n\rangle$ fulfilling $|n| \lesssim n_{\max}$ where $n_{\max}$ can be estimated as $n_{\max} = \bar{g}/\Delta\omega_n$. Now, since $g \ll J$ (as assumed throughout), it turns out that $\bar{g}/\Delta\omega_n \ll \sqrt{\xi}$ [3]. Hence, we find that almost resonant eigenstates in this case satisfy the condition $|n| \ll \sqrt{\xi}$. This means that the qubit lies far enough from the tails of the wavefunction of each of such eigenstates, allowing us to approximate each of them as having a sinusoidal shape based on Eq. (2.76). Accordingly, in this regime, the memory kernel (3.15) can be effectively approximated as

$$\mathcal{K}(\tau) \simeq \frac{2}{\pi\xi} \sum_{n=-\infty}^{\infty} \sin^2\left(n\frac{\pi}{2} + \xi + \frac{\pi}{4}\right) e^{-iFn\tau} \tag{3.16}$$

By decomposing next the sine function into complex exponentials, this can be equivalently written (see Appendix B.2) as a sum of Dirac delta functions

$$\mathcal{K}(\tau) = \frac{T_B}{\pi\xi} \Big[\sum_{\ell=0}^{\infty} \delta(\tau - \ell T_B) + \sin(2\xi) \sum_{\ell=0}^{\infty} \delta[\tau - (\ell + \frac{1}{2} T_B)] \Big]. \tag{3.17}$$

Replacing this back into Eq. (3.14), one eventually ends up with the non-Markovian differential equation governing the qubit emission:

$$\begin{aligned} \frac{d\alpha_e}{dt} = &- \frac{\Gamma}{2}\alpha_e(t) - \Gamma \sum_{\ell=1}^{\infty} \alpha_e(t - \ell T_B)\Theta\left(t - \ell T_B\right) \\ &- \Gamma \sin(2\xi) \sum_{\ell=0}^{\infty} \alpha_e[t - (\ell + \tfrac{1}{2})T_B]\ \Theta[t - (\ell + \tfrac{1}{2})T_B] \end{aligned} \tag{3.18}$$

with $\Theta(x)$ the Heaviside step function. Mathematically, Eq. (3.18) is an instance of delay differential equation [86] whose corresponding memory kernel function peaks at multiple integers of $T_B/2$ which coincide with the return times t_r of emitted wavepackets during the dynamics (see Section 3.2.2). The dynamics governed by Eq. (3.18) can be worked out by solving exactly the generally inhomogeneous differential equation in each time interval $t \in [\ell T_B/2, (\ell+1)T_B/2[$ and using the resulting solution to define the inhomogeneous term to solve the equation in the next time interval [86]. We checked that the full solution of Eq. (3.18) resulting from this iterative procedure accurately reproduces the one obtained from numerical simulations provided that F is small enough [as is e.g. the case in Fig. 3.3(b1)]. For times shorter than $T_B/2$, only the first term in the right-hand side of Eq. (3.18) is non-zero: in this initial time interval, the qubit is effectively unaware of the presence of the electric field and undergoes the standard exponential decay according to $\alpha_e(t) = e^{-\frac{\Gamma}{2}t}$. At time $t = T_B/2$, the first revival generally occurs [see second line of Eq. (3.18)] corresponding to the first return time of the two previously emitted wavepackets. Interestingly, notice that in Eq. (3.18) terms corresponding to odd multiple integers of $T_B/2$ (second line of the equation) can identically vanish whenever $\xi = \nu\pi/2$ corresponding to the force values $F = 4J/(q\pi)$ with q an integer number, which is due to destructive interference of two emitted wavepackets as they return to the qubit. In these cases, qubit revivals at odd multiple

[3] Indeed, with the help of Eq. (2.75) we get $\frac{\bar{g}}{\Delta\omega_n} \sim \frac{g}{\sqrt{2JF}} \ll \frac{J}{\sqrt{2JF}} \sim \sqrt{\xi}$.

integers of $T_B/2$ do not occur, which we numerically checked.

Eq. (3.18) is formally analogous to the delay differential equation [87] (see also Ref. [48] corresponding to the case where $\sin(2\xi)=0$) governing the decay of an atom placed in the middle of a perfect cavity in the regime where, differently from the usual Jaynes-Cummings model, one has to take into account the multi-mode nature of the cavity and, consistently, the time delay t_d taken by a photon to travel between the two cavity mirrors (with t_d scaling as L/v where L is the cavity length and v the photon speed). The role of t_d and L in our system are played by T_B and ξ, respectively. A more thorough comparison between our delay differential equation and the one describing the decay of an atom in a multi-mode cavity is presented in Appendix B.3.

Interestingly, in a cavity, the non-Markovian decay with revivals originates from the spatial confinement due to the actual cavity mirrors. Instead, in the present mirrorless setup it is caused by the combined effect of the synthetic force and band finiteness: the former makes the emitted photon change its momentum and energy in time while the latter constrains this motion through band edges. From the viewpoint of an experimental observation of qubit revivals, compared to a standard cavity (or equivalently a homogeneous lattice with fixed ends) the present system provides an interesting potential advantage in that it replaces the role of the emitter's position (which is usually hard to control in an experiment) with its frequency (a usually tunable knob in most if not all platforms). This allows to control emission properties in the presence of "mirrors" without the need to change the emitter's actual position.

3.3.4 Differences from an atom in a conventional cavity

While, as discussed, the physics of the present system shares some features with an atom in a standard cavity, there are as well non-trivial differences which are highlighted next. In the strong-force regime (cf. Fig. 3.2 and Section 3.2.1), the chirality of the field dynamics during vacuum Rabi oscillations has no analogue in a conventional cavity where all sine-shaped field modes have the same spatial support (the region between the two mirrors) in contrast to the relative displacement of Bessel modes in the present system (see Fig. 2.9), a hallmark of our system that is key to the chiral behavior. In the weak-force regime, the qubit revivals - as we previously pointed out - resemble those caused by photon reflections from mirrors in a standard multi-mode cavity. However, the field dynamics differs significantly: the photon experiences all the time a non-uniform acceleration [see Fig. 3.3(b2),(c2),(d2),(e2)] not just upon reaching a band edge; this is at variance with a conventional cavity where the photon undergoes impulsive acceleration/force only upon hitting a mirror.

In general, we can state that although the two systems share a ladder-like energy spectrum of the field - resulting in some common features in their behavior - the field normal modes have very different shapes. As a consequence, all physical features that are sensitive to the shape of the normal modes of the photonic bath, particularly those related to the field dynamics, generally differ between the two systems.

3.4 Experimental implementations

The predicted phenomena can be potentially implemented in any state-of-the-art waveguide-QED platform enabling the fabrication of a 1D photonic lattice coupled to quantum emitters [64]. Two particularly promising implementations are superconducting arrays of resonators coupled to transmon qubits [13, 14, 88] and matter-wave emulators employing cold atoms in optical lattices [65, 66, 89–92]. In these setups, high-quality factors and very limited dissipation ensure that Eq. (3.1) captures the whole qubit-field dynamics with very good approximation.

While the strong-force regime entailing vacuum Rabi oscillations is straightforward to achieve, the weak-force regime, where non-Markovian decay with revivals occur, demands the gradient of cavity frequencies (i.e., the force) to be small but yet large enough with respect to the unavoidable disorder. In state-of-the-art superconducting coupled-resonator arrays [14, 88, 93], for instance, typical ranges of the hopping rate and coupling strength are respectively $J/(2\pi) \sim 100-300\,\text{MHz}$ and $g/(2\pi) \sim 1-100\,\text{MHz}$, but due to fabrication imperfections the frequency of each resonator is subject to disorder with a typical uncertainty $\sigma_\omega/(2\pi) \sim 1\,\text{MHz}$ which thus imposes the requirement $F > \sigma_\omega$. As an instance, a device with $g/(2\pi) \sim 50\,\text{MHz}$, $J/(2\pi) \sim 300\,\text{MHz}$ and $F/(2\pi) \sim 5\,\text{MHz}$ would match this condition and appear within reach or at least not far-fetched.

Numerical simulations used to assess the robustness of the system against disorder are shown in Fig. 3.5. For a disorder strength of $\sigma/J = 3 \times 10^{-3}$, which is more than one order of magnitude smaller than the synthetic field F [see Fig. 3.5(b)and (d)], the dynamics is virtually indistinguishable from the disorder-free case. To quantify the effect of disorder, we analyze the average height of the first qubit revival as a function of the disorder strength [Fig. 3.5(e)]. The results show that the first revival remains robust for disorder strengths up to approximately $\sigma/J \lesssim 10^{-2}$.

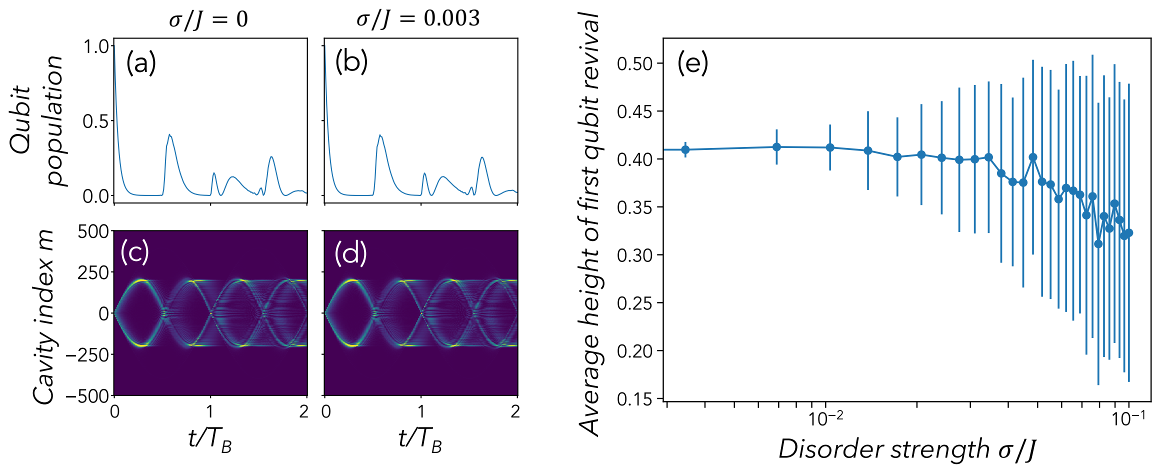

Figure 3.5: Analysis of the effect of disorder in the cavity frequencies. Panels (a) and (c) correspond to the disorder-free system, while panels (b) and (d) show the dynamics for a disorder strength of $\sigma/J = 0.003$. Panel (e) shows the height of the first qubit revival as a function of the disorder strength. Each point represents an average over 100 disorder realizations, and the error bars indicate one standard deviation. All simulations were performed with $\omega_0 = 0$, $g = 0.2J$, and $F = 0.01J$ for a lattice containing $N = 1000$ sites.

In general, a reasonable minimum condition for experimentally accessing the weak-force regime, and in particular for observing qubit revivals, is $\Gamma T_B \gtrsim 10$. Using Eqs. (2.75), (2.80), and (3.5), this condition yields $F \lesssim 0.6g^2/J$ and $\xi \gtrsim 10J^2/(\pi g^2)$. In addition, the number of cavities should satisfy $N \gtrsim 2\xi$. It is worth noting that this requirement is sufficient to observe the effects discussed in this chapter in both the weak- and strong-force limits. For a representative coupling strength $g = 0.2J$, we obtain $F \lesssim 0.025J$ and $N \gtrsim 160$, while for $g = 0.4J$ we find $F \lesssim 0.1J$ and $N \gtrsim 40$; both parameter sets lie within the weak-force regime. In contrast, as shown in Fig. 3.2, only a small number of cavities is required to observe the characteristic dynamics in the strong-force regime. For example, choosing $g = 0.01J$ and $F = 0.5J$ yields $\xi = 4$, implying that only $N \gtrsim 8$ cavities are needed. These requirements appear to be within reach of current experimental capabilities, given recent advances in the fabrication of long coupled-cavity arrays (see, e.g., Ref. [94]).

3.5 Conclusions

In summary, in this chapter we have investigated the decay of a qubit into a photonic lattice where emitted photons are accelerated by a synthetic force. Despite the qubit being weakly coupled to the array, the force drives the emitted photon along the band until hitting one of the two band edges. Somewhat similarly to a mirror, despite the absence of actual mirrors in the system, this causes an inversion of motion enforcing the emitted photon to return to the qubit where, depending on interference conditions, it can be generally reabsorbed. The non-Markovian dynamics seeded by this novel feedback mechanism is rich and generally involved. Here, we provided a first characterization by identifying in particular two regimes corresponding to strong and weak values of the synthetic force. In the former case, we showed that vacuum Rabi oscillations can occur with the qubit periodically exchanging energy with a field eigenmode spread over many cavities of the array. These can lie either to the right or left of the qubit, meaning that chiral reversible emission occurs whose chirality can be controlled by tuning the qubit frequency. For weak force, the qubit instead exhibits a complex non-Markovian decay with revivals where each emitted wavepacket undergoes a round trip before returning to the qubit. When the qubit is tuned to the band center, we proved that such dynamics is described by a delay differential equation formally analogous to the one describing the decay of an atom into a multi-mode standard cavity.

The present study links a very distinctive and longstanding effect of having a band structure (Bloch oscillations) with non-Markovian dynamics in a 1D wavevuide. It is remarkable that the usual in-band exponential decay occurring for weak coupling and no applied force does not show up any direct sign of the presence of photonic band edges. In contrast, turning on even a weak force makes the qubit aware that the field lives in a finite-size band, which deeply affects its dynamics. This occurs because the emitted photon is accelerated by the synthetic force; as such, its energy and momentum are no longer constant during the evolution. Such kind of dynamics is to our knowledge unprecedented in waveguide QED and thus has the potential to introduce a new paradigm of atom-photon interactions, including implementations of quantum information processing tasks.

We note that Bloch oscillations can be viewed as a sort of dynamical Bragg diffraction with the points $k = \pm\pi$ in the momentum space acting as effective Bragg planes (see e.g. Refs. [95, 96]). An explicit connection between the effects predicted in this chapter and Bragg diffraction is therefore an interesting direction for future research, especially in light of the fact that this concept has proven useful in the study of light–matter interaction in free space (see e.g. Ref. [97]).

The one-qubit model considered in this chapter can be naturally extended in various ways. For instance, by introducing a uniform but time-dependent force, the fictitious Newtonian dynamics (see Section 2.7.1) would still apply, with F now being time-dependent. If this force is oscillatory, one could then take advantage of Floquet theory. This represents a promising direction for future research, especially given that light-matter interactions in Floquet photonic lattices are currently the subject of active investigation [98]. Another straightforward generalization involves considering a multi-band array (see, e.g., Refs. [14, 94]), which would leave Newton's equation unaffected, but with the photon now generally able to undergo inter-band transitions.

Somewhat in line with several papers investigating non-Markovian decay with time delays in standard waveguides (see e.g. Refs. [23, 44–46]), in this chapter we focused on emission properties of a single qubit, which was shown to be an already quite involved dynamics. The extension to many qubits is an interesting outlook, for instance in order to devise novel entanglement generation schemes, but demands introducing extra degrees of freedom and an additional characteristic length (the distance between the qubits) into the problem; as such, it goes beyond the scope of this thesis and will be the subject of future investigations.

Chapter 4

Chiral emission of valley-polarized light from a giant atom

In condensed-matter physics, *valleytronics* exploits the valley index of Bloch bands as an information carrier, analogous to spin in spintronics. In graphene and transition-metal dichalcogenides, inequivalent extrema at K and K' define a valley degree of freedom [99, 100]; when inversion symmetry is broken, they acquire opposite Berry curvature and orbital magnetic moment, enabling valley-dependent transport and optical responses [99, 101], including optical valley polarization [102] and the valley Hall effect [99, 103].

An analogous valley-Hall mechanism exists in photonics: in engineered photonic crystals, inversion-symmetry breaking opens a topological band gap at the inequivalent K and K' valleys, which carry opposite valley character [104, 105]. This enables robust valley-selective transport through valley-Hall edge states, kink modes, and pseudospin–valley-coupled propagation [106–108]. Recent works have coupled quantum emitters to such valley-polarized edge modes [109–112], typically exploiting the correlation between valley character and local optical spin/helicity. This allows spin-selective coupling to opposite propagation channels, often using a V-type emitter with two circularly polarized transitions. Such schemes are appealing for quantum information processing, as they provide disorder-robust chiral single-photon emission [113, 114].

In platforms such as circuit QED [115, 116], however, photons do not naturally provide a readily usable polarization degree of freedom. A different mechanism is therefore needed to selectively couple a quantum emitter to a given photonic valley.

In this chapter, we show that this task can be accomplished by using so-called *giant atoms* [117] (introduced in Section 2.8 of Chapter 2). These have emerged in the last few years as a new paradigm in quantum optics, since they overcome the conventional description of an atom as a pointlike quantum emitter inherent in the electric-dipole approximation. In contrast to a small atom, a giant atom couples to the field at multiple discrete points, giving rise to a nonlocal light–matter interaction and, consequently, to a variety of distinctive phenomena [30, 58, 118–120]. Experimentally, giant atoms were first realized in circuit-QED platforms as superconducting qubits coupled to one-dimensional waveguides supporting either phonons or microwave photons [36, 57, 121], and, more recently, using a ferromagnetic spin ensemble coupled to a meandering waveguide [122]. Alternative implementations based on ultracold atoms and Rydberg atoms in photonic-crystal waveguides have been proposed [123, 124]. In addition, the coupling at different points can be engineered to be complex and phase tunable, as recently demonstrated experimentally [125]. Very recently, giant-atom emission into an array of coupled resonators realizing the SSH model [126] was experimentally demonstrated in a circuit-QED setup by coupling a transmon qubit simultaneously to multiple resonators [33].

A key property of giant atoms is their ability to enable *selective coupling* to photonic modes; for example, in a waveguide they can be engineered to couple to right-propagating modes while suppressing coupling to left-propagating ones [125, 127, 128]. We exploit this nonlocal interference mechanism in a honeycomb photonic lattice [129–132] to couple a giant atom to one valley while suppressing emission into the other. This valley selectivity imprints the Berry curvature of the selected valley onto the emitted photon. When a spatially varying sublattice detuning creates a topological domain wall, the same mechanism yields chiral single-photon emission along the interface.

Within the broad framework of waveguide QED [1, 3], and especially of circuit-QED arrays of coupled resonators interacting with qubits [8, 9, 13, 14, 72, 73, 133–135], chiral emission from a quantum emitter locally coupled to a topological lattice has recently been explored experimentally in a circuit-QED implementation on a 5×5 lattice [134], as well as theoretically [79, 136]. In all these cases, however, time-reversal symmetry is broken throughout the entire lattice, an experimentally demanding requirement for large systems. By contrast, our scheme achieves chiral emission while preserving time-reversal symmetry in the two-dimensional photonic lattice. The required symmetry breaking is confined to the light–matter coupling Hamiltonian and can be implemented with only two coupling points, one of which has a complex coupling amplitude.

The present chapter is organized as follows. We begin in Section 4.1 by introducing the model since the spectral and topological properties of the inversion-symmetry-broken honeycomb lattice were reviewed in Section 2.9.2. In Section 4.2, we show how the non-local coupling of a giant atom can be engineered to achieve selective coupling to a single valley. Section 4.3 demonstrates that this mechanism yields valley-polarized spontaneous emission in the bulk. We then review in Section 4.4 the valley-polarized edge modes supported by a topological domain wall. In Section 4.5, we show that the giant atom can be made to couple only to the edge modes of a single valley, resulting in chiral single-photon emission along the domain wall. Finally, in Section 4.7, we summarize our results and discuss possible future directions.

4.1 Model and Hamiltonian

In this section, we revisit the honeycomb lattice introduced in Section 2.9.2. Since its main properties have already been discussed there, we assume familiarity with the lattice structure and its corresponding photonic Hamiltonian. We consider a qubit with transition frequency ω_0 that is *non-locally* coupled to the photonic lattice under the rotating-wave approximation (see Fig. 4.1). Using Eq. (2.132), the total Hamiltonian can be written as

$$H = H_B + \omega_0 \sigma_+ \sigma_- + H_{\text{int}} \tag{4.1}$$

with the atom-field coupling Hamiltonian given by

$$H_{\text{int}} = \frac{g}{\sqrt{\mathcal{N}}} \sum_{\ell=1}^{\mathcal{N}} \left(e^{i\phi_\ell} a^\dagger_{\mathbf{R}_\ell} \sigma_- + \text{H. c.} \right), \tag{4.2}$$

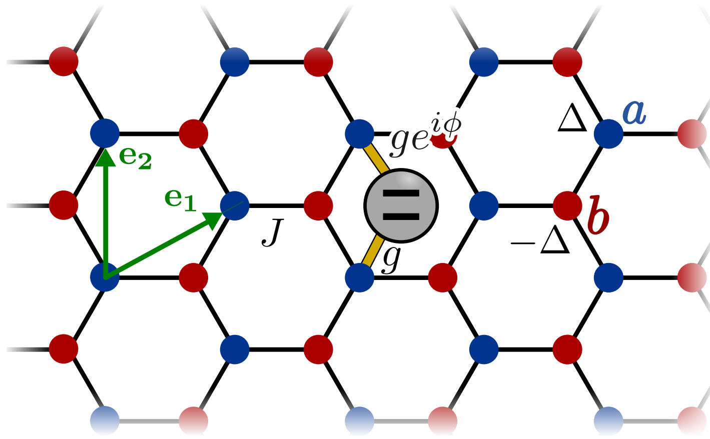

Figure 4.1: Sketch of the setup: a two-level giant atom is coupled to a photonic honeycomb lattice of resonators (blue and red dots). In this instance, the giant atom is coupled at two points, with coupling strengths g and $ge^{i\phi}$, respectively. The bare lattice does not break time reversal symmetry, it breaks inversion symmetry due to sublattice detuning measured by Δ.

while $a_{\mathbf{R}_\ell}$ annihilates an excitation in the a-sublattice resonator located at position $\mathbf{R}_\ell$, with $\ell = 1, \ldots, \mathcal{N}$. Each of these resonators is coupled to the qubit with strength $g_\ell = (g/\sqrt{\mathcal{N}})e^{i\phi_\ell}$, where $g/\sqrt{\mathcal{N}}$ is the common coupling modulus and ϕ_ℓ is the corresponding phase. In the following, we refer to these resonators as "coupling points" and to the qubit as a "giant atom". Notice that the coupling strengths g_ℓ are, in general, complex and may therefore break time-reversal symmetry. In Eq. (4.1) and throughout the remainder of this chapter, we assume identical coupling magnitudes at all coupling points and restrict the giant atom to couple only to the a-resonators, which is sufficient for our purposes.

4.2 Selective coupling to a single valley

We are now interested in studying how a giant atom couples to the normal modes of the photonic honeycomb lattice. To this aim, we invert Eqs. (2.134) and (2.141) in order to express in terms of normal modes the real-space field operators appearing in the interaction Hamiltonian (4.2). This yields

$$H_{\text{int}} = \sum_{\mathbf{k}} (g_{\mathbf{k}}^{+}\, \alpha_{\mathbf{k}}^{\dagger} + g_{\mathbf{k}}^{-}\, \beta_{\mathbf{k}}^{\dagger})\sigma + \text{H.c.}\,, \tag{4.3}$$

with the mode coupling functions for the upper and lower bands respectively given by

$$\begin{aligned} g_{\mathbf{k}}^{+} &= \frac{g}{\sqrt{N\mathcal{N}}} \sum_{\ell=1}^{\mathcal{N}} e^{i\phi_\ell} e^{-i\mathbf{k}\cdot\mathbf{R}_\ell} \cos\frac{\theta_{\mathbf{k}}}{2}\,, \\ g_{\mathbf{k}}^{-} &= -\frac{g}{\sqrt{N\mathcal{N}}} \sum_{\ell=1}^{\mathcal{N}} e^{i\phi_\ell} e^{-i\mathbf{k}\cdot\mathbf{R}_\ell} e^{i\varphi_{\mathbf{k}}} \sin\frac{\theta_{\mathbf{k}}}{2}\,. \end{aligned} \tag{4.4}$$

In valley τ, namely for $\mathbf{k} = \mathbf{K}_\tau + \mathbf{q}$ with $|\mathbf{q}| \ll |\mathbf{K}|$ [recall that τ=1 (τ=−1) corresponds to $\mathbf{K}$ ($\mathbf{K}'$), with $\mathbf{K}' = -\mathbf{K}$], we have that for $\Delta > 0$

$$g^{+}_{\mathbf{K}_\tau+\mathbf{q}} \simeq \frac{g}{\sqrt{N\mathcal{N}}}\sum_{\ell=1}^{\mathcal{N}} e^{i[\phi_\ell-(\tau\mathbf{K}+\mathbf{q})\cdot\mathbf{R}_\ell]}, \;\; g^{-}_{\mathbf{K}_\tau+\mathbf{q}} \simeq 0\,, \tag{4.5}$$

while for $\Delta < 0$

$$g^{+}_{\mathbf{K}_\tau+\mathbf{q}} \simeq 0, \;\; g^{-}_{\mathbf{K}_\tau+\mathbf{q}} \simeq -\frac{g\, e^{i\varphi_{\tau,\mathbf{q}}}}{\sqrt{N\mathcal{N}}}\sum_{\ell=1}^{\mathcal{N}} e^{i[\phi_\ell-(\tau\mathbf{K}+\mathbf{q})\cdot\mathbf{R}_\ell]}\,. \tag{4.6}$$

where $e^{i\varphi_{\tau,\mathbf{q}}}=(\tau q_x - iq_y)/q$. Therefore, the giant atom couples predominantly to the upper (lower) band for $\Delta > 0$ ($\Delta < 0$). In either case, we see that the coupling to the valleys is governed by the same structure factor

$$F_\tau(\mathbf{q}) = \sum_{\ell=1}^{\mathcal{N}} e^{i[\phi_\ell-(\tau\mathbf{K}+\mathbf{q})\cdot\mathbf{R}_\ell]}\,. \tag{4.7}$$

Now, since selective coupling to valley τ implies decoupling from the other, it is convenient to derive first the condition to decouple from a generic valley τ.

Decoupling condition from valley τ

Based on (4.5) and (4.6), the condition to decouple from the whole valley τ reads $F_\tau(\mathbf{q}) \simeq 0$, that is

$$\sum_{\ell=1}^{\mathcal{N}} e^{i[\phi_\ell-(\tau\mathbf{K}+\mathbf{q})\cdot(\mathbf{R}_\ell-\mathbf{R}_1)]} \simeq 0 \tag{4.8}$$

for any $\mathbf{q}$ such that $q \ll 1/a$.

In particular, this condition must hold for $\mathbf{q} = 0$, corresponding to the valley center, which yields

$$\sum_{\ell=1}^{\mathcal{N}} e^{i[\phi_\ell-\tau\mathbf{K}\cdot(\mathbf{R}_\ell-\mathbf{R}_1)]} = 0\,. \tag{4.9}$$

Arranging Eq. (4.8) in the form

$$\sum_{\ell=1}^{\mathcal{N}} e^{i[\phi_\ell-\tau\mathbf{K}\cdot(\mathbf{R}_\ell-\mathbf{R}_1)]}\, e^{-i\mathbf{q}\cdot(\mathbf{R}_\ell-\mathbf{R}_1)} = 0 \tag{4.10}$$

we find that (approximate) decoupling from the entire valley occurs when (4.9) holds together with $q\,|\mathbf{R}_\ell - \mathbf{R}_1| \ll 1$ for all coupling points and all momenta $\mathbf{q}$ in the considered valley. Since $q \ll 1/a$ within the valley, the latter condition corresponds to $|\mathbf{R}_\ell - \mathbf{R}_1| \sim a$.

Selective coupling condition

Based on the above, we conclude that the conditions for the giant atom to couple selectively only to valley τ are thus

$$\sum_{\ell=1}^{\mathcal{N}} z_\ell(\tau) \neq 0, \quad \sum_{\ell=1}^{\mathcal{N}} z_\ell(-\tau) = 0, \quad |\mathbf{R}_\ell - \mathbf{R}_1| \sim a\,, \tag{4.11}$$

where for each coupling point we have defined the τ-dependent phasor

$$z_\ell(\tau) = e^{i[\phi_\ell - \tau \mathbf{K}\cdot(\mathbf{R}_\ell - \mathbf{R}_1)]}\,. \tag{4.12}$$

Geometrically, the second condition requires the $\mathcal{N}$ phasors $z_\ell(-\tau)$ to form a closed polygon in the complex plane, thereby ensuring decoupling from valley $-\tau$, whereas the corresponding polygon for valley τ must remain open (first condition), so that the coupling to that valley is nonzero. Finally, the third condition requires that the giant-atom size must be comparable to the unit-cell scale.

Notably, conditions (4.11) evidently cannot be satisfied by any normal atom (i.e., in the case $\mathcal{N} = 1$), while they can be fulfilled by a giant atom ($\mathcal{N} \geq 2$).

In particular, for *two coupling points*, the decoupling condition from valley $-\tau$ reduces to

$$1 + e^{i[\phi + \tau \mathbf{K}\cdot(\mathbf{R}_2 - \mathbf{R}_1)]} = 0, \tag{4.13}$$

where we set $\phi = \phi_2 - \phi_1$. Hence

$$\phi = \left[1 - \frac{2\tau}{3}(\Delta n - \Delta m)\right]\pi \pmod{2\pi} \tag{4.14}$$

with $\Delta n = n_2 - n_1$ and $\Delta m = m_2 - m_1$, where $\mathbf{R}_\ell = n_\ell \mathbf{e}_1 + m_\ell \mathbf{e}_2$. It is easy to see that this also guarantees the first condition, namely a nonzero coupling to valley τ, unless $\Delta n - \Delta m$ is an integer multiple of 3. This possibility, however, is ruled out by the third condition in Eq. (4.11).

In particular, the condition can always be satisfied when the giant atom is coupled to a pair of a-resonators in nearest-neighbour cells (as in Fig. 4.1) since in this case either $\Delta n = \pm 1$, $\Delta m = 0$ or $\Delta n = 0$, $\Delta m = \pm 1$. In these cases, therefore, condition (4.11) yields either $\phi = \pi/3$ or $\phi = -\pi/3$ (up to a multiple integer of 2π). In particular, in the instance of Fig. 4.1 the coupling points are such that $\mathbf{R}_2 - \mathbf{R}_1 = \mathbf{e}_2$ hence $\Delta n = 0$, $\Delta m = 1$, implying that the giant atom couples only to valley K (K') for $\phi = \pi/3$ ($\phi = -\pi/3$).

Weak-coupling regime

It is worth noting that, in general, although the above conditions ensure coupling to only one valley, the giant atom may still couple to high-frequency lattice modes outside the two valleys. This possibility is, however, suppressed provided that such modes are far detuned from the emitter, which occurs when $\omega_0 \approx 0$ is tuned near the band center, corresponding to the low-energy modes in proximity of the Dirac points, and the coupling strength is much smaller than the hopping rate $g \ll J$. This condition is completely consistent also with the previous decoupling condition from the $-\tau$ valley. Indeed, by considering Eq. (2.147), we require that the coupling is not larger

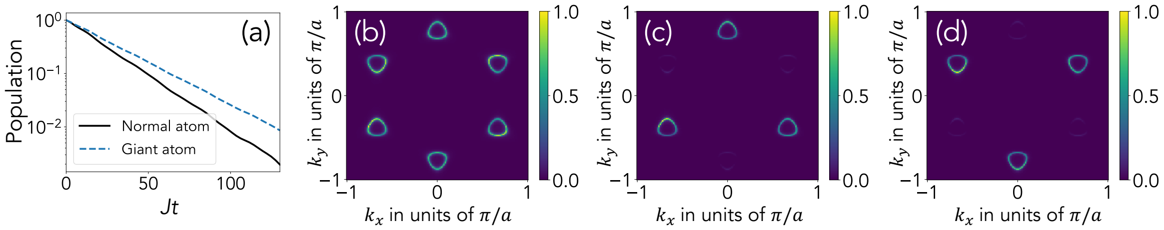

Figure 4.2: Homogeneous lattice: spontaneous emission of a normal and a giant atom for $\Delta = 0.5J$, $\omega_0 = 0.7J$. The normal atom is coupled to resonator a_{00} with strength $g = 0.18J$, while the giant atom is coupled to a_{00} and a_{01} with strengths $g/\sqrt{2}$ and $g/\sqrt{2}\, e^{i\phi}$, respectively. (a) Emitter's excited-state population $|\epsilon|^2$ versus time (in units of J) for the normal atom (black solid line) and the giant atom for $\phi = \pm\pi/3$ (blue dashed). (b) Momentum-space photon density $\rho(\mathbf{k}) = |\epsilon_{\alpha\mathbf{k}}|^2 + |\epsilon_{\beta\mathbf{k}}|^2$ of the field emitted from the normal atom. (c) Same as (b), but for the giant atom with $\phi = \pi/3$. (d) Same as (c), but for $\phi = -\pi/3$. In (b)-(d), the photon density is computed at the time when $|\epsilon|^2 = 1\%$ and rescaled to its maximum value. All plots are obtained from numerical simulations of a lattice of 331×331 unit cells.

than the maximum energy consistent with the Dirac Hamiltonian approximation, i.e. $g \ll v\, q_{\max}$, for a wavevector $0 < q_{\max} < \pi/a$. From Eq. (2.146), as an upper bound, we immediately get $g/J \ll 3/2$. In the following, we will always consider this weak-coupling regime.

4.3 Spontaneous emission of valley-polarized photons

To assess the effectiveness of selective coupling to a single valley, we compare the spontaneous emission of a normal and a giant atom in the bulk of a homogeneous honeycomb lattice according to Hamiltonian (4.1) (we will consider a non-homogeneous lattice later on). The joint state at time t lies in the single-excitation sector and has the form

$$|\Psi(t)\rangle = \epsilon(t)\,|e\rangle + \sum_{\mathbf{k}} \epsilon_{\alpha\mathbf{k}}(t)\, |\alpha_{\mathbf{k}}\rangle + \sum_{\mathbf{k}} \epsilon_{\beta\mathbf{k}}(t)\,|\beta_{\mathbf{k}}\rangle\,, \tag{4.15}$$

where $|e\rangle$ is the state where the emitter is in the excited state and the field in the vacuum state $|\mathrm{vac}\rangle$, while $|\alpha_{\mathbf{k}}\rangle = |g\rangle\, \alpha^\dagger_{\mathbf{k}}\,|\mathrm{vac}\rangle$ and $|\beta_{\mathbf{k}}\rangle = |g\rangle\, \beta^\dagger_{\mathbf{k}}\,|\mathrm{vac}\rangle$. The initial condition is $\epsilon(0) = 1$, $\alpha_{\mathbf{k}}(0) = \beta_{\mathbf{k}}(0) = 0$. Replacing (4.15) into the Schrödinger equation $\frac{d}{dt}\,|\Psi(t)\rangle = -iH\,|\Psi(t)\rangle$ leads to a linear first-order differential system in the $2N + 1$ unknown functions $\epsilon(t)$, $\alpha_{\mathbf{k}}(t)$ and $\beta_{\mathbf{k}}(t)$, which can be easily solved.

We consider first a normal atom coupled to resonator a_{00} with strength g and then a giant atom coupled to a_{00} and a_{01} with strengths $g/\sqrt{2}$ and $g/\sqrt{2}\,e^{i\phi}$, respectively [cf. Eq. (4.2)]. In either case, we set $\Delta > 0$, $\omega_0 > \Delta$ and g small compared to $\omega_0 - \Delta$ corresponding to an emitter weakly coupled to the upper photonic band and far-detuned from the lower band (hence the latter is negligibly populated) [1]. The resulting emission dynamics is displayed in Fig. 4.2. As expected, both the normal and giant atoms undergo a standard exponential decay although with different rates [see Fig. 4.2(a)]. In momentum space, the field emitted from the normal atom [see Fig. 4.2(b)] is uniformly

[1]Setting a non-zero Δ is not necessary for the essential qualitative results of the present section, which would hold even for $\Delta = 0$ provided that ω_0 is sufficiently far from the Dirac points.

distributed along thin contours around the points $\mathbf{K}$ and $\mathbf{K}'$ (as well as the remaining four vertices of the first Brillouin zone, which are equivalent to $\mathbf{K}$ or $\mathbf{K}'$). Remarkably, the contour around the point $\mathbf{K}'$ (as well as those around the two equivalent points) vanishes for the field emitted by the giant atom when $\phi = \pi/3$ [see Fig. 4.2(c)]. Setting instead $\phi = -\pi/3$ conversely suppresses the contour around the point $\mathbf{K}$ [see Fig. 4.2(d)].

The behavior of the emitted field in panels (c) and (d) confirms the validity of the condition for selective coupling to a specific valley derived in the previous section. This shows that a giant atom with suitably engineered coupling points (even just two) can emit valley-polarized light.

It is worth noting that, as is well known, while being preserved globally, time-reversal symmetry is broken within *each* valley. This is consistent with the condition (4.14) implying that valley-polarized emission requires the atom–field coupling Hamiltonian (4.2) to break time-reversal symmetry.

4.4 Valley-polarized edge modes

As discussed in Section 2.9.5, breaking inversion symmetry through a non-zero detuning Δ between sublattice frequencies endows each valley with a nontrivial topology, as signaled by a nonzero Berry curvature whose sign is controlled by Δ [cf. Eq. (2.148)]. A remarkable consequence of this valley topology is that, when two lattice domains with opposite sublattice detuning ($\Delta = \pm\Delta_0$) are engineered, within each valley a topological phase transition occurs across the interface. As a result, a band of gapless, *valley-polarized edge modes* emerges along the domain wall [137, 138]. In the present section, we review the properties of these edge modes.

In the presence of a spatially-varying detuning Δ, the lattice Hamiltonian (2.132) becomes

$$H_B = \sum_{\mathbf{R}} \Delta(\mathbf{R})(a^\dagger_{\mathbf{R}} a_{\mathbf{R}} - b^\dagger_{\mathbf{R}} b_{\mathbf{R}}) + J \sum_{\langle \mathbf{R},\mathbf{R}'\rangle} (a^\dagger_{\mathbf{R}} b_{\mathbf{R}'} + \mathrm{H.\,c.}) \,, \tag{4.16}$$

where $\Delta(\mathbf{R})$ changes sign upon crossing a domain wall. A standard and convenient way to model $\Delta(\mathbf{R})$ so as to ensure a smooth spatial sign change across the domain wall is

$$\Delta(\mathbf{R}) = \Delta_0 \tanh\left(\frac{\mathbf{R}\cdot\hat{\mathbf{v}}}{\lambda}\right) , \tag{4.17}$$

which interpolates between $\pm\Delta_0$ over a length scale λ, where $\hat{\mathbf{v}}$ identifies the gradient direction. We assume $\lambda \gg a$, such that the detuning varies slowly on the scale of the lattice spacing.

In the following, we set $\hat{\mathbf{v}} = \hat{\mathbf{x}}$, so that the domain wall is centered at $x = 0$ and extends along the y direction; the results, however, are naturally generalized to an arbitrary $\hat{\mathbf{v}}$.

4.4.1 Edge modes

In Fig. 4.3, we show the results of numerically diagonalizing (4.16) after Fourier transformation along the y direction. As expected, two band dispersions with opposite slopes arise within the gap $|\omega| \le \Delta_0$ around the K' and K points, respectively [see Fig. 4.3(a)]. Each in-gap band corresponds to valley-polarized edge modes propagating

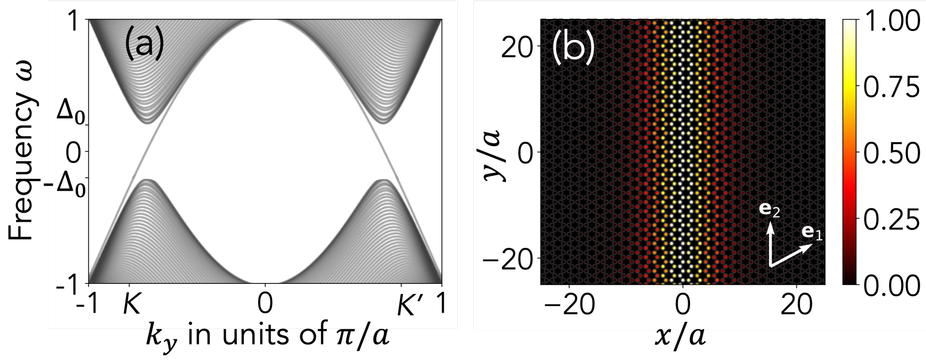

Figure 4.3: Valley-polarized edge modes under a spatially varying sublattice detuning $\Delta(x) = \Delta_0 \tanh(x/\lambda)$ for $\Delta_0 = 0.2J$, and $\lambda = 4a$. (a) Lattice dispersion along k_y (frequency is in units of J). (b) Rescaled real-space photon density of the lattice normal mode at frequency $\omega = -0.16J$ for $k_y = -0.73\pi/a$. The plots were obtained by numerical diagonalization of $H_B(k_y)$, the partial Fourier transform of (4.16) along the y axis, for k_y running over the first Brillouin zone, using a lattice of 100×100 unit cells.

along the y axis and localized across the domain wall at $x = 0$, as shown in Fig. 4.3(b) for a representative edge mode. Notably, the edge modes associated with the two valleys have opposite group velocities.

Using the standard envelope-function approximation [139] and replacing $\Delta \to \Delta(x)$ in the effective massive Dirac Hamiltonian (2.147) for each valley τ, one can derive analytical expressions for the edge modes and their spectrum near $\omega = 0$, where the dispersion is approximately linear [see Fig. 4.3(a)].

The resulting edge modes can be written in real space as single-photon Fock states

$$\left|\mathcal{E}_{\tau,q_y}\right\rangle = \sum_{\mathbf{R}} \left[\Psi_{\tau,q_y}(\mathbf{R})\, a^\dagger_{\mathbf{R}} + \Phi_{\tau,q_y}(\mathbf{R})\, b^\dagger_{\mathbf{R}}\right] |\mathrm{vac}\rangle\,, \tag{4.18}$$

with (see Appendix C.1)

$$\Psi_{\tau,q_y}(\mathbf{R}) = -i\tau\, \Phi_{\tau,q_y}(\mathbf{R}) = e^{i\tau\mathbf{K}\cdot\mathbf{R}} \frac{e^{iq_y y_{\mathbf{R}}}}{\sqrt{N_y}} \frac{\psi(x_{\mathbf{R}})}{\sqrt{2}}\,, \tag{4.19}$$

where $q_y = \nu 2\pi/L_y$ with $L_y = N_y\sqrt{3}\,a$ the system length along y [cf. Eq. (2.133)], while $x_{\mathbf{R}}$ and $y_{\mathbf{R}}$ are the Cartesian components of $\mathbf{R}$. The transverse localized wavefunction appearing in Eq. (4.19) is defined as

$$\psi(x_{\mathbf{R}}) = A \exp\left[-\frac{1}{v}\int_0^{x_{\mathbf{R}}} \Delta(x')\, dx'\right], \tag{4.20}$$

where A is fixed by the normalization of (4.18) and is explicitly given by

$$A = \left[\sum_{n=-N_x/2}^{N_x/2-1} \exp\left(-\frac{2}{v}\int_0^{\frac{3a}{2}n} \Delta(x')\, dx'\right)\right]^{-1/2}, \tag{4.21}$$

where we used $x_{\mathbf{R}} = \frac{3a}{2}n$ [see Eq. (2.133)].

The corresponding spectrum of Eq. (4.18) reads

$$\omega_\tau(q_y) = \tau v q_y \,. \tag{4.22}$$

with v given by Eq. (2.146).

Therefore, the edge modes propagate along y with group velocity $+v$ $(-v)$ in the K (K') valley and are localized along x, with an asymptotic decay $\sim e^{-|x|/\xi}$, where

$$\xi = \frac{v}{\Delta_0} \,, \tag{4.23}$$

thus setting their transverse width [we used $\Delta(x)\to\pm\Delta_0$ for $x\to\pm\infty$].

In the specific case of the detuning profile $\Delta(x) = \Delta_0 \tanh(x/\lambda)$ [cf. Eq. (4.17)], the transverse wavefunction (4.20) explicitly reads (see Appendix C.1)

$$\psi(x_{\mathbf{R}}) = \left[\frac{1}{\lambda\sqrt{\pi}} \frac{\Gamma\left(\beta+\frac{1}{2}\right)}{\Gamma(\beta)}\right]^{1/2} \cosh^{-\beta}\left(\frac{x_{\mathbf{R}}}{\lambda}\right) , \tag{4.24}$$

where $\beta = \lambda/\xi$. For large $|x_{\mathbf{R}}|$, $\psi(x_{\mathbf{R}})$ decays asymptotically as $e^{-|x_{\mathbf{R}}|/\xi}$.

4.5 Single-photon chiral emission

In the presence of $\Delta(x)$ and in the weak-coupling regime, a quantum emitter tuned within the band gap couples only to the valley-polarized edge modes, as the bulk modes are far detuned and can be neglected. In this section, we first analyze this spontaneous emission process for a normal atom and then generalize it to a giant atom.

4.5.1 Emission from a normal atom

Consider a normal atom tuned near the band gap center [cf. Eq. (4.2) for $\mathcal{N} = 1$] and coupling strength g small compared to Δ_0 [2]. Fig. 4.4(a) shows the real-space photon density of the field emitted from an atom coupled to the resonator $a_{\mathbf{R}=0}$. The emitted photon clearly propagates along the domain wall, equally in the upward and downward directions thus providing evidence that the normal atom couples with the same strength to the edge modes of both valleys. This conclusion can be quantitatively supported by explicitly calculating the decay rate into each valley, as outlined below.

Let $\rho_\tau(\mathbf{R};\omega)$ denote the local density of states of the valley-polarized edge modes

[2] We place the emitter at the center of the band gap for the sake of argument. The essential requirement is that its frequency lies within the gap and its coupling is small compared to the detuning from band edges.

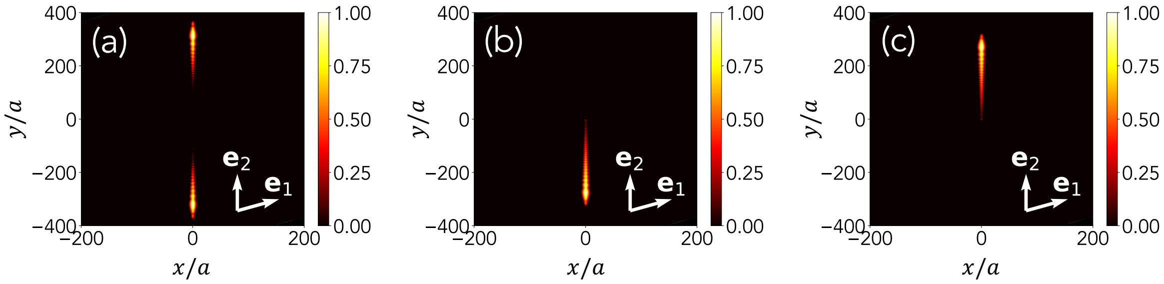

Figure 4.4: Lattice with a non-uniform sublattice detuning $\Delta(x) = \Delta_0 \tanh(x/\lambda)$: spontaneous emission of a normal and a giant atom for $\Delta_0 = 0.5J$, $\lambda = 2a$, $\omega_0 = 0$. The normal atom is coupled to resonator a_{00} (lying at the origin) with strength $g = 0.3J$, while the giant atom is coupled to a_{00} and a_{01} with strengths $g/\sqrt{2}$ and $g/\sqrt{2}\, e^{i\phi}$, respectively. (a) Log-scale rescaled real-space photon density of the field emitted from the normal atom. (b) Same as (a), but for the giant atom setting $\phi = -\pi/3$. (c) Same as (b) but for $\phi = \pi/3$. In all cases, we numerically verified that the emitter decays exponentially, with decay rates $\Gamma = \sum_\tau \Gamma_\tau = 0.03J$ in (a) and, $\tilde{\Gamma}_{+1} = 0.021J$ in (b) and $\tilde{\Gamma}_{-1} = 0.021J$ in (c), in excellent agreement with Eqs. (4.26) and (4.31). In all plots, the photon density is computed at the time when $|\epsilon|^2 = 1\%$. All plots are obtained from numerical simulations of a lattice of 551×551 unit cells.

at the a-resonator in unit cell $\mathbf{R}$. Based on Eqs. (4.19) and (4.22), this is given by

$$\begin{aligned}\rho_\tau(\mathbf{R};\omega) &= \sum_{q_y} |\Psi_{\tau,q_y}(\mathbf{R})|^2 \delta[\omega - \omega_\tau(q_y)] \\ &= \frac{1}{2N_y} \sum_{q_y} |\psi(x_\mathbf{R})|^2 \delta(\omega - \tau v q_y) \\ &\simeq \frac{1}{2N_y} \frac{L_y}{2\pi v} |\psi(x_\mathbf{R})|^2 \\ &= \frac{\sqrt{3}\, a}{4\pi v} |\psi(x_\mathbf{R})|^2 \,. \end{aligned} \tag{4.25}$$

This expression is independent of ω, owing to the linear dispersion in Eq. (4.22), and also of τ, since this appears only in the phases of the exponential factors [cf. Eq. (4.19)]. Accordingly, the decay rate into valley τ for a normal atom coupled to the a-resonator in the unit cell $\mathbf{R}$ is given by

$$\begin{aligned}\Gamma_\tau(\mathbf{R}) &= 2\pi g^2 \rho_\tau(\mathbf{R};\omega_0) \\ &= \frac{g^2}{\sqrt{3}\, J} |\psi(x_\mathbf{R})|^2 \,, \end{aligned} \tag{4.26}$$

where we used Eq. (2.146). Since the right-hand side of (4.26) is independent of τ, the normal atom decays into both valleys at equal rates with the total decay rate given by $\Gamma = \sum_\tau \Gamma_\tau$.

An explicit expression for Γ_τ can be obtained by substituting Eq. (4.24) into Eq. (4.26), which in particular allows one to predict the numerically computed decay rate in the case of Fig. 4.4(a).

4.5.2 Emission from a giant atom

We now replace the normal atom with a giant atom coupled to resonators a_{00} and a_{01} with relative phase $e^{i\phi}$ with $\phi = \phi_2 - \phi_1$. Fig. 4.4(b) shows the real-space photon density emitted by the giant atom for $\phi = -\pi/3$. While the photon still propagates along the domain wall, it now does so exclusively in the downward direction, thus demonstrating chiral emission. For $\phi = \pi/3$, as shown in Fig. 4.4(c), the propagation is instead fully upward. This shows that the giant atom selectively couples to only one band of valley-polarized edge modes, with emission into the other band being fully suppressed.

For a giant atom, the decay rate into valley τ does not depend on the standard local density of states (4.25), but is instead given by [140]

$$\tilde{\Gamma}_\tau = 2\pi g^2 \tilde{\rho}_\tau(\omega_0) \tag{4.27}$$

with $\tilde{\rho}_\tau$ an effective local density of states defined by [cf. Eq. (4.2)]

$$\tilde{\rho}_\tau(\omega) = \sum_{q_y} \frac{1}{\mathcal{N}} \left| \sum_{\ell=1}^{\mathcal{N}} e^{-i\phi_\ell} \Psi_{\tau,q_y}(\mathbf{R}_\ell) \right|^2 \delta[\omega - \omega_\tau(q_y)] \,. \tag{4.28}$$

Explicitly, using Eqs. (4.19) and Eq. (4.22)

$$\begin{aligned} \tilde{\rho}_\tau(\omega) = \frac{1}{2N_y} \sum_{q_y} \frac{1}{\mathcal{N}} & \left| \sum_{\ell=1}^{\mathcal{N}} \psi(x_{\mathbf{R}_\ell}) e^{i\left(\tau \mathbf{K}\cdot\mathbf{R}_\ell + q_y y_{\mathbf{R}_\ell} - \phi_\ell\right)} \right|^2 \\ & \times \delta(\omega - \tau v q_y) \,. \end{aligned} \tag{4.29}$$

For a giant atom of size comparable with the unit cell and for $\xi \gg a$, that is $\Delta_0 \ll J$ [cf. Eqs. (2.146) and (4.23), we can approximate $\psi(x_{\mathbf{R}_\ell}) \simeq \psi(x_{\mathbf{R}_1})$ and $q_y(y_{\mathbf{R}_\ell} - y_{\mathbf{R}_1}) \simeq 0$, hence

$$\tilde{\rho}_\tau(\omega) \simeq \frac{\sqrt{3}\,a}{4\pi v} |\psi(x_{\mathbf{R}_1})|^2 \frac{1}{\mathcal{N}} \left| \sum_{\ell=1}^{\mathcal{N}} e^{i(\tau \mathbf{K}\cdot\mathbf{R}_\ell - \phi_\ell)} \right|^2 \,. \tag{4.30}$$

Replacing in Eq. (4.27) and recalling Eq. (2.146), we thus end up with

$$\tilde{\Gamma}_\tau = \frac{1}{\mathcal{N}} \left| \sum_{\ell=1}^{\mathcal{N}} e^{i(\tau \mathbf{K}\cdot\mathbf{R}_\ell - \phi_\ell)} \right|^2 \Gamma_\tau(\mathbf{R}_1) \,, \tag{4.31}$$

with $\Gamma_\tau(\mathbf{R}_1)$ the decay rate of a normal atom coupled to resonator $a_{\mathbf{R}_1}$ [cf. Eq. (4.26)]. This vanishes precisely when Eq. (4.9), namely the decoupling condition from valley τ, holds. Therefore, when the giant atom decouples from valley τ, it cannot emit into the corresponding valley-polarized edge-mode band. This result, combined with Section 4.2, shows that in the present system chiral emission is achieved through selective coupling to the K or K' valley.

For two coupling points with strengths $g_1 = g/\sqrt{2}$ and $g_2 = g_1 e^{i\phi}$ as in Fig. 4.4(b)-(c), Eq. (4.31) reduces to

$$\tilde{\Gamma}_\tau = \frac{1}{2} \left| 1 + e^{i[\tau \mathbf{K}\cdot(\mathbf{R}_2 - \mathbf{R}_1) - \phi]} \right|^2 \Gamma_\tau(\mathbf{R}_1) \,, \tag{4.32}$$

which, for $\mathbf{R}_2 - \mathbf{R}_1 = \mathbf{e}_2$ and $\phi = -\pi/3$ ($\phi = \pi/3$), correctly reproduces the decay rate in Fig. 4.4(b) [(c)].

4.6 Experimental Implementations

To implement this scheme experimentally, we propose a setup analogous to that of Ref. [132] in the circuit QED platform [13, 14, 135, 141]. Typical parameters are $J/(2\pi) \sim 100-200$ MHz, $g/(2\pi) \sim 20$ MHz, and a resonator frequency $\omega_r/(2\pi) \sim 6$ GHz. The main experimental challenge lies in coupling the qubit to the bulk of the lattice, rather than to its edge. This limitation could be overcome with *flip-chip* technology [142–144], in which a second chip hosting the qubits is bonded on top of the resonator array, enabling direct coupling to bulk sites.

Our numerical simulations indicate that the effects presented in this Chapter are robust against disorder up to $\sigma_\omega/J \lesssim 0.3$, a threshold well above the disorder typical of state-of-the-art resonator fabrication, $\sigma_\omega \sim 0.5\%\,\omega_r \sim 30$ MHz [24, 94].

A minimal condition for observing the unidirectional emission concerns the system size. Along the x direction, the lattice must accommodate the decay of the wave function [see Eq. (4.24)]: requiring the amplitude to fall below 13% of its maximum yields $N_x \gtrsim 4\xi$. Along the y direction, the required size is instead set by the qubit decay rate Γ and the propagation velocity v: requiring the qubit population to drop below 13% of its initial value before the emitted photon reaches the boundary yields $N_y \gtrsim 4v/\Gamma$. As an example, for a giant atom with $\Delta_0 = J$, $\lambda = a$, and $g = 0.4J/\sqrt{2}$, this gives $N_x \gtrsim 6$ and $N_y \gtrsim 76$.

4.7 Conclusions

In this chapter, we have shown that giant atoms provide a natural and powerful route to implement *valley-selective* light–matter interactions in synthetic honeycomb photonic lattices. By exploiting the non-local character of the emitter–bath coupling, interference among different coupling points can be engineered so as to suppress the coupling to one valley while preserving it to the other, a task unachievable for a normal atom locally coupled to a single lattice resonator.

We first analyzed a homogeneous honeycomb lattice with sublattice detuning, which breaks inversion symmetry while preserving time-reversal symmetry. In this setting, we derived the condition under which a giant atom selectively couples to only one of the two inequivalent valleys, K or K'. We showed that this can already be achieved with only two coupling points, provided that their relative phase is appropriately tuned. Numerical simulations of spontaneous emission in the bulk confirmed these analytical predictions, showing that the emitted radiation becomes strongly valley polarized in momentum space. In this regime, the giant atom acts as a source of valley-polarized photons, while a normal atom populates both valleys symmetrically.

We then turned to the case of a spatially inhomogeneous sublattice detuning, generating a domain wall between two regions with opposite valley topology. As is well known, such a configuration supports edge modes associated with the two valleys, localized at the interface and counter-propagating along it. By combining this valley-polarized photonic environment with the selective valley coupling enabled by the giant atom, we demonstrated that the emitter undergoes chiral spontaneous emission: depending on the engineered relative phases between the coupling-point strengths, the photon is emitted preferentially into one propagation direction along the domain wall. In contrast, a normal atom, which couples equally to both valleys, emits the photon along the domain wall, with equal probability in the two opposite directions.

Our results therefore identify a physical mechanism through which non-local light–matter coupling promotes valley selectivity into directional quantum emission thus opening new perspectives for quantum-optical applications and phenomena based on the valley degree of freedom of photons.

Importantly, the emergence of chirality here does not rely on breaking time-reversal symmetry in the photonic bath, but only in the phase-patterned giant-atom coupling to the field. This distinguishes the present setting from chiral quantum-optical platforms based on explicitly non-reciprocal or magnetic photonic metamaterials, and makes it especially appealing for implementations in experimentally accessible architectures such as circuit QED, where realizing large photonic lattices with broken time-reversal symmetry is challenging.

More broadly, our work establishes giant atoms as a versatile tool for photonic valleytronics. Beyond the single-emitter scenario considered here, the framework developed in this chapter opens several promising directions. For instance, arrays of giant atoms selectively coupled to different valleys may give rise to direction-dependent collective decay, dissipative state preparation protocols, or effective interactions mediated by valley-polarized edge channels.

In summary, we have shown that a giant atom coupled to a photonic graphene lattice can be used to engineer selective coupling to a single valley and, in the presence of valley-polarized edge modes, to realize chiral single-photon emission without requiring time-reversal-symmetry breaking in the bath. These findings introduce a new bridge between giant-atom physics, topological quantum optics, and valleytronics, and point to a flexible strategy for designing directional quantum interfaces in synthetic photonic materials.

Chapter 5

Conclusions

In this thesis, we have investigated how synthetic potentials in photonic lattices can be used to engineer and control the emission dynamics of a quantum emitter. The central idea underlying the work is that, in modern waveguide QED, the electromagnetic environment should not be regarded as a passive background into which a qubit irreversibly decays. Rather, the photonic bath can be designed so as to possess nontrivial dispersion, finite bandwidth, synthetic forces, topology, and spatially structured normal modes. As a consequence, the spontaneous emission of a qubit becomes a sensitive probe of the engineered bath and, at the same time, a controllable dynamical process.

The results presented in this thesis fit within the broader framework of quantum optics in structured reservoirs. In standard spontaneous emission, the reservoir is assumed to be broad, smooth, and effectively memoryless around the emitter frequency. Under these conditions, the atom decays exponentially and the emitted photon escapes irreversibly into the continuum. Photonic lattices allow one to go beyond this paradigm. Their finite bands, band edges, gaps, mode profiles, and internal degrees of freedom provide mechanisms through which the emitted photon can remain partially confined, return to the emitter, acquire geometrical properties, or be directed into selected channels. In this sense, the main message of the thesis is that the geometry and synthetic structure of the bath can be promoted to active control knobs for light–matter interaction.

The first part of the thesis focused on a one-dimensional coupled-cavity array with a linear gradient of cavity frequencies. This gradient acts as an effective synthetic force on photons. In the absence of such a force, a qubit weakly coupled to the middle of the photonic band undergoes the familiar Markovian decay into propagating wavepackets. By contrast, once the synthetic force is switched on, the emitted photon is accelerated across the Brillouin zone. Because the photonic band has finite width, the photon cannot accelerate indefinitely. Instead, it undergoes Bloch oscillations: its quasi-momentum evolves periodically, and its real-space motion becomes bounded. This simple mechanism profoundly modifies the qubit dynamics. Although there are no physical mirrors in the system, the band edges act as effective turning points for the emitted photon, making it possible for the photon to return to the qubit and produce non-Markovian feedback.

A central outcome of this analysis was the identification of two regimes of light–matter interaction, controlled by the ratio between the Bloch-oscillation period and the qubit decay time. In the strong-force regime, the Wannier–Stark ladder spacing is large enough that the qubit effectively couples to a single photonic eigenstate. The dynamics then reduces to an effective Jaynes–Cummings model, but with an important difference from ordinary cavity QED: the relevant photonic mode is not a conventional cavity mode localized between two mirrors, but a Wannier–Stark eigenstate spatially centered around a lattice site determined by its frequency. As a result, the qubit can undergo vacuum Rabi oscillations with a spatially extended region of the lattice. Moreover, by tuning the qubit frequency, this region can be displaced either to the left or to the right of the qubit. This produces a form of chiral reversible emission whose directionality is controlled spectroscopically, rather than by changing the emitter position or by introducing a topological photonic bath. This chirality arises from the spatial organization of Wannier–Stark modes: different normal-mode frequencies correspond to eigenstates localized around different positions.

In the weak-force regime, the Wannier–Stark ladder becomes dense on the scale of the effective qubit–mode coupling, and the qubit interacts with many photonic modes. In this case, the initial emission resembles ordinary waveguide-QED decay only at short times. At later times, the emitted wavepackets undergo Bloch oscillations and return to the emitter after well-defined delay times, generating revivals in the qubit population. The resulting dynamics is non-Markovian and can be understood as a form of coherent feedback induced by band finiteness and synthetic acceleration. For a qubit tuned at the band center, we derived an effective delay differential equation for the excited-state amplitude. This equation is formally analogous to the one describing an atom in a multimode cavity, with the Bloch-oscillation period playing the role of a cavity round-trip time and the Bloch-oscillation amplitude playing the role of an effective cavity length. This analogy is physically useful, but it also highlights an important distinction: in the present system, confinement does not come from real-space mirrors, but from the finite Brillouin zone and from the force-driven evolution of the emitted photon.

This first set of results establishes a connection between two areas that are usually considered separately: Bloch oscillations in lattice systems and non-Markovian quantum-optical feedback. The synthetic force makes the qubit sensitive to the full finite-band structure of the photonic environment. In the absence of the force, a weakly coupled qubit tuned inside the band would mainly probe the local density of states at its transition frequency. With the force, however, the emitted photon continuously changes energy and momentum during the evolution, and therefore dynamically explores the band. This is the origin of the mirrorless feedback mechanism discussed in Chapter 3. It suggests that synthetic forces provide a flexible route to realizing delayed quantum-optical dynamics without the need for physical boundaries, long waveguides, or external reflectors.

The second part of the thesis moved from one-dimensional dynamics to two-dimensional valley photonics. There, we considered a giant atom nonlocally coupled to a honeycomb lattice of resonators with detuned sublattice frequencies. The sublattice detuning breaks inversion symmetry while preserving time-reversal symmetry, opening a gap at the Dirac points and endowing the two valleys with opposite Berry curvature. In ordinary photonic valley-Hall systems, valley-selective coupling often relies on local polarization or spin-helicity structure. This route is not naturally available in circuit-QED resonator arrays, where microwave photons do not generally carry an easily exploitable polarization degree of freedom. The thesis showed that giant atoms provide an alternative mechanism: the interference between multiple spatially separated coupling points can be engineered so that the emitter couples to one valley while decoupling from the other.

We derived the valley-selective coupling condition in terms of the phases and positions of the giant-atom coupling points. In particular, we showed that a giant atom with only two coupling points can already suppress emission into one valley, provided that the relative phase between the couplings is properly chosen. This is impossible for a normal atom locally coupled to a single resonator. The result demonstrates that nonlocal coupling geometry can act as a momentum-space filter. Numerical simulations confirmed the analytical prediction: whereas a normal atom emits symmetrically into both valleys, a suitably designed giant atom emits a strongly valley-polarized photon in momentum space.

The same mechanism was then applied to a honeycomb lattice with a spatially varying sublattice detuning. When the detuning changes sign across a domain wall, the valley topology changes across the interface and gives rise to valley-polarized edge modes. The two valleys support counter-propagating edge channels along the domain wall. A normal atom placed near the interface couples to both valleys and therefore emits symmetrically in the two opposite directions. A giant atom, instead, can be engineered to couple only to one valley and hence only to one propagation direction. This produces chiral single-photon emission along the domain wall.

A key feature of this proposal is that chirality is achieved without breaking time-reversal symmetry in the photonic bath. The honeycomb lattice itself remains reciprocal; the required phase structure is confined to the light–matter coupling Hamiltonian. This distinction is important from both conceptual and practical perspectives. Conceptually, it shows that directional quantum emission does not necessarily require a globally nonreciprocal photonic environment. Practically, it makes the scheme attractive for circuit-QED implementations, where engineering large two-dimensional lattices with broken time-reversal symmetry is challenging, whereas complex and phase-tunable coupling amplitudes are comparatively more accessible.

Taken together, the two main results of the thesis show two complementary ways in which synthetic structure controls qubit emission. In the one-dimensional system, a synthetic force reshapes the temporal structure of emission by producing Bloch-oscillation-induced feedback. In the two-dimensional system, sublattice detuning and nonlocal giant-atom coupling reshape the momentum and topological structure of emission by selecting a valley and, near a domain wall, a propagation direction. In both cases, the emitter dynamics is not determined solely by the bare coupling strength or by the local density of states, but by the interplay between the emitter and the global structure of the photonic bath.

This thesis therefore contributes to the broader program of reservoir engineering in waveguide QED. It shows that photonic lattices are not merely convenient discretizations of waveguides, but platforms in which new mechanisms of light–matter interaction can be designed from band structure, synthetic potentials, and coupling geometry. The results also emphasize the usefulness of the single-excitation sector as a theoretical setting in which complex emission phenomena can be understood analytically and numerically. Within this sector, the qubit amplitude encodes the non-Markovian memory kernel of the bath, while the emitted photon wavefunction gives direct access to the real-space and momentum-space structure of the emission process.

Several directions naturally follow from this work. For the one-dimensional force-gradient lattice, an important extension would be the study of time-dependent synthetic forces. Since the photon dynamics under a uniform force admits a Newtonian interpretation in quasi-momentum space, a periodically driven force could allow one to combine Bloch oscillations with Floquet engineering. This may lead to tunable feedback times, dynamically controlled revivals, and new regimes of photon-mediated interactions. A second extension would be the inclusion of multiband photonic lattices, where the accelerated photon could undergo interband transitions. This would enrich the feedback mechanism by combining Bloch oscillations with Landau–Zener processes and could provide a route toward controllable emission into multiple bands.

Another important direction is the many-emitter problem. In the present thesis, the non-Markovian dynamics induced by Bloch oscillations was analyzed for a single qubit. Adding more emitters would introduce an additional length scale, namely the emitter separation, and would allow one to explore photon-mediated interactions in a force-driven lattice. Since the emitted photon can return after a controllable time, such a system may support delayed collective decay, non-Markovian entanglement generation, and interaction protocols controlled by the synthetic force. The interplay between Bloch-oscillation return times and emitter separations could lead to regimes with no direct analogue in standard waveguide QED.

For the valley-photonic giant-atom setup, one natural continuation is the study of arrays of giant atoms coupled to the same domain-wall modes. Since each giant atom can be designed to select a valley, arrays of such emitters could realize direction-dependent collective decay, cascaded interactions, or dissipative state-preparation schemes mediated by valley-polarized edge channels. Another direction is to explore more general coupling geometries, involving more than two coupling points, which could allow sharper momentum-space filtering or simultaneous coupling to selected regions of the Brillouin zone. It would also be interesting to investigate the robustness of the valley-selective mechanism against disorder in the coupling phases, emitter positions, and lattice parameters.

From an experimental point of view, the results are naturally connected to circuit-QED lattices, where resonator frequencies, hopping amplitudes, qubit frequencies, and coupling phases can be engineered with high flexibility. In the one-dimensional setting, a frequency gradient across a coupled-resonator array directly realizes the synthetic force. In the two-dimensional setting, honeycomb resonator lattices with sublattice detuning and phase-controlled giant-atom couplings provide a plausible route to valley-selective chiral emission. More broadly, both proposals exploit ingredients that are compatible with ongoing developments in superconducting quantum circuits and synthetic photonic materials.

In conclusion, this thesis has shown that synthetic potentials and engineered coupling geometries provide powerful tools for controlling quantum emission in photonic lattices. A linear frequency gradient can transform ordinary spontaneous emission into mirrorless non-Markovian feedback governed by Bloch oscillations. A phase-patterned giant atom coupled to a detuned honeycomb lattice can transform valley topology into directional single-photon emission without requiring time-reversal-symmetry breaking in the bath. These results connect waveguide QED with Bloch-oscillation physics, giant-atom quantum optics, and photonic valleytronics, and point toward new strategies for designing quantum interfaces in structured electromagnetic environments.

Appendix A

The Laplace Transform

Integral transforms are very useful tools for dealing with functions and differential equations. In particular, throughout this thesis we make use of the Laplace transform. This transformation is defined as follows: let $f(t)$ be a single-variable function, and let $F(s)$ be the representation of f in the Laplace domain. In other words,

$$\mathcal{L}\left\{f(t)\right\}(s) = F(s) = \int_0^\infty dt\, f(t)e^{-st}. \tag{A.1}$$

The study of Laplace transforms is extensively covered in textbooks [145–147]; therefore, we do not discuss the subject in detail in this thesis. Instead, we focus only on some specific transformations and properties, which are summarized below:

$$\mathcal{L}\left\{af(t) + bg(t)\right\}(s) = aF(s) + bG(s) \qquad \text{(linearity)} \tag{A.2}$$

$$\mathcal{L}\left\{\int_0^t d\tau\, f(\tau)g(t-\tau)\right\}(s) = F(s)G(s) \qquad \text{(convolution)} \tag{A.3}$$

$$\mathcal{L}\left\{\frac{d}{dt}f(t)\right\}(s) = sF(s) - f(0) \qquad \text{(derivative)} \tag{A.4}$$

$$\mathcal{L}\left\{e^{\beta t}\right\}(s) = \frac{1}{s-\beta} \qquad \text{(exponential).} \tag{A.5}$$

Appendix B

Analytical Derivations of Return Times and Delay Differential Equations

B.1 Return times

Consider a wavepacket emitted from the qubit at time t_i whose average position evolves as in Eq. (2.84). The return time t_r is the earliest non-zero time such that $x(t_r) = x_i$. This fulfils the condition

$$k_i - 2\pi \frac{t_r - t_i}{T_B} = -k_i + 2\nu\pi \,, \tag{B.1}$$

with ν an integer number, which gives

$$t_r - t_i = \frac{k_i}{\pi} T_B + \nu T_B \,. \tag{B.2}$$

Taking into account the constraint $t_r - t_i \geq 0$, we get

$$t_r(t_i, k_i) = t_i + \left(1 + \frac{k_i}{\pi}\right) T_B \quad \text{for } -\pi < k_i < 0 \,, \tag{B.3}$$

$$t_r(t_i, k_i) = t_i + \frac{k_i}{\pi} T_B \quad \text{for } 0 \leq k_i \leq \pi \,, \tag{B.4}$$

where on the left-hand side we have highlighted the dependence on t_i and k_i. Note that at these times not only the wavepacket average position is back to the initial value x_i, but even its average energy takes again the initial value $\omega_i = -2J \cos k_i$ [since the oscillations in Eqs. (2.84) and (2.85) are in-phase].

The whole set of return times during the emission dynamics is obtained iteratively as follows. The return times of the first two emitted wavepackest are given by $t_r(0, \pm k_0)$. Either of these is the initial time at which a new pair of wavepackets of momenta $\pm k_0$ are emitted (thus four overall). By iterating this procedure, the whole set of return times can be predicted. In the special case $k_0 = \pm\pi/2$, it is easy to see that the set of return times are simply $\nu T_B/2$ with $\nu = 1, 2, ...$

Notice that the above computation scheme of return times implicitly assumes that each wavepacket is emitted and absorbed instantaneously. This picture breaks down at long times for $\omega_0 \neq 0$, as e.g. in Fig. Fig. 3.3(c1), (c2) and (c3), since the return times of emitted wavepackets get more and more dense.

B.2 Derivation of the delay differential equation

Upon decomposition of the sine function into complex exponentials, Eq. (3.16) can be expressed as

$$\begin{aligned}\mathcal{K}(\tau) = \frac{1}{\pi\xi}\sum_{n=-\infty}^{\infty} e^{-iFn\tau} + \frac{i}{2\pi\xi}e^{-i2\xi}\sum_{n=-\infty}^{\infty} e^{i(\pi-F\tau)n} \\ - \frac{i}{2\pi\xi}e^{i2\xi}\sum_{n=-\infty}^{\infty} e^{-i(\pi+F\tau)n}\end{aligned} \tag{B.5}$$

With the help of the Poisson summation formula

$$\sum_{n=-\infty}^{\infty} e^{inx} = \sum_{n=-\infty}^{\infty} \delta(x/(2\pi)-n) \tag{B.6}$$

the three series in (B.5) can be conveniently expressed in terms of Dirac delta functions as

$$\sum_{n=-\infty}^{\infty} e^{-iFn\tau} = \frac{2\pi}{F}\sum_{n=-\infty}^{\infty}\delta\left(\tau + n\frac{2\pi}{F}\right), \tag{B.7}$$

$$\sum_{n=-\infty}^{\infty} e^{i(\pi-F\tau)n} = \frac{2\pi}{F}\sum_{n=-\infty}^{\infty}\delta\left[\tau + (n-1/2)\frac{2\pi}{F}\right], \tag{B.8}$$

$$\sum_{n=-\infty}^{\infty} e^{-i(\pi+F\tau)n} = \frac{2\pi}{F}\sum_{n=-\infty}^{\infty}\delta\left[\tau + (n+1/2)\frac{2\pi}{F}\right]. \tag{B.9}$$

Taking into account that in our case τ is anyway positive, these can be equivalently arranged as (note in particular the lower bounds of summation)

$$\sum_{n=-\infty}^{\infty} e^{-iFn\tau} = \frac{2\pi}{F}\left[\delta(\tau) + \sum_{n=1}^{\infty}\delta\left(\tau - n\frac{2\pi}{F}\right)\right], \tag{B.10}$$

$$\sum_{n=-\infty}^{\infty} e^{i(\pi-F\tau)n} = \frac{2\pi}{F}\sum_{n=0}^{\infty}\delta\left[\tau + (n+1/2)\frac{2\pi}{F}\right], \tag{B.11}$$

$$\sum_{n=-\infty}^{\infty} e^{-i(\pi+F\tau)n} = \frac{2\pi}{F}\sum_{n=1}^{\infty}\delta\left[\tau + (n-1/2)\frac{2\pi}{F}\right]. \tag{B.12}$$

Plugging these back into Eq. (B.5) with helpf of Eqs. (2.75), (2.80) and (3.5) leads to Eq. (3.17).

Finally, once $K(\tau)$ is replaced with (3.17) in Eq. (3.14) and recalling that $\int_0^t \delta(\tau - \tau^*)f(\tau) = f(\tau^*)\Theta(t-\tau^*)$ and $\Theta(0) = 1/2$, one ends up with the delay differential equation (3.18).

B.3 Delay differential equation for generalized coupling-mode function

Rigorously speaking, despite sharing a ladder-type photonic spectrum, our system differs from an atom coupled to a multi-mode cavity in the functional form of the coupling-mode function g_n. Notwithstanding, the atomic excitation amplitude is governed by the same kind of delay differential equation. This indeed holds for a large class of photonic baths with ladder spectrum, as shown by the following general argument.

Consider a photonic bath with a ladder spectrum of normal frequencies $\omega_n = n\Delta$, where n labels the modes and Δ is the energy spacing (in our case $\Delta = F$). A two-level emitter with frequency ω_0 is coupled to the field under the rotating wave approximation so that Eqs. (3.9) still hold but with the coupling-mode function now taking the general form

$$g_n = g\, f(n) \sin\left(n\frac{\pi}{2} + \varphi\right) . \tag{B.13}$$

In our system for $\omega_0 = 0$ and F weak [cf. Eqs. (3.10) and (2.76)] $f(n)$ is n-independent, whereas for a standard multi-mode cavity $f(n) \propto \sqrt{n}$.

Through the mild requirement that function $\mathcal{F}(n) = f^2(n)$ be analytic, the integro-differential equation governing the evolution of the atomic amplitude $\alpha_e(t)$ in the weak-coupling regime reads

$$\begin{aligned}\frac{d\alpha_e}{dt} = -g^2 \int_0^t dt' \sum_{n=-\infty}^{\infty} \mathcal{F}(n) \sin^2\left(\frac{n\pi}{2} + \varphi\right)&. \\ \times\, e^{-i(\omega_n-\omega_0)(t-t')}\alpha_e(t')&\,.\end{aligned} \tag{B.14}$$

By decomposing the sine function into complex exponentials and upon a Taylor-expansion of $\mathcal{F}(n)$, each power of n can be conveniently expressed as a time derivative of the complex exponential according to

$$\begin{aligned}\frac{d\alpha_e}{dt} =& -g^2 \int_0^t dt' e^{i\omega_0(t-t')} \sum_{m=0}^{\infty} \frac{\mathcal{F}^{(m)}(0)}{m!}\frac{1}{(-i\Delta)^m} \\ &\frac{d^m}{dt^m} \sum_{n=-\infty}^{\infty} e^{-in\Delta(t-t')} \sin^2\left(\frac{n\pi}{2} + \varphi\right) \alpha_e(t') \,.\end{aligned} \tag{B.15}$$

By applying the Poisson summation formula (B.6) along with the property of Dirac delta functions

$$\frac{d^m}{dt^m}\delta(t-t^*) = (-1)^m \delta(t-t^*)\frac{d^m}{dt^m}\,, \tag{B.16}$$

Eq. (B.15) can be turned into the delay differential equation

$$\begin{aligned}\frac{d\alpha_e}{dt} =& -\frac{g^2 T}{2} f^2\left(\frac{\omega_0}{\Delta}\right)\Bigg[\frac{\alpha_e(t)}{2} + \\ &\sum_{n=1}^{\infty} e^{i\omega_0 nT}\alpha_e(t-nT)\Theta(t-nT) - \cos(2\varphi)\times \\ &\times \sum_{n=0}^{\infty} e^{i\omega_0 T(n+\frac{1}{2})}\alpha_e[t-T(n+\tfrac{1}{2})]\Theta[t-T(n+\tfrac{1}{2})]\Bigg]\end{aligned} \tag{B.17}$$

where we set $T = 2\pi/\Delta$.

In our case, $f(n) = \sqrt{2/(\pi\xi)}$, $T = T_B = 2\pi/F$, $\varphi = \xi + \frac{\pi}{4}$ and $\omega_0 = 0$ [cf. Eqs. (B.13), (2.76),(2.80) and (3.10)], in which case $f^2\left(\frac{\omega_0}{\Delta}\right) = 2/(\pi\xi)$, hence Eq. (B.17) reduces to Eq. (3.18).

For a standard cavity instead $T{=}t_d{=}2L/v$, $g{=}\sqrt{\pi v/LV}\mu$ (with μ the atom dipole moment and V the cavity volume) while $f(n) = -\sqrt{n}$, which yields $f^2\left(\frac{\omega_0}{\Delta}\right) = \omega_0/\Delta$.

Appendix C

Derivation of Valley-Polarized Edge Modes

C.1 Derivation of the edge modes

The derivation of the approximate valley-polarized edge modes (4.18) proceeds analogously to the standard low-energy calculation of edge modes in two-dimensional topological lattices [139].

In the presence of a non-uniform sublattice detuning $\Delta(x)$ that varies slowly on the scale of the unit cell, the low-energy effective Hamiltonian in each valley reads [cf. Eq. (2.147)]

$$H_\tau = v\,(\tau p_x \sigma_x + p_y \sigma_y) + \Delta(x)\sigma_z\,. \tag{C.1}$$

Under periodic boundary conditions along the y axis, k_y is a good quantum number. Accordingly, for each value of k_y one can diagonalize the Hamiltonian $H_\tau(k_y)$ obtained from (C.1) under the replacement $p_y \to k_y$.

We search for eigenstates of $H_\tau(k_y)$ whose real-space wavefunction has the form $\Psi_\tau(x,y) = e^{ik_y y}\,\psi_\tau(x)$ with $\psi_\tau(x)$ the x-dependent spinor defined by $\psi_\tau(x) = (\psi_a(x), \psi_b(x))^T$. Enforcing the Schrödinger equation $H_\tau(k_y)\Psi_\tau(x,y) = E\Psi_\tau(x,y)$ yields

$$[v\,(-i\tau\sigma_x\partial_x + k_y\sigma_y) + \Delta(x)\sigma_z]\,\psi_\tau(x) = E\,\psi_\tau(x)\,, \tag{C.2}$$

where we expressed p_x in real space. Eq. (C.2) is equivalent to the system of differential equations

$$\begin{aligned} \Delta(x)\psi_a - i\tau v\,\psi_b' - ivk_y\psi_b &= E\psi_a\,,\\ -\Delta(x)\psi_b - i\tau v\,\psi_a' + ivk_y\psi_a &= E\psi_b\,. \end{aligned} \tag{C.3}$$

where $(\cdot)' \equiv \partial_x(\cdot)$.

Focusing now on the case k_y=0, we search for a zero-energy solution of (C.3). The differential system thus simplifies to a system of coupled first-order linear differential equations with x-dependent coefficients

$$\Delta(x)\psi_a - i\tau v\,\psi_b' = 0, \tag{C.4}$$

$$-\Delta(x)\psi_b - i\tau v\,\psi_a' = 0. \tag{C.5}$$

Under the boundary conditions $\psi_a(\pm\infty) = \psi_b(\pm\infty) = 0$, the solution is

$$\psi_\tau(x) = \mathcal{N} \exp\left[-\frac{1}{v}\int_0^x \Delta(x')\,dx'\right]\begin{pmatrix}1\\ i\tau\end{pmatrix}. \tag{C.6}$$

The normalization condition of (C.6) is easily seen to reduce to the equation

$$4|\mathcal{N}|^2\lambda \int\limits_0^\infty d\xi \cosh^{-\beta}(\xi) = 1\,, \tag{C.7}$$

where $\xi = x/\lambda$ and $\beta = 2\Delta_0\lambda/v$. The integral can be calculated as

$$\int\limits_0^\infty d\xi \cosh^{-\beta}(\xi) = \frac{\sqrt{\pi}}{2}\frac{\Gamma\left(\frac{\beta}{2}\right)}{\Gamma\left(\frac{\beta+1}{2}\right)} \tag{C.8}$$

Solving Eq. (C.7) for $\mathcal{N}$ and replacing in Eq. (C.6), we finally end up with Eq. (4.24).

To derive the dispersion relation, we now consider a finite k_y,

$$H_\tau(k_y) = H_\tau(0) + v_F k_y \sigma_y. \tag{C.9}$$

Since the bound state satisfies $\sigma_y\psi_\tau = \tau\psi_\tau$ we can immediately obtain

$$E_\tau(k_y) = \tau v_F k_y. \tag{C.10}$$

Bibliography

[1] A. S. Sheremet, M. I. Petrov, I. V. Iorsh, A. V. Poshakinskiy, and A. N. Poddubny, *Waveguide quantum electrodynamics: Collective radiance and photon-photon correlations*, Rev. Mod. Phys. **95**, 015002 (2023).

[2] D. Roy, C. M. Wilson, and O. Firstenberg, *Colloquium: Strongly interacting photons in one-dimensional continuum*, Reviews of Modern Physics **89**, 21001 (2017).

[3] F. Ciccarello, P. Lodahl, and D. Schneble, *Waveguide quantum electrodynamics*, Optics and Photonics News **35**, 34–41 (2024).

[4] S. John and J. Wang, *Quantum electrodynamics near a photonic band gap: Photon bound states and dressed atoms*, Phys. Rev. Lett. **64**, 2418–2421 (1990).

[5] S. John and T. Quang, *Spontaneous emission near the edge of a photonic band gap*, Phys. Rev. A **50**, 1764–1769 (1994).

[6] A. G. Kofman, G. Kurizki, and B. Sherman, *Spontaneous and induced atomic decay in photonic band structures*, J. Mod. Opt. **41**, 353–384 (1994).

[7] G. Calajó, F. Ciccarello, D. Chang, and P. Rabl, *Atom-field dressed states in slow-light waveguide qed*, Phys. Rev. A **93**, 033833 (2016).

[8] J. D. Hood, A. Goban, A. Asenjo-Garcia, M. Lu, S.-P. Yu, H. J. Kimble, and D. E. Chang, *Atom-atom interactions around the band edge of a photonic crystal waveguide*, Proc. Natl. Acad. Sci. U.S.A. **113**, 10507–10512 (2016).

[9] Y. Liu and A. A. Houck, *Quantum electrodynamics near a photonic bandgap*, Nat. Phys. **13**, 48–52 (2017).

[10] M. Mirhosseini, E. Kim, V. S. Ferreira, M. Kalaee, A. Sipahigil, A. J. Keller, and O. Painter, *Superconducting metamaterials for waveguide quantum electrodynamics*, Nat. Commun. **9**, 3706 (2018).

[11] L. Zhou, Z. R. Gong, Y.-x. Liu, C. P. Sun, and F. Nori, *Controllable scattering of a single photon inside a one-dimensional resonator waveguide*, Phys. Rev. Lett. **101**, 100501 (2008).

[12] F. Lombardo, F. Ciccarello, and G. M. Palma, *Photon localization versus population trapping in a coupled-cavity array*, Phys. Rev. A **89**, 053826 (2014).

[13] M. Scigliuzzo *et al.*, *Controlling atom-photon bound states in an array of josephson-junction resonators*, Phys. Rev. X **12**, 031036 (2022).

[14] E. Kim, X. Zhang, V. S. Ferreira, J. Banker, J. K. Iverson, A. Sipahigil, M. Bello, A. González-Tudela, M. Mirhosseini, and O. Painter, *Quantum electrodynamics in a topological waveguide*, Phys. Rev. X **11**, 011015 (2021).

[15] A. Goban, C.-L. Hung, J. D. Hood, S.-P. Yu, J. A. Muniz, J. H. Lee, M. J. Martin, A. C. McClung, K. S. Choi, D. E. Chang, O. Painter, and H. J. Kimble, *Superradiance for atoms trapped along a photonic crystal waveguide*, Phys. Rev. Lett. **115**, 063601 (2015).

[16] A. Kay and D. G. Angelakis, *Reproducing spin lattice models in strongly coupled atom-cavity systems*, Europhysics Letters **84**, 20001 (2008).

[17] A. González-Tudela and F. Galve, *Anisotropic quantum emitter interactions in two-dimensional photonic-crystal baths*, ACS Photonics **6**, 221–229 (2019), https://doi.org/10.1021/acsphotonics.8b01455 .

[18] C. Tabares, E. Zohar, and A. González-Tudela, *Tunable photon-mediated interactions between spin-1 systems*, Phys. Rev. A **106**, 033705 (2022).

[19] J. I. Cirac and P. Zoller, *Goals and opportunities in quantum simulation*, Nature Physics **8**, 264–266 (2012).

[20] M. Bello, G. Platero, and A. González-Tudela, *Spin many-body phases in standard- and topological-waveguide qed simulators*, PRX Quantum **3**, 010336 (2022).

[21] C. Tabares, A. Muñoz de las Heras, L. Tagliacozzo, D. Porras, and A. González-Tudela, *Variational quantum simulators based on waveguide qed*, Phys. Rev. Lett. **131**, 073602 (2023).

[22] S. Roca-Jerat, M. Rubín-Osanz, M. D. Jenkins, A. Camón, P. J. Alonso, D. Zueco, and F. Luis, *Waveguide quantum electrodynamics at the onset of spin-spin correlations*, Communications Materials **6**, 172 (2025).

[23] H. Pichler and P. Zoller, *Photonic circuits with time delays and quantum feedback*, Phys. Rev. Lett. **116**, 093601 (2016).

[24] V. S. Ferreira, J. Banker, A. Sipahigil, M. H. Matheny, A. J. Keller, E. Kim, M. Mirhosseini, and O. Painter, *Collapse and revival of an artificial atom coupled to a structured photonic reservoir*, Phys. Rev. X **11**, 041043 (2021).

[25] P. Lodahl, S. Mahmoodian, S. Stobbe, A. Rauschenbeutel, P. Schneeweiss, J. Volz, H. Pichler, and P. Zoller, *Chiral quantum optics*, Nature **541**, 473–480 (2017).

[26] D. G. Suárez-Forero, M. Jalali Mehrabad, C. Vega, A. González-Tudela, and M. Hafezi, *Chiral quantum optics: Recent developments and future directions*, PRX Quantum **6**, 020101 (2025).

[27] H. Pichler, T. Ramos, A. J. Daley, and P. Zoller, *Quantum optics of chiral spin networks*, Physical Review A **91**, 042116 (2015), arXiv:1411.2963 .

[28] R. Mitsch, C. Sayrin, B. Albrecht, P. Schneeweiss, and A. Rauschenbeutel, *Quantum state-controlled directional spontaneous emission of photons into a nanophotonic waveguide*, Nat. Commun. **5**, 5713 (2014).

[29] I. Söllner, S. Mahmoodian, S. L. Hansen, L. Midolo, A. Javadi, G. Kiršanskė, T. Pregnolato, H. El-Ella, E. H. Lee, J. D. Song, S. Stobbe, and P. Lodahl, *Deterministic photon-emitter coupling in chiral photonic circuits*, Nat. Nanotechnol. **10**, 775–778 (2015).

[30] A. F. Kockum, G. Johansson, and F. Nori, *Decoherence-free interaction between giant atoms in waveguide quantum electrodynamics*, Phys. Rev. Lett. **120**, 140404 (2018).

[31] A. F. Kockum, in *Mathematics, Physics, and Chemistry: Interdisciplinary Problems and Applications* (2021) pp. 125–146.

[32] L. Leonforte, X. Sun, D. Valenti, B. Spagnolo, F. Illuminati, A. Carollo, and F. Ciccarello, *Quantum optics with giant atoms in a structured photonic bath*, Quantum Sci. Technol. **10**, 015057 (2025).

[33] V. Jouanny, L. Peyruchat, M. Scigliuzzo, A. Mercurio, E. Di Benedetto, D. De Bernardis, D. Sbroggiò, S. Frasca, V. Savona, F. Ciccarello, and P. Scarlino, *Superstrong dynamics and chiral emission of a giant atom in a structured bath*, arXiv preprint arXiv:2509.01579 (2025).

[34] C. Joshi, F. Yang, and M. Mirhosseini, *Resonance fluorescence of a chiral artificial atom*, Physical Review X **13**, 021039 (2023).

[35] G. Andersson, B. Suri, L. Guo, T. Aref, and P. Delsing, *Non-exponential decay of a giant artificial atom*, Nature Physics **15**, 1123–1127 (2019).

[36] B. Kannan *et al.*, *Waveguide quantum electrodynamics with superconducting artificial giant atoms*, Nature **583**, 775–779 (2020).

[37] A. Goban, C.-L. Hung, S.-P. Yu, J. D. Hood, J. A. Muniz, J. H. Lee, M. J. Martin, A. C. McClung, K. S. Choi, D. E. Chang, O. Painter, and H. J. Kimble, *Atom-light interactions in photonic crystals*, Nat. Commun. **5**, 3808 (2014).

[38] M. Arcari, I. Söllner, A. Javadi, S. L. Hansen, S. Mahmoodian, J. Liu, H. Thyrrestrup, E. H. Lee, J. D. Song, S. Stobbe, and P. Lodahl, *Near-unity coupling efficiency of a quantum emitter to a photonic crystal waveguide*, Phys. Rev. Lett. **113**, 093603 (2014).

[39] S. Schmidt and J. Koch, *Circuit qed lattices: Towards quantum simulation with superconducting circuits*, Ann. Phys. (Berlin) **525**, 395–412 (2013).

[40] J. C. Owens, M. G. Panetta, B. Saxberg, G. Roberts, S. Chakram, R. Ma, A. Vrajitoarea, J. Simon, and D. I. Schuster, *Chiral cavity quantum electrodynamics*, Nature Physics **18**, 1048–1052 (2022).

[41] I. Carusotto, A. A. Houck, A. J. Kollár, P. Roushan, D. I. Schuster, and J. Simon, *Photonic materials in circuit quantum electrodynamics*, Nat. Phys. **16**, 268–279 (2020).

[42] M. A. Pinto, G. L. Sferrazza, D. De Bernardis, and F. Ciccarello, *Non-markovian dynamics of a qubit due to accelerated light in a lattice*, Physica Scripta **100**, 105304 (2025).

[43] M. A. Pinto, G. L. Sferrazza, S. Casulleras, A. Gonzalez-Tudela, D. De Bernardis, and F. Ciccarello, *Giant-atom-enabled quantum optics with valley-polarized photons*, Preprint (2026), arXiv:2605.06771 .

[44] U. Dorner and P. Zoller, *Laser-driven atoms in half-cavities*, Phys. Rev. A **66**, 023816 (2002).

[45] T. Tufarelli, F. Ciccarello, and M. S. Kim, *Dynamics of spontaneous emission in a single-end photonic waveguide*, Physical Review A **87**, 13820 (2013).

[46] A. L. Grimsmo, *Time-Delayed Quantum Feedback Control*, Physical Review Letters **115**, 60402 (2015).

[47] R. Cook and P. Milonni, *Quantum theory of an atom near partially reflecting walls*, Physical Review A **35**, 5081 (1987).

[48] P. Milonni, J. Ackerhalt, H. Galbraith, and M.-L. Shih, *Exponential decay, recurrences, and quantum-mechanical spreading in a quasicontinuum model*, Physical Review A **28**, 32 (1983).

[49] K. Hacker and G. Obermair, *Stark ladders in a one-band-model*, Zeitschrift für Physik A Hadrons and nuclei **234**, 1–5 (1970).

[50] H. Fukuyama, R. A. Bari, and H. C. Fogedby, *Tightly bound electrons in a uniform electric field*, Physical Review B **8**, 5579 (1973).

[51] T. Hartmann, F. Keck, H. J. Korsch, and S. Mossmann, *Dynamics of bloch oscillations*, New Journal of Physics **6**, 2 (2004).

[52] J.-P. Gazeau, V. Hussin, J. Moran, and K. Zelaya, *Generalized susskind–glogower coherent states*, Journal of Mathematical Physics **62** (2021).

[53] I. Ramos-Prieto, K. Uriostegui, J. Récamier, F. Soto-Eguibar, and H. Moya-Cessa, *Kapitza–dirac photonic lattices*, Optics Letters **46**, 4690–4693 (2021).

[54] M. Abramowitz and I. Stegun, *Handbook of Mathematical Functions: With Formulas, Graphs, and Mathematical Tables*, Applied mathematics series (Dover Publications, 1965).

[55] F. Bloch, *Über die quantenmechanik der elektronen in kristallgittern*, Zeitschrift für physik **52**, 555–600 (1929).

[56] C. Zener, *A theory of the electrical breakdown of solid dielectrics*, Proceedings of the Royal Society of London. Series A, Containing Papers of a Mathematical and Physical Character **145**, 523–529 (1934).

[57] M. V. Gustafsson, T. Aref, A. F. Kockum, M. K. Ekström, G. Johansson, and P. Delsing, *Propagating phonons coupled to an artificial atom*, Science **346**, 207–211 (2014).

[58] A. Frisk Kockum, P. Delsing, and G. Johansson, *Designing frequency-dependent relaxation rates and lamb shifts for a giant artificial atom*, Phys. Rev. A **90**, 013837 (2014).

[59] S. M. Girvin and K. Yang, *Modern Condensed Matter Physics* (Cambridge University Press, Cambridge, 2019).

[60] J. K. Asbóth, L. Oroszlány, and A. Pályi, *A short course on topological insulators*, Vol. 919 (Springer, 2016).

[61] A. H. Castro Neto, F. Guinea, N. M. R. Peres, K. S. Novoselov, and A. K. Geim, *The electronic properties of graphene*, Rev. Mod. Phys. **81**, 109–162 (2009).

[62] L. E. F. Foa Torres, S. Roche, and J.-C. Charlier, *Introduction to Graphene-Based Nanomaterials: From Electronic Structure to Quantum Transport* (Cambridge University Press, Cambridge, 2014).

[63] D. Xiao, M.-C. Chang, and Q. Niu, *Berry phase effects on electronic properties*, Rev. Mod. Phys. **82**, 1959–2007 (2010).

[64] D. E. Chang, J. S. Douglas, A. González-Tudela, C.-L. Hung, and H. J. Kimble, *Colloquium: Quantum matter built from nanoscopic lattices of atoms and photons*, Rev. Mod. Phys. **90**, 031002 (2018).

[65] L. Krinner, M. Stewart, A. Pazmiño, J. Kwon, and D. Schneble, *Spontaneous emission of matter waves from a tunable open quantum system*, Nature **559**, 589–592 (2018).

[66] M. Stewart, J. Kwon, A. Lanuza, and D. Schneble, *Dynamics of matter-wave quantum emitters in a structured vacuum*, Phys. Rev. Res. **2**, 043307 (2020).

[67] R. F. Nabiev, P. Yeh, and J. J. Sanchez-Mondragon, *Dynamics of the spontaneous emission of an atom into the photon-density-of-states gap: Solvable quantum-electrodynamical model*, Phys. Rev. A **47**, 3380–3384 (1993).

[68] P. Lambropoulos, G. M. Nikolopoulos, T. R. Nielsen, and S. Bay, *Fundamental quantum optics in structured reservoirs*, Reports on Progress in Physics **63**, 455–503 (2000).

[69] T. Shi, Y.-H. Wu, A. González-Tudela, and J. I. Cirac, *Bound states in boson impurity models*, Phys. Rev. X **6**, 021027 (2016).

[70] J. S. Douglas, H. Habibian, C. L. Hung, A. V. Gorshkov, H. J. Kimble, and D. E. Chang, *Quantum many-body models with cold atoms coupled to photonic crystals*, Nature Photonics **9**, 326–331 (2015).

[71] A. González-Tudela, C.-L. Hung, D. E. Chang, J. I. Cirac, and H. Kimble, *Subwavelength vacuum lattices and atom–atom interactions in two-dimensional photonic crystals*, Nature Photonics **9**, 320 (2015).

[72] N. M. Sundaresan, R. Lundgren, G. Zhu, A. V. Gorshkov, and A. A. Houck, *Interacting Qubit-Photon Bound States with Superconducting Circuits*, Physical Review X **9**, 011021 (2019).

[73] X. Zhang, E. Kim, D. K. Mark, S. Choi, and O. Painter, *A superconducting quantum simulator based on a photonic-bandgap metamaterial*, Science **379**, 278–283 (2023).

[74] G. Calajó, Y.-L. L. Fang, H. U. Baranger, and F. Ciccarello, *Exciting a Bound State in the Continuum through Multiphoton Scattering Plus Delayed Quantum Feedback*, Physical Review Letters **122**, 073601 (2019).

[75] K. Sinha, P. Meystre, E. A. Goldschmidt, F. K. Fatemi, S. L. Rolston, and P. Solano, *Non-markovian collective emission from macroscopically separated emitters*, Physical review letters **124**, 043603 (2020).

[76] H. Pichler, S. Choi, P. Zoller, and M. D. Lukin, *Universal photonic quantum computation via time-delayed feedback*, Proceedings of the National Academy of Sciences **114**, 11362–11367 (2017).

[77] M. Bello, G. Platero, J. I. Cirac, and A. González-Tudela, *Unconventional quantum optics in topological waveguide qed*, Science Advances **5**, eaaw0297 (2019).

[78] D. De Bernardis, Z.-P. Cian, I. Carusotto, M. Hafezi, and P. Rabl, *Light-matter interactions in synthetic magnetic fields: Landau-photon polaritons*, Phys. Rev. Lett. **126**, 103603 (2021).

[79] D. De Bernardis, F. S. Piccioli, P. Rabl, and I. Carusotto, *Chiral quantum optics in the bulk of photonic quantum hall systems*, PRX Quantum **4**, 030306 (2023).

[80] L. Leonforte, A. Carollo, and F. Ciccarello, *Vacancy-like dressed states in topological waveguide qed*, Phys. Rev. Lett. **126**, 063601 (2021).

[81] F. Lombardo, F. Ciccarello, and G. M. Palma, *Photon localization versus population trapping in a coupled-cavity array*, Physical Review A **89**, 053826 (2014).

[82] H.-P. Breuer and F. Petruccione, *The theory of open quantum systems* (OUP Oxford, 2002).

[83] D. O. Krimer, M. Liertzer, S. Rotter, and H. E. Türeci, *Route from spontaneous decay to complex multimode dynamics in cavity qed*, Phys. Rev. A **89**, 033820 (2014).

[84] N. M. Sundaresan, Y. Liu, D. Sadri, L. J. Szocs, D. L. Underwood, M. Malekakhlagh, H. E. Türeci, and A. A. Houck, *Beyond strong coupling in a multimode cavity*, Physical Review X **5**, 21035 (2015), arXiv:1502.02660 .

[85] S. Haroche and J.-M. Raimond, *Exploring the quantum: atoms, cavities, and photons*, first published in paperback ed., Oxford graduate texts (Oxford University Press, Oxford, 2013).

[86] R. D. Driver, *Ordinary and delay differential equations*, Vol. 20 (Springer Science & Business Media, 2012).

[87] R. J. Cook and P. W. Milonni, *Quantum theory of an atom near partially reflecting walls*, Phys. Rev. A **35**, 5081–5087 (1987).

[88] M. Mirhosseini, E. Kim, V. S. Ferreira, M. Kalaee, A. Sipahigil, A. J. Keller, and O. Painter, *Superconducting metamaterials for waveguide quantum electrodynamics*, Nature Communications **9**, 3706 (2018).

[89] A. J. Daley, M. M. Boyd, J. Ye, and P. Zoller, *Quantum computing with alkaline-earth-metal atoms*, Phys. Rev. Lett. **101**, 170504 (2008).

[90] A. González-Tudela and J. I. Cirac, *Non-Markovian Quantum Optics with Three-Dimensional State-Dependent Optical Lattices*, Quantum **2**, 97 (2018).

[91] I. de Vega, D. Porras, and J. Ignacio Cirac, *Matter-wave emission in optical lattices: Single particle and collective effects*, Phys. Rev. Lett. **101**, 260404 (2008).

[92] C. Navarrete-Benlloch, I. d. Vega, D. Porras, and J. Ignacio Cirac, *Simulating quantum-optical phenomena with cold atoms in optical lattices*, New Journal of Physics **13**, 023024 (2011).

[93] R. Ma, B. Saxberg, C. Owens, N. Leung, Y. Lu, J. Simon, and D. I. Schuster, *A dissipatively stabilized mott insulator of photons*, Nature **566**, 51–57 (2019).

[94] V. Jouanny, S. Frasca, V. J. Weibel, L. Peyruchat, M. Scigliuzzo, F. Oppliger, F. De Palma, D. Sbroggiò, G. Beaulieu, O. Zilberberg, *et al.*, *High kinetic inductance cavity arrays for compact band engineering and topology-based disorder meters*, Nature Communications **16**, 3396 (2025).

[95] S. Longhi, *Bloch oscillations in complex crystals with pt symmetry*, Physical review letters **103**, 123601 (2009).

[96] S. Longhi, *Spectral singularities and bragg scattering in complex crystals*, Physical Review A—Atomic, Molecular, and Optical Physics **81**, 022102 (2010).

[97] E. Giese, A. Roura, G. Tackmann, E. M. Rasel, and W. P. Schleich, *Double bragg diffraction: A tool for atom optics*, Physical Review A—Atomic, Molecular, and Optical Physics **88**, 053608 (2013).

[98] J.-Q. Chen, P.-B. Li, Á. Gómez-León, and A. González-Tudela, *Photon-mediated interactions by floquet photonic lattices*, arXiv preprint arXiv:2506.10439 (2025).

[99] D. Xiao, W. Yao, and Q. Niu, *Valley-contrasting physics in graphene: Magnetic moment and topological transport*, Phys. Rev. Lett. **99**, 236809 (2007).

[100] J. R. Schaibley, H. Yu, G. Clark, P. Rivera, J. S. Ross, K. L. Seyler, W. Yao, and X. Xu, *Valleytronics in 2d materials*, Nature Reviews Materials **1**, 16055 (2016).

[101] X. Xu, W. Yao, D. Xiao, and T. F. Heinz, *Spin and pseudospins in layered transition metal dichalcogenides*, Nature Physics **10**, 343–350 (2014).

[102] K. F. Mak, K. He, J. Shan, and T. F. Heinz, *Control of valley polarization in monolayer MoS_2 by optical helicity*, Nature Nanotechnology **7**, 494–498 (2012).

[103] R. V. Gorbachev, J. C. W. Song, G. L. Yu, A. V. Kretinin, F. Withers, Y. Cao, A. Mishchenko, I. V. Grigorieva, K. S. Novoselov, L. S. Levitov, and A. K. Geim, *Detecting topological currents in graphene superlattices*, Science **346**, 448–451 (2014).

[104] T. Ma and G. Shvets, *All-Si valley-Hall photonic topological insulator*, New J. Phys. **18**, 025012 (2016).

[105] J.-W. Dong, X.-D. Chen, H. Zhu, Y. Wang, and X. Zhang, *Valley photonic crystals for control of spin and topology*, Nat. Mater. **16**, 298–302 (2017).

[106] J. Noh, S. Huang, K. P. Chen, and M. C. Rechtsman, *Observation of photonic topological valley-Hall edge states*, Phys. Rev. Lett. **120**, 063902 (2018).

[107] F. Gao, H. Xue, Z. Yang, K. Lai, Y. Yu, X. Lin, Y. Chong, G. Shvets, and B. Zhang, *Topologically protected refraction of robust kink states in valley photonic crystals*, Nat. Phys. **14**, 140–144 (2018).

[108] Y. Kang, X. Ni, X. Cheng, A. B. Khanikaev, and A. Z. Genack, *Pseudo-spin–valley coupled edge states in a photonic topological insulator*, Nat. Commun. **9**, 3029 (2018).

[109] S. Barik, A. Karasahin, C. Flower, T. Lu, H. Miyake, M. Hafezi, and E. Waks, *Chiral quantum optics using a topological resonator*, Phys. Rev. B **101**, 205303 (2020).

[110] M. J. Mehrabad, A. P. Foster, R. Dost, E. Clarke, P. K. Patil, A. M. Fox, M. S. Skolnick, and L. R. Wilson, *Chiral topological photonics with an embedded quantum emitter*, Optica **7**, 1690–1696 (2020).

[111] M. J. Mehrabad, A. P. Foster, N. J. Martin, R. Dost, E. Clarke, P. K. Patil, M. S. Skolnick, and L. R. Wilson, *Chiral topological add-drop filter for integrated quantum photonic circuits*, Optica **10**, 415–423 (2023).

[112] S. Shi, X. Xie, S. Yan, J. Yang, J. Dang, S. Xiao, L. Yang, D. Dai, B. Fu, Y. Yuan, R. Zhu, X. Su, H. Liu, Z. Zuo, C. Wang, H. Ni, Z. Niu, Q. Gong, and X. Xu, *Asymmetric chiral coupling in a topological resonator*, Appl. Phys. Lett. **122**, 191104 (2023).

[113] P. Lodahl, S. Mahmoodian, S. Stobbe, A. Rauschenbeutel, P. Schneeweiss, J. Volz, H. Pichler, and P. Zoller, *Chiral quantum optics*, Nature **541**, 473–480 (2017).

[114] D. G. Suárez-Forero, M. Jalali Mehrabad, C. Vega, A. González-Tudela, and M. Hafezi, *Chiral quantum optics: Recent developments and future directions*, PRX Quantum **6**, 020101 (2025).

[115] X. Gu, A. F. Kockum, A. Miranowicz, Y.-x. Liu, and F. Nori, *Microwave photonics with superconducting quantum circuits*, Physics Reports **718**, 1–102 (2017).

[116] A. Blais, A. L. Grimsmo, S. M. Girvin, and A. Wallraff, *Circuit quantum electrodynamics*, Reviews of Modern Physics **93**, 025005 (2021).

[117] A. F. Kockum, in *International Symposium on Mathematics, Quantum Theory, and Cryptography*, edited by T. Takagi, M. Wakayama, K. Tanaka, N. Kunihiro, K. Kimoto, and Y. Ikematsu (Springer Singapore, Singapore, 2021) pp. 125–146.

[118] L. Guo, A. Grimsmo, A. F. Kockum, M. Pletyukhov, and G. Johansson, *Giant acoustic atom: A single quantum system with a deterministic time delay*, Phys. Rev. A **95**, 053821 (2017).

[119] Y. Wang, J. J. García-Ripoll, and A. C. Santos, *Decoherence-free qubit and chiral emission from a giant molecule in waveguide QED*, arXiv preprint arXiv:2603.27443 10.48550/arXiv.2603.27443 (2026), arXiv:2603.27443 [quant-ph] .

[120] T. Levy-Yeyati, T. Ramos, and A. González-Tudela, *Engineering giant transmon molecules as mediators of conditional two-photon gates*, Phys. Rev. Appl. (2026).

[121] A. M. Vadiraj, A. Ask, T. G. McConkey, I. Nsanzineza, C. W. S. Chang, A. F. Kockum, and C. M. Wilson, *Engineering the level structure of a giant artificial atom in waveguide quantum electrodynamics*, Physical Review A **103**, 023710 (2021).

[122] Z.-Q. Wang, Y.-P. Wang, J. Yao, R.-C. Shen, W.-J. Wu, J. Qian, J. Li, S.-Y. Zhu, and J. Q. You, *Single-magnon quantum acoustics*, Nature Communications **13**, 7580 (2022).

[123] A. González-Tudela, C. Sánchez Muñoz, and J. I. Cirac, *Engineering and harnessing giant atoms in high-dimensional baths: A proposal for implementation with cold atoms*, Phys. Rev. Lett. **122**, 203603 (2019).

[124] Y.-T. Chen, L. Du, Y. Zhang, L. Guo, J.-H. Wu, M. Artoni, and G. C. La Rocca, *Giant-atom effects on population and entanglement dynamics of rydberg atoms in the optical regime*, Phys. Rev. Research **5**, 043135 (2023).

[125] C. Joshi, F. Yang, and M. Mirhosseini, *Quantum control of giant atoms*, Physical Review X **13**, 021039 (2023).

[126] W. P. Su, J. R. Schrieffer, and A. J. Heeger, *Solitons in polyacetylene*, Physical Review Letters **42**, 1698–1701 (1979).

[127] T. Ramos, B. Vermersch, P. Hauke, H. Pichler, and P. Zoller, *Non-markovian dynamics in chiral quantum networks with spins and photons*, Physical Review A **93**, 062104 (2016).

[128] F. Roccati and D. Cilluffo, *Controlling markovianity with chiral giant atoms*, Physical Review Letters **133**, 063603 (2024).

[129] A. González-Tudela and J. I. Cirac, *Exotic quantum dynamics and purely long-range coherent interactions in Dirac-cone-like baths*, Phys. Rev. A **97**, 043831 (2018).

[130] J. Perczel and M. D. Lukin, *Theory of dipole radiation near a dirac photonic crystal*, Phys. Rev. A **101**, 033822 (2020).

[131] J. Redondo-Yuste, M. B. de Paz, P. A. Huidobro, and A. González-Tudela, *Quantum electrodynamics in anisotropic and tilted dirac photonic lattices*, New J. Phys. **23**, 103018 (2021).

[132] E. Di Benedetto, X. Sun, M. A. Pinto, L. Leonforte, C.-Y. Chang, V. Jouanny, L. Peyruchat, P. Scarlino, and F. Ciccarello, *Emergent cavity-qed dynamics along the edge of a photonic lattice*, arXiv 10.48550/arXiv.2507.13444 (2025), arXiv:2507.13444 [quant-ph] .

[133] M. Mirhosseini, E. Kim, V. S. Ferreira, M. Kalaee, A. Sipahigil, A. J. Keller, and O. Painter, *Superconducting metamaterials for waveguide quantum electrodynamics*, Nat. Commun. **9**, 3706 (2018).

[134] J. C. Owens *et al.*, *Chiral cavity quantum electrodynamics*, Nat. Phys. **18**, 1048–1052 (2022).

[135] K. O'Brien *et al.*, *A circuit-qed lattice system with flexible connectivity and gapped flat bands for photon-mediated spin models*, arXiv (2025), arXiv:2505.05559 [quant-ph] .

[136] C. Vega, D. Porras, and A. González-Tudela, *Topological multimode waveguide qed*, Phys. Rev. Res. **5**, 023031 (2023).

[137] J. Jung, F. Zhang, Z. Qiao, and A. H. MacDonald, *Valley-hall kink and edge states in multilayer graphene*, Physical Review B **84**, 075418 (2011).

[138] J. Noh, S. Huang, K. P. Chen, and M. C. Rechtsman, *Observation of photonic topological valley hall edge states*, Physical Review Letters **120**, 063902 (2018).

[139] J. K. Asbóth, L. Oroszlány, and A. Pályi, *A Short Course on Topological Insulators: Band-Structure Topology and Edge States in One and Two Dimensions* (Springer International Publishing, Cham, 2016).

[140] L. Leonforte, X. Sun, D. Valenti, B. Spagnolo, F. Illuminati, A. Carollo, and F. Ciccarello, *Quantum optics with giant atoms in a structured photonic bath*, Quantum Sci. Technol. **10**, 015057 (2025).

[141] A. Morvan, M. Féchant, G. Aiello, J. Gabelli, and J. Estève, *Observation of topological valley hall edge states in honeycomb lattices of superconducting microwave resonators*, Opt. Mater. Express **11**, 1224–1233 (2021).

[142] B. Foxen, J. Mutus, E. Lucero, R. Graff, A. Megrant, Y. Chen, C. Quintana, B. Burkett, J. Kelly, E. Jeffrey, *et al.*, *Qubit compatible superconducting interconnects*, Quantum Science and Technology **3**, 014005 (2018).

[143] C. R. Conner, A. Bienfait, H.-S. Chang, M.-H. Chou, É. Dumur, J. Grebel, G. A. Peairs, R. G. Povey, H. Yan, Y. P. Zhong, and A. N. Cleland, *Superconducting qubits in a flip-chip architecture*, Applied Physics Letters **118**, 232602 (2021).

[144] G. J. Norris, L. Michaud, D. Pahl, M. Kerschbaum, C. Eichler, J.-C. Besse, and A. Wallraff, *Improved parameter targeting in 3d-integrated superconducting circuits through a polymer spacer process*, EPJ Quantum Technology **11**, 5 (2024).

[145] G. B. Arfken, H. J. Weber, and F. E. Harris, *Mathematical methods for physicists: a comprehensive guide* (Academic press, 2011).

[146] M. L. Boas, *Mathematical methods in the physical sciences* (John Wiley & Sons, 2006).

[147] S. Hassani, *Mathematical physics: a modern introduction to its foundations* (Springer Science & Business Media, 2013).